FEDERAL UNIVERSITY OF SÃO CARLOS
CENTER FOR EXACT SCIENCES AND TECHNOLOGY
GRADUATE PROGRAM IN MATERIALS SCIENCE AND ENGINEERING

INJECTION OVERMOLDING OF POLYCARBONATE-ALUMINUM ALLOYS HYBRID STRUCTURES

Gean Henrique Marcatto de Oliveira

São Carlos-SP
2023

FEDERAL UNIVERSITY OF SÃO CARLOS
CENTER FOR EXACT SCIENCES AND TECHNOLOGY
GRADUATE PROGRAM IN MATERIALS SCIENCE AND ENGINEERING

INJECTION OVERMOLDING OF POLYCARBONATE-ALUMINUM ALLOYS HYBRID STRUCTURES

Gean Henrique Marcatto de Oliveira

Doctoral thesis conducted under cotutelle agreement presented to the Graduate Program in Materials Science and Engineering as a partial requirement to obtain the title of DOCTOR IN MATERIALS SCIENCE AND ENGINEERING conferred by the Federal University of São Carlos (UFSCar) and the title of DOCTOR OF TECHNICAL SCIENCES IN MECHANICAL ENGINEERING conferred by Graz University of Technology (TU Graz)

Advisors: Dr. Leonardo Bresciani Canto – UFSCar, Brazil
Dr.-Ing. Sergio de Traglia Amancio Filho – TU Graz, Austria

Funding agencies: CNPq (grant number: 164791/2018-3); CAPES (grant number: 88887.569948/2020-00); FAPESP (grant number 2018/24296-0) and The Austrian Ministry for Climate Action, Environment, Energy, Mobility, Innovation and Technology, BMK (TAKE-OFF grant number 852796, 2018)

São Carlos-SP
2023

DEDICATION

To my grandparents, Sirlena Mazzari Marcatto and Antonio Jorge Marcatto

“There´s a feeling I get
When I look to the west
And my spirit is crying for leaving
In my thoughts I have seen
Rings of some through the trees
And the voices of those who stand looking”

Robert Plant, Led Zeppelin - Stairway to Heaven

VITAE

University Degree in Aircraft Maintenance Technology, Federal Institute of São Paulo (2014); Master in Materials Science and Engineering, Federal University of São Carlos (2018)

UNIVERSIDADE FEDERAL DE SÃO CARLOS

Centro de Ciências Exatas e de Tecnologia
Programa de Pós-Graduação em Ciência e Engenharia de Materiais

Folha de Aprovação

Defesa de Tese de Doutorado do candidato Gean Henrique Marcatto de Oliveira, realizada em 24/03/2023.

Comissão Julgadora:

Prof. Dr. Leonardo Bresciani Canto (UFSCar)

Prof. Dr. Sebastião Vicente Canevarolo Junior (UFSCar)

Prof. Dr. José Eduardo Spinelli (UFSCar)

Prof. Dr. Sergio de Traglia Amancio Filho (TU Graz)

Prof. Dr. Sandro Campos Amico (UFRGS)

O Relatório de Defesa assinado pelos membros da Comissão Julgadora encontra-se arquivado junto ao Programa de Pós-Graduação em Ciência e Engenharia de Materiais.

ACKNOWLEDGEMENTS

The development of this doctoral work counted on the help of several people for whom I would like to sincerely thank:

- First of all, I thank God – the basis of my faith.
- To all my family, who supported me during my graduation, especially my parents, Claudia and Odair and my uncles, Dulcelena and Rubens.
- Prof. Dr. Leonardo Bresciani Canto, for the opportunity and trust in this work and all the dedication and commitment to my development as a professional and researcher.
- Prof. Dr.-Ing. Sergio Traglia Amancio-Filho for all the discussions, incentives and valuable orientations and support for accomplishing this work. Also, for the honorable opportunity to establish a co-tutelle agreement between UFSCar and the University of Technology of Graz, Austria.
- Prof. Dr. Arnaldo Carlos Morelli who introduced me to the world of materials science and engineering and has always trusted my potential since undergraduation.
- I thank my post-graduation friends from PPGCEM, Brazil and the friends I met during my internship at TU Graz, Austria.
- I would like to thank SABIC Innovative Plastics South América for readily making available the polymer used in this work.
- I would like to thank the research group of Prof. Rodrigo B. Canto, in particular Prof. Vinicius Sciuti, for the analysis of digital image correlation (DIC).
- The financial support was provided by the Austrian aviation program “TAKE-OFF” and the Austrian Ministry for Climate Action, Environment, Energy, Mobility, Innovation and Technology, BMK.
- To CNPq - Conselho Nacional de Desenvolvimento Científico e Tecnológico for the financial support for this work with a scholarship (grant numbers 164791/20183)
- This study was financed in part by the Coordencao de Aperfeicoamento de Pessoal de Nível Superior – Brasil (CAPES) – Finance Code 001.

ABSTRACT

Overlap joints between polycarbonate (PC) and aluminum alloys AA6061 and AlSi10Mg were manufactured by injection overmolding and evaluated regarding the interfacial structure and mechanical performance. The injection overmolding parameters; barrel temperature, injection speed and holding pressure were optimized through a design of experiments, using AA6061 inserts machined from an rolled sheet and laser surface textured. The injection molding parameters studied showed a positive effect on the filling of the grooves on the metal surface. The ultimate lap-shear force (ULSF) was used as a response and the values correlated to the filling of the polymer into the grooves of the metal surface, the molding conditions and the rheology of the polymer. Additionally, with the aid of design of experiments, AlSi10Mg inserts were produced by laser powder bed fusion (L-PBF), and their surfaces were structured with submillimetrical dimensions features on the metal surface, so-called, inkpot-like, mushroom-like and lattice structures. Afterwards, the metal inserts were hybridized with PC via injection overmolding and the interfacial strength were evaluated. PC/AA6061 and PC/AlSi10Mg joints exhibited outstanding joining strength of 7.2 MPa ± 0.5 MPa and 20.5 MPa ± 3.8 MPa, respectively. Fracture analysis through optical and scanning electron microscopies and digital image correlation (DIC) was used to elucidate the joint failure mechanisms. In dynamic fatigue testing, joints exhibited fatigue life close to 30% ULSF, demonstrating excellent mechanical durability. In addition, PC/AA6061 joints showed excellent hygrothermal stability. The findings add to the comprehension of the manufacturing, mechanical behavior and durability of injection overmolded polymer-metal hybrid structures.

Keywords: Injection overmolding; polymer-metal hybrid structures; additive manufacturing; polycarbonate; aluminum.

RESUMO

SOBREMOLDAGEM POR INJEÇÃO DE ESTRUTURAS HÍBRIDAS DE POLICARBONATO E LIGAS DE ALUMÍNIO

Juntas sobrepostas de policarbonato (PC) e ligas de alumínio AA6061 e AlSi10Mg foram fabricadas por sobremoldagem por injeção e avaliadas quanto à estrutura interfacial e o desempenho mecânico. Os parâmetros de moldagem por injeção, temperature do barril, velocidade de injeção e pressão de recalque, foram otimizados a partir de um planejamento de experimentos, utilizando-se insertos de AA6061 usinados a partir de chapa extrudada e texturizados a laser. A força máxima em ensaio de cisalhamento foi utilizada como resposta e os valores correlacionados com o preenchimento do polímero nas cavidades da superfície do metal, as condições de moldagem e a reologia do polímero. Adicionalmente, com auxílio de planejamento de experimentos, insertos de AlSi10Mg foram produzidos e suas superfícies estruturadas por fusão seletiva em leito de pó com estruturas em escalas submilimétricas denominadas tipo tinteiro, cogumelo e treliça. Posteriormente os insertos metálicos foram hibridizados com PC por sobremoldagem por injeção e a resitência interfacial foi avaliado. As juntas PC/AA6061 e PC/AlSi10Mg apresentaram resistências ao cisalhamento notáveis, de até 7,2 MPa ± 0,5 MPa e 20,5 MPa ± 3,8 MPa, respectivamente. Análise de falhas via microscopia ótica e eletrônica de varredura e correlação de imagens digitais (CID) foi empregada para elucidação dos mecanismos de falha das juntas. Em ensaio de fadiga dinâmica as juntas PC/AA6061 e PC/AlSi10Mg apresentaram limite de resistência próximo dos 30% da força máxima de cisalhamento, o que indica excelente durabilidade mecânica. Além disso, juntas PC/AA6061 apresentaram excelente estabilidade higrotérmica. Os resultados contribuem para a compreensão do processo de fabricação, comportamento mecânico e durabilidade de estruturas híbridas polímero-metal sobremoldadas por injeção.

Palavras chave: Sobremoldagem por injeção; estruturas polímero-metal; manufatura aditiva; policarbonato; alumínio.

KURZFASSUNG

SPRITZGIESSEN VON HYBRIDSTRUKTUREN AUS POLYCARBONAT-ALUMINIUM-LEGIERUNGEN

Überlappende Verbindungen zwischen Polycarbonat (PC) und den Aluminiumlegierungen AA6061 und AlSi10Mg wurden durch Spritzgießen hergestellt und hinsichtlich der Grenzflächenstruktur und der mechanischen Leistung bewertet. Die Parameter für das Spritzgießen - Zylindertemperatur, Einspritzgeschwindigkeit und Nachdruck - wurden mit Hilfe eines Versuchsplans optimiert, wobei AA6061-Einsätze verwendet wurden, die aus einer stranggepressten Platte hergestellt und mit einer Laseroberfläche versehen wurden. Die untersuchten Spritzgießparameter zeigten einen positiven Effekt auf die Füllung der Nuten auf der Metalloberfläche. Die ultimative Überlappungsscherkraft (ULSF) wurde als Antwort verwendet, und die Werte korrelierten mit der Füllung des Polymers in die Nuten der Metalloberfläche, den Gießbedingungen und der Rheologie des Polymers. Zusätzlich wurden mit Hilfe von Versuchsplänen AlSi10Mg-Einsätze durch Laser-Pulverbettschmelzen (L-PBF) hergestellt und ihre Oberflächen mit submillimetrischen Strukturen auf der Metalloberfläche, so genannten Tintenfass-, Pilz- und Gitterstrukturen, strukturiert. Anschließend wurden die Metalleinsätze durch Spritzgießen mit PC hybridisiert und die Grenzflächenfestigkeit wurde bewertet. PC/AA6061- und PC/AlSi10Mg-Verbindungen wiesen eine hervorragende Verbindungsfestigkeit von 7,2 MPa ± 0,5 MPa bzw. 20,5 MPa ± 3,8 MPa auf. Die Bruchanalyse mittels Licht- und Rasterelektronenmikroskopie und digitaler Bildkorrelation (DIC) wurde zur Aufklärung der Versagensmechanismen der Verbindungen eingesetzt. In dynamischen Ermüdungstests wiesen die Verbindungen eine Dauerfestigkeit von nahezu 30 % ULSF auf, was eine ausgezeichnete mechanische Beständigkeit belegt. Darüber hinaus zeigten die PC/AA6061-Verbindungen eine ausgezeichnete hygrothermische Stabilität. Die Ergebnisse tragen zum Verständnis der Herstellung, des mechanischen Verhaltens und der Haltbarkeit von spritzgegossenen Polymer-Metall-Hybridstrukturen bei.

Stichworte: Overmolding- Verfahren; Polymer-Metall-Hybridstrukturen; Additive Fertigung; Polycarbonat; Aluminium.

x

PUBLICATIONS

ISI-Papers:

- Oliveira, G.H.M.; Belei, C.: Carvalho, W.; Canto, L. B.; Amancio-Filho, S. T.; On the fully additive manufacturing of PC/AlSi10Mg hybrid structures. **Materials Letters**, v. 330, 133378, 2022.
- Vasconcelos, R. L.; Oliveira, G. H. M.; Amancio-Filho, S. T.; Canto, L. B.; Injection Overmolding of Polymer-Metal Hybrid Structures: A review. **Polymer Engineering and Science**, v. 63, p. 691 – 722, 2023.

Conference proceedings

- Oliveira, G. H. M.; Amancio-Filho, S. T.; Canto, L. B.; Injection Overmoulded Polymer-Metal Hybrid Structures. Advanced Materials Poster Day, Graz, Austria, 2022.
- Oliveira, G.H.M.; Silva, J.M.O; Riva, Rudimar; Amancio-Filho, S. T.; Canto, L. B.; Juntas Híbridas de Policarbonato e Alumínio 6061-T6 Produzidas por Sobremoldagem por Injeção: Efeitos da Texturização a Laser do Metal sobre a Resistência Interfacial. 15th Brazilian Polymer Conference (CBPOL), Bento Bento Gonçalves, 2019.
- Oliveira, G.H.M.; Silva, J.M.O; Volu, R. M.; Vasconcelos, G.; Amancio-Filho, S. T.; Canto, L. B.; Injection Over-Molded Polycarbonate-Aluminum Composite Structures. 5th Brazilian Conference on Composite Materials (BCCM), São Carlos, Brazil, 2021.
- Oliveira, G. H. M.; Amancio-Filho, S. T.; Canto, L. B.; Injection Overmolded Polymer-Metal Hybrid Structures. 16th Brazilian Polymer Conference (CBPOL), Ouro Preto, Brazil, 2021.

SUMMARY

LIST OF TABLES

LIST OF FIGURES

SYMBOLS AND ABBREVIATIONS

AM	Addtive Manufacturing
AA2024	Aluminum alloy 2024
AA5052	Aluminum alloy 5052
AA6061	Aluminum alloy 6061
AA6082	Aluminum alloy 6082
ABS	Acrylonitrile butadiene styrene
ABS-GP	Glass fiber reinforced acrylonitrile butadiene styrene
AddJoining	Joining via additive manufacturing
AlSi10Mg	Aluminum alloy AlSi10Mg
ANOVA	Analysis of variance
ASTM	American society for testing and materials
Al_20_3	Aluminum oxide
BED	Beam expander diameter
CAD	Computed-aided design
CO_2	Carbon dioxide
CW	Continuous wave laser
DIC	Digital image correlation
DSC	Differential scanning calorimetry
DoE	Design of experiments
EDS	Energy-dispersive x-ray spectroscopy
FFF	Fused filament fabrication
FEA	Finite element analysis
GFRP	Glass fiber reinforced polymer
H_3PO_4	Phosphoric acid
HIP	Hot isostatic pressure
HNO_3	Nitric acid
L-PBF	Laser powder bed fusion
NaOH	Sodium hydroxide
OM	Optical microscopy
PA66	Polyamide 66
PA-CF	Carbon fiber reinforced polyamide

PC	Polycarbonate
PEI	Polyetherimide
PEEK	Polyether ether ketone
PP	Polypropylene
PP-GF	Carbon fiber reinforced polypropylene
PPS-GF	Carbon fiber reinforced polyphenylene sulfide
PBT-GF	Carbon fiber reinforced polybutylene terephthalate
PW	Pulsed wave laser
PMH	Polymer-metal hybrids
PMMA	Polymethyl methacrylate
PPS	Polyphenylene sulfide
R_a	Average roughness
R_z	Average between heights of five peaks and valleys
SEM	Scanning electron microscopy
SLM	Selective laser melting
STEM	Scanning transmission electron microscopy
Ti6Al4V	Titanium alloy Ti6Al4V
ULSF	Ultimate lap-shear force
UV	Ultraviolet

1. INTRODUCTION

In the last decades, engineering and high-performance polymers have been gaining ground in structural applications in the automotive and aeronautical sectors [1]. This pattern is brought on by the low density, simple processing requirements, design of flexibility, and strong chemical resistance of polymers. In contrast, metals have more noticeable features than polymers for some structural applications, such as components adjacent to vehicle engines, due to their higher stiffness, strength, and thermo-mechanical resistance [2]. In this regard, the development of polymer-metal hybrid structures (PMH), which can synergistically combine the capabilities of both materials and fill specific deficiencies of each class, has eased this dichotomy between the choosing of polymer or metal materials [3].

Transportation is one of the most in need of parts and components with low density and superior mechanical properties, as lighter vehicles can reduce fuel consumption and, as a result, decrease the emission of pollutant gases and/or increase load capacity. The automotive industries present a wide field of applications of polymer-metal hybrid structures, with a strong interest in producing hybrid components formed by the joining of polycarbonate (PC) and aluminum alloys, since these materials are widely used as neighbor parts in this sector. PC has high tensile and impact strength and high heat resistance, and due to its transparency, it can replace vehicle windshields. Other applications for PC include fog lights, air conditioning systems, radiator grilles and glove box covers [4]. AA6061 is one of the most widely used aluminum alloys in automotive components, such as wheel hub, vehicle body, braking system, engine components and others. Moreover, it is commonly used in manufacturing bicycle frames and other sectors, such as the construction of towers, furniture, railroad cars, and several other applications that demand good weldability and corrosion resistance [5]. This alloy contains magnesium and silica as main alloying elements and presents good tensile strength, good weldability, easy machining, and high corrosion resistance (in comparison to other aluminum alloys) [6]. Another aluminum alloy has gained prominence for its easy processability by additive manufacturing is the AlSi10Mg alloy. It presents great interest for the

aerospace, automotive, and biomedical industries for possible applications in lightweight structures [7].

Mechanical fastening and adhesive bonding are the most conventional ways for polymer-metal joining [1]. However, these solutions still face significant manufacturing process and hybrid structure performance problems. In mechanical fastening, they are connected to a large number of process steps, increases the weight of the final structure and the stress concentration is caused by the existence of through holes. In contrast, adhesive bonding is accompanied by the need of surface pre-treatments, long curing periods, low heat and chemical resistance, and toxic chemicals and solvents.

Alternative approaches with high efficiency and low processing costs, including friction-based [8–13] and fusion-based [14–16] techniques, have been developed to address these shortcomings. In general, the friction-based joining techniques rely on the generation of heat by the friction and feed of a non-consumable rotating tool or metal fastener on a polymeric part or a polymer-metal assembly to produce macro- or micromechanical interference joints as well as promote adhesion forces between the consolidate polymer and metal surface [17,18]. The laser welding technique has also been highlighted in recent years [37,38]. This technique, in a simplified way, consists of softening the polymer in the region of contact with the metal employing a laser beam, causing the polymer to soften/deepen and infiltrate into grooves on the metal surface to form the polymer-metal joint. The Ultrasonic Joining [39] - sometimes called by some authors [40] Ultrasonic Welding – is another technique widely used in industry and explored in the literature [10,40–45]. Moreover, AddJoining is a process that combines additive manufacturing with material joining principles.

Metal insert injection over-molding, also known as ‘metal over-molding’ or ‘injection overmolding’ (other possible forms include ‘over-molding’, over-moulding or overmoulding), is a technique with great potential for joining polymer-metal hybrid structures with several advantages over the previously mentioned joining and additive manufacturing techniques [48,49]. These include improved stress distribution and mechanical performance, as well as the absence of adhesive or fasteners, which significantly reduces the weight of the structures

formed. In its basic configuration, polymer-to-metal joining occurs by adhesion forces and mechanical interference through the filling of the polymer into through-holes in the metal structure and by forming flanges [48]. The technique of injection overmolding with direct-adhesion, also known as ‘direct-adhesion injection overmolding’, uses metal inserts with a textured surface or adhesion promoters, whose joining mechanism is by physical and/or chemical adhesion forces [50].

Even though injection overmolding has already been studied for a variety of material combinations, there are still fundamentals knowledge gaps concerning the fatigue and hygrothermal durability of these joints. Furthermore, there is a lack of detailed understanding of the correlations between process parameters, structure/microstructure and mechanical properties. Finally, the use of metal inserts produced by additive manufacturing for hybridization via injection overmolding has not been extensively explored.

In this context, the main objective of this study was to develop polycarbonate/aluminum alloys (AA6061 and AlSi10Mg) hybrid structures prepared by injection overmolding, with potential application in engineering lightweight structures. Experiments and data analysis were conducted in an attempt to establish relationships between processing conditions, interfacial microstructure and mechanical and chemical performance of the hybrid joints. The effects of injection overmolding parameters on the joining strength were evaluated through design of experiments (DoE) and analysis of variance (ANOVA). High-density AlSi10Mg inserts were produced and surface structured by additive manufacturing (Laser Powder Bed Fusion – L-PBF) with the aid of DoE and then joined with PC using optimized injection overmolding conditions. Microstructure and joint failure mechanisms after quasi-static mechanical testing were evaluated through optical (OM), scanning electron (SEM), and laser confocal microscopy, as well as digital image correlation (DIC). Moreover, fatigue strength of hybrid joints was studied, while their chemical resistance was evaluated through hygrothermal aging tests on PC/AA6061 joints.

2. LITERATURE REVIEW

2.1 Adhesion theories

The adhesion theories or mechanisms are usually categorized into several main models or areas, namely, mechanical interlocking, electronic or electrostatic; adsorption (thermodynamic) or wetting theory; diffusion; chemical (covalent) bonding; acid-base; and weak boundary layer.

Temesi and Czigany [51] proposed, as depicted in Figure 2.1, a categorization for adhesion theories based on the magnitude of activity of the primary mechanism. The main process will depend on the conditions on the metal surface prior to hybridization, such as the deposition of adhesion promoters or the structuring of the metal surface.

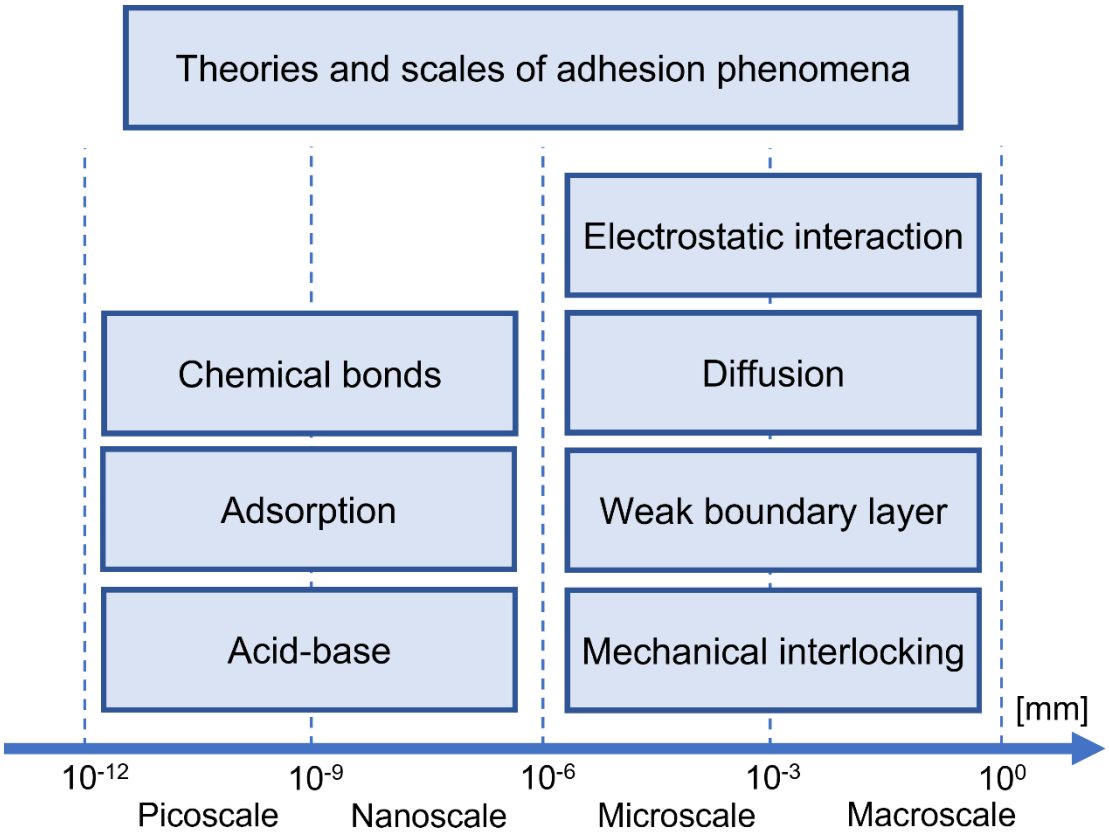

Figure 2.1: Action scale of the adhesion phenomena theories. Source: Adapted from reference [51].

In polymer-metal hybrid (PMH) structures manufactured by injection overmolding, the following adhesion mechanisms are expected to occur to a greater or lesser extent: mechanical interlocking, weak boundary layer, chemical bonding and adsorption [52]. Nevertheless, adhesion is typically the product of a mixture of these mechanisms.

Mechanical interlocking in injection overmolded PMH results from the micromechanical interlocking of the polymer into microcavities (roughness, pores) or microfeatures (pins, pultrusion, lattice structures) present on the metal surface. The ability of the molten polymer to infiltrate the microcavities is related not only to the surface energies of the metal but also to the viscosity of the molten polymer, fluid pressure, and microcavity geometry [52,53]. Increasing the temperature of the molten polymer enables lower viscosity and, consequently, greater filling of the polymer into the microcavities. The correlation of roughness filling as a function of spreading time and polymer temperature, $x(t)$, can be represented quantitatively by an adaptation of Poiseuille law, given by Equation 2.1 [52].

$$x(t) = \sqrt{\left(\frac{r.\gamma_{LV}.\cos\theta_{\infty}}{2\eta}\right).\left(t - \frac{a}{c} + \frac{a.e^{-ct}}{c}\right)} \qquad (2.1)$$

Where r is the radius of the microcavity, θ_{∞} is the contact angle, γ_{LV} is the surface free energy, a and c are adjustable parameters, and η is the polymer viscosity.

Figure 2.2 is a simplified, out-of-scale representation of the effect of temperature, roughness, pressure and spreading time on the filling capability of a molten polymer into the surface roughness of a metal. In general, the mechanical interlocking of the polymer on the metal surface is intensified by increasing the surface roughness of the metal, the temperature of the polymer and metal, the pressure exerted, and the wetting time. Mechanical micro-interlocking can also be enhanced by modification of the polymer with the addition of fillers, as identified by Lucchetta *et al*. [53]. The authors explored hybrid joints of glass-fiber reinforced polypropylene (PP-GF) or poly(phenylene sulfide) (PPS-

GF) with 6082 aluminum alloy. Corundum powder with typical grain sizes of 0.1 mm to 0.6 mm were used to blast metal inserts. The joining strength of PP-GF/AA6082 joints increased with the glass-fiber content (30 to 50 wt%), whereas the joining strength of PPS-GF/AA6082 joints increased with the metal surface average roughness (2 µm to 6 µm), injection speed (80 mm/s to 120 mm/s), and metal preheating temperature (300 °C to 450 °C). The researchers correlated these findings with the degree of polymer filling in metal microscale roughness patterns. A higher roughness topography enhanced adhesion since it allowed the polymer to flow into the microcavities and the glass fibers to bind the polymer to the metal surface. The increase in the metal surface temperature also facilitated this effect.

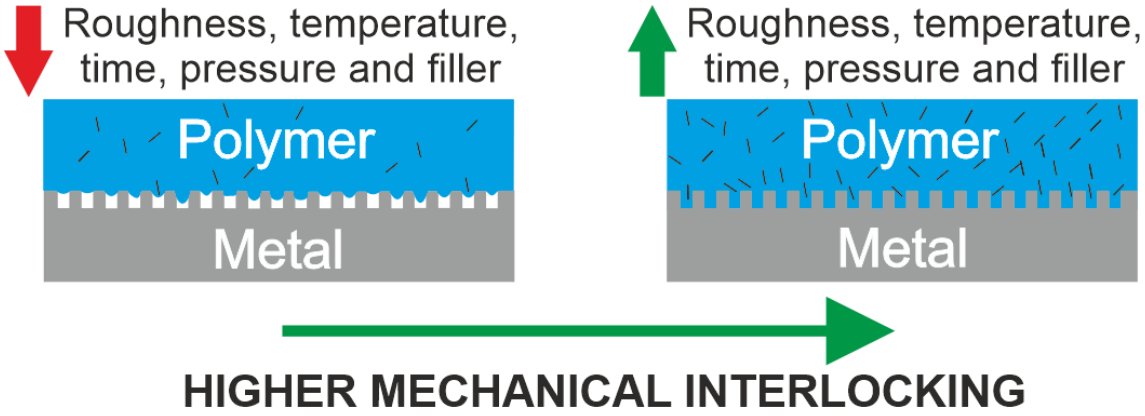

Figure 2.2: Schematics of the influence of metal substrate surface roughness, polymer temperature, pressure, and spreading time on melt polymer filling (in blue) in the microcavities of the metal insert (in gray). Adapted from reference [53].

Another theory that helps to understand the failure behavior of injection overmolded PMH joints is the weak layer model; naturally, the rough surface of aluminum has a thin and irregular natural layer of aluminum oxide (Al_2O_3), which can act as a preferential site for adhesive fracture in the polymer-metal interface. However, a thick porous layer of alumina purposely formed on the aluminum surface by anodizing can promote mechanical interlocking by filling the molten polymer into the regular and deeper pores of the alumina layer [54–56].

The chemical bond and diffusion theories also assist in understanding the adhesion of injection overmolded PMH, as some material combinations form primary chemical bonds at the interface. Liu, Dong, and Sun [57] identified via X-ray photoelectron spectroscopy (XPS) on samples of vaporized aluminum oxide layer onto PA66 plates the formation of Al-O-C bonds at the interface. The authors hypothesized that the carbonyl group of the PA66 chains on the surface of the plate produces a coordination covalent bond with the Al, which might also be observed in other combinations of aluminum alloys and polymers containing carbonyl groups, such as polycarbonate. Moreover, Goushegir *et al*. [58], through XPS analysis have also identified the formation of Al-C and Zr-C bonds at a fractured surface of AA2024/CF-PPS hybrid joints.

Chemical bonds and diffusion can also be achieved by deposition of adhesion promoter or also called "primer" to the metal surface [59]. This layer must have a mutual good chemical interaction with the metal and the polymer. Moreover, the primer layer needs to achieve a good anchorage in the roughness crevices of the metal or porous oxide layer and not act as a weak layer between the dissimilar materials, as all the stress applied to the joint will be concentrated at the adhesion promoter interface [59,60].

The adsorption or wetting theory describes adhesion between materials by interatomic interactions established between atoms and molecules at the interface. According to this theory, to have a joining between two materials, the adhesive must wet or infiltrate the microcavities of the substrate. The wetting depends on the surface tension of the joint components and due to the complexity, surface tension is equated with surface free energy. This energy can be calculated from the contact angle between adhesive and substrate. The adhesive is dripped onto the substrate and the angle formed by the liquid is measured. The lower the contact angle of the liquid on the substrate, the higher the wettability. Adsorption is the result of chemical interactions such as acid-base interactions, hydrogen bonds, or van der Walls forces [61]. The contact angle can be estimated using the equation of Young, Equation 2.2, for a smooth and homogeneous surface.

$$\gamma_s = \gamma_{sl} + \gamma_l \cos\theta \qquad (2.2)$$

Being, γ_s is the surface free energy of the substrate (mJ/m²), γ_{sl} is the interfacial free energy between substrate and liquid, γ_l is the surface free energy of the dripped liquid (mN/m), and θ the wetting angle (Young-Dupré) or contact angle.

The wettability on the substrate will depend not only on the surface energy differences between solid, liquid and interactions at the interface but also on the surface roughness of the substrate. In addition to the surface energy difference, increased wettability, or in other words, the ability of the polymer to infiltrate the microcavities (roughness) of the metal surface is hindered by the presence of trapped air within the microcavities. This trapped air acts as a barrier against movement of the molten polymer into the microcavity. In the case of injection overmolding of polymer-to-metal joints, the high pressure applied to the injected polymer drives entrapped air out of the roughness crevices. Li *et al*. [62] investigated the influence of metal surface topography and temperature on the joining strength of PP/AA6061 single-lap joints. Four grades of abrasive with varying particle sizes (A = 2 mm; B = 1 mm; C = 0.5 mm; D = 0.3 mm) were used to sandblast metal inserts, resulting in varied average surface roughness (R_a) and topographical features density. As shown in Figure 2.3a, the contact angle of molten PP (200 °C) on AA6061 substrates at 190 °C decreased as surface roughness and features density decreased. Moreover, the contact angle decreased progressively with increasing metal surface temperature (Figure 2.3b) for a substrate with constant surface roughness and feature density (sandblasted surface with particles size C). Low contact angles between the polymer and metal were found to aid the filling of metal surface features with polymer melt, hence enhancing the joining strength. The highest ultimate lap-shear force (ULSF) values up to 250 N for an overlap area of 10 x 15 mm^2 were achieved for C (R_a of 4.30 µm and surface density area of 195 mm^2) and D (3.97 µm and 193 mm^2) surfaces with decreasing surface roughness and increased feature density. Considering the same metal surface (A–D), the lap-shear strength was highest

when the surface temperature was 120 °C. PP cohesive failure was also seen in PP/AA6061 joints produced with higher metal surface temperatures.

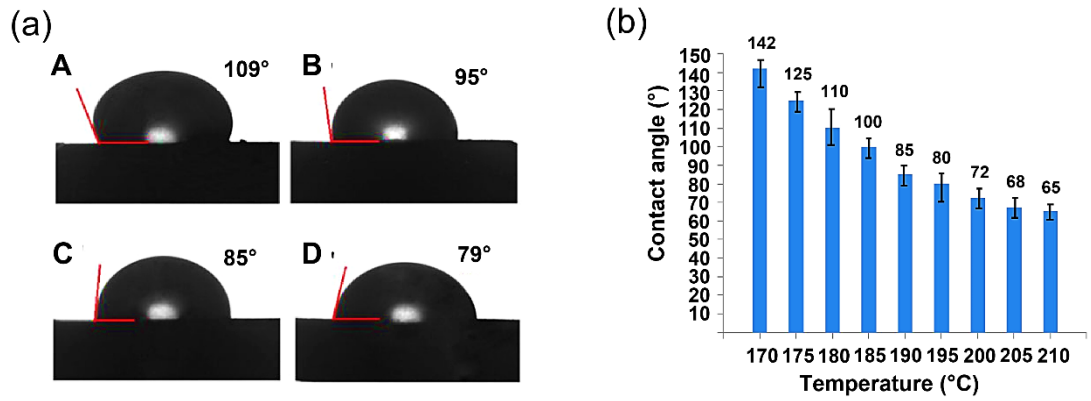

Figure 2.3: Contact angle of molten polypropylene (PP) onto AA6061 substrate in different surface conditions. a) Contact angle at different average roughness and features density; b) Contact angle at different surface temperatures for a surface sandblasted with particles diameter of 0.5 mm (C). Adapted from Reference [62].

2.2 Mechanical behavior of polymer-metal hybrid joints

Due to the convenience of production and the simplicity of comprehending stresses, single-lap joints are the most frequent method for assessing the joining strength of polymer-metal hybrid systems. The components of a single-lap joint and the loads imposed and resulting stresses are schematically depicted in Figure 2.4a. In general, the adhesive or interface area transfers the load between the joined parts and withstands these stresses. When single-lap joints are loaded, a combination of peel (y) and shear stresses (xz) predominate. Moreover, tensile and compression stresses are also present, which manifest as normal stresses (z) in the direction of the adhesive thickness (interface). These combined efforts concentrate stress at the joint ends, such as shown in the inlet graph of Figure 2.4 for the peak shear stress distribution (τ_{max}); hence, the fracture process will begin primarily at the ends of the overlapping region [63]. When overloaded, structural components having geometric eccentricities undergo secondary bending and out-of-plane displacements, as shown in Figure 2.4b [63,64].

The joint design also affects the stress concentration at the overlap ends. On the one hand, according to the model proposed by Ebnesajjad [65], for a constant overlap length, the joint shear strength increases linearly with joint width. On the other hand, in joints with constant width, the shear strength tends to increase non-linearly with the overlap length, gradually reducing the angular coefficient of the curve until a null value in which the shear strength will be constant and independent of the increase in length, as shown in Figure 2.5.

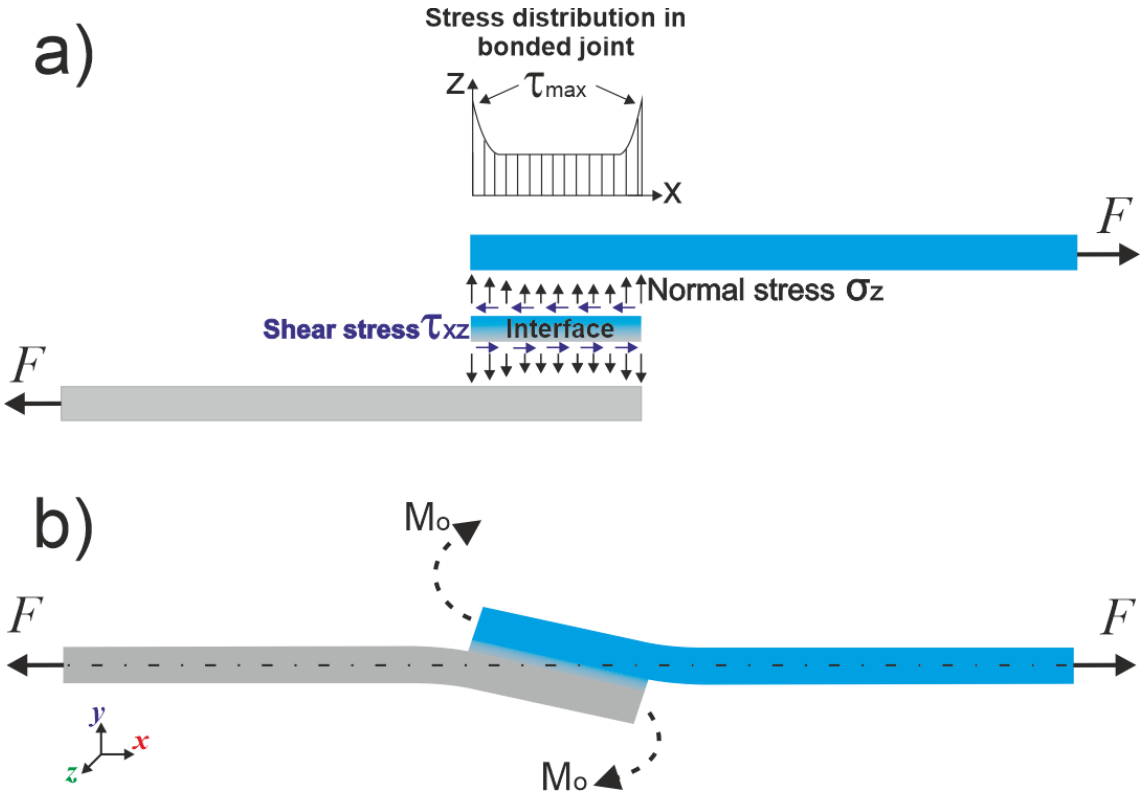

Figure 2.4: Bonded single-lap joint: a) Components of a single-lap joint and the stresses imposed when overloaded; b) deformation of a loaded single-lap joint and occurrence of the secondary bending moment. Adapted from references [63,64].

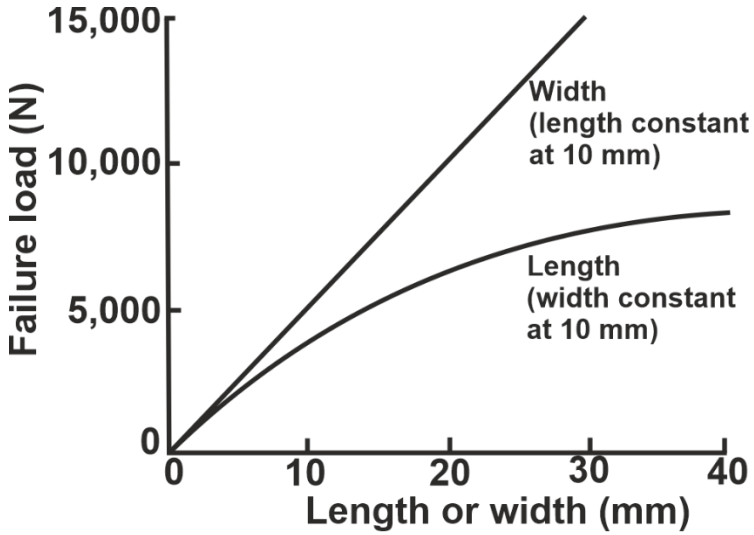

Figure 2.5: Effect of overlap and width on the shear strength of a typical single-lap joint. Adapted from reference [66].

The properties and the thickness of the individual components in the overlap joint will also change the peak shear stresses at the overlap area. On the one hand, joints with adherents with the same Young modulus decrease secondary bending and peel stresses, hence enhancing joint strength. A change in the maximum out-of-plane force is caused, on the other hand, by the disparity in stiffness between the bonded adherents [67]. Similarly, if two adherents of differing thicknesses are bonded together, the degree of secondary bending might vary throughout the interface. This is due to the adhesive stiffness, which will affect the thinner adherent more than the thicker adherent, resulting in non-uniform stress distributions and perhaps localized bending in the thinner adherent. In a bonded joint between adherents of different thicknesses, the thicker adherent will typically have a higher stiffness and resist bending more effectively than the thinner substrate. This can cause the thinner adherent to experience higher stresses and strains than the thicker one, which can lead to premature failure in the joint [68].

2.2.1 Failure mechanisms in polymer-metal joints

Polymer-metal joint failures are usually classified as cohesive, adhesive, or a combination of these (mixture failure) [69]. Figure 2.6a-d illustrates the failure

types of hybrid joints. The adhesive failure occurs at the interface between the polymer and metal, i.e., the polymer detaches from the metal, indicating weak adhesion between the components (Figure 2.6a). The cohesive failure occurs when the polymer-metal interface is more resistant than one of the joint materials (Figure 2.6b and Figure 2.6c). Depending on the particular strengths of each component and the joint geometry, cohesive failure may occur in either the polymeric or metallic component. The most frequent failure is a mix of adhesive and cohesive failures (Figure 2.6d). For effective bonding between hybrid parts, cohesive failure should predominate [70,71].

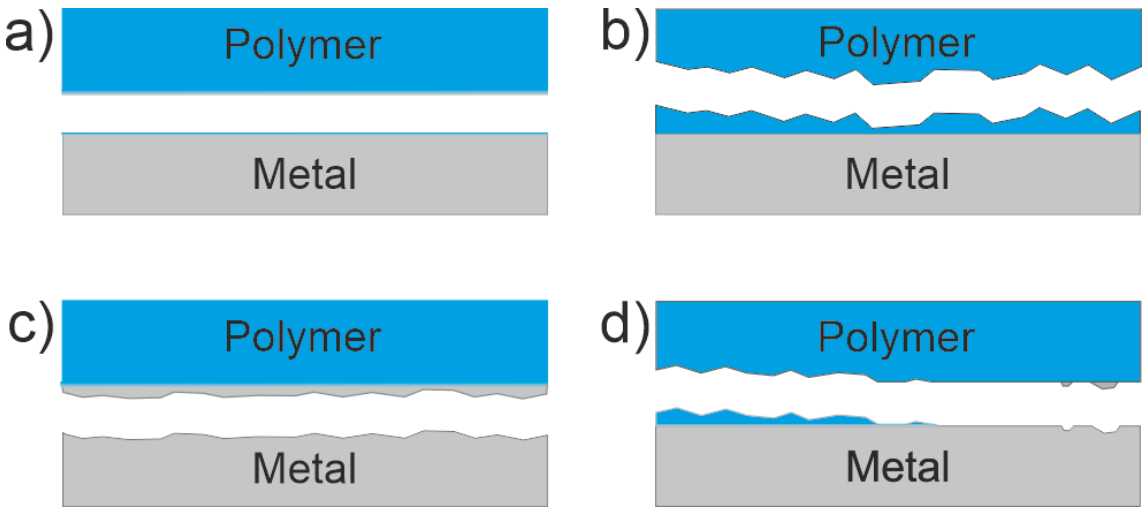

Figure 2.6: Schematic representation of failure types in direct-adhesion polymer-metal joints. a) Adhesive failure; b) Cohesive failure of the polymer part; c) Cohesive failure of the metal insert; d) Mixed failure (adhesive and cohesive). Adapted from reference [52].

When the interface bonding strength is larger than mechanical resistance of one of the individual components in an overlap polymer-metal hybrid joint, net-tension or stock-break failure takes place (Figure 2.7a) [72]. This global failure mechanism occurs, for instance when the adhesion mechanisms were improved at the interface to a larger level than the base material strength of one of the components or the overlap area was artificially increased to an extent resulting in a joined area larger enough, to shift the external loads to the individual components (or a combination of both phenomena) [73]. Moreover, tear-out

failure can take place when a component is subjected to a tensile force that exceeds the material or surrounding structure's strength. This results in a part of the material being forcibly removed or torn away from the surrounding material, resulting in a hole or tear in the material as shown in Figure 2.7b [72]. Any other global failure types taking place at the interface of a hybrid overlap joint are usually called delamination, as depicted in Figure 2.7c [74,75].

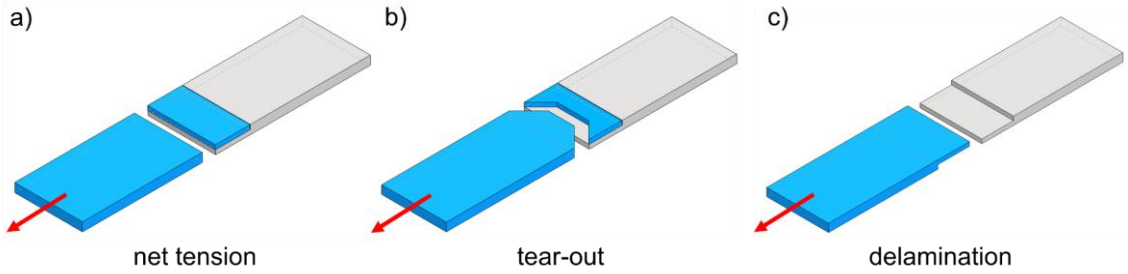

Figure 2.7: Schematics of global failures of a polymer-metal hybrid joint. a) net-tension (stock-break); b) tear-out and c) delamination. Source: Author.

2.3 Metal surface structuring technologies

Preparing the metal insert surface before joining it with the polymer is crucial for adhesion at the polymer-metal interface. This is an important manufacturing pre-step to achieving hybrid structures with excellent mechanical strength and durability [51,76] The methods of metal surface preparation can be categorized into three groups [76]: (i) Subtractive technologies, in which some material is removed from the metal surface to generate micro- or nanometric structures that increase the total surface area (such as micro-machining [77] abrasive blasting [62,78,79], laser texturing [80–85], and chemical etching [50,86–90]; (ii) Additive technologies, in which a component external to the polymer-metal system is added to the metal surface to increase interfacial strength by physical and/or chemical means; this includes additive manufacturing (powder-bed and directed energy deposition technique [91], welding surfacing (e.g. laser [92], arc-based [93] and friction surfacing [94], cold metal transfer [95]), electrochemical converting (e.g. electrolytic anodic oxidation or anodizing [56,96], and plasma electrolytic oxidation [97]), as well as chemical conversion (e.g.

phosphatizing [98] or adhesion promoter deposition (such as silanization [99–102]); and (iii) Formative technologies, often include plastically forming or shaping (e.g. embossing [103]), molding (e.g. Metal Injection Molding [104]) or using electrons or photons structuring (e.g. electron beam or laser surface structuring [105]) the metal surface to create protrusions or indentations without removing any material. A combination of these surface modification techniques, mixing the last two methods is a common practice to achieve improved mechanical (macrometric, micrometric or nanometric) interlocking and promote adhesion forces at the interface of the hybrid structure.

The following subtopics introduce the metal surface preparation techniques used in this work, namely, laser texturing and additive manufacturing.

2.3.1 Laser texturing

Laser texturing is a low-cost and rapid process for sculpting the metal surface of polymer-metal hybrid structures by using an optical system to focus the laser beam [106,107]; it is feasible to concentrate light energy in micro-sized regions, making it a high-precision micro-machining tool. The laser beam enables the application of various surface treatments for metals based on ablation, melting, and heating, to which lasers may apply with varied wavelengths and pulsed waves [108]. Microsecond and nanosecond laser pulses may efficiently ablate material off the metal surface. However, heat diffusion on the whole substrate may result in the vaporization of some metal alloy components. In contrast, picosecond and femtosecond pulsed lasers can lessen this heat effect on the microstructure of metals due to their much faster pulse duration than microsecond and nanosecond lasers, avoiding microstructure modifications on the metal surface [106].

The heat absorption significantly impacts the amount of material expelled during each laser scan. In general, metals are excellent heat conductors and sometimes show high surface reflectivity (e.g. aluminum alloys), requiring a higher heat input (i.e. higher laser energies) than polymers to form grooves with greater depth. The energy applied (Equation 2.3) in each laser pulse (E, in mJ) is specified by a correlation between the average laser power (P, in W) and the

laser operating frequency (F, in kHz). Controlling the laser settings allows for fine control over the surface structure height and geometry. Higher levels of laser power and lower operating frequency values provide great energy per laser pulse, promoting a deeper ablation with each laser scan [106].

$$E = \frac{P}{F} \qquad (2.3)$$

Figure 2.8a shows schematically the process of metal ablation by a pulsed laser. The metal reaches its vaporization temperature (T_v) due to the pulse high energy intensity. For most metals, the vaporization temperature (Tv) is around double the melting temperature (T_m). The surface temperature of the liquid metal, the liquid-vapor transition area, is significantly greater than the vaporization temperature; as a result, the vapor pressure (P_v) can reach high values, around 100 atm, when employing a pulsed laser with an intensity of 10^8 W/cm^2 [109]. This increased pressure at the liquid-to-vapor transition functions as a piston, pushing the liquid toward the microcavity boundaries. A portion of the ejected metal solidifies near the microcavity borders [110].

Figure 2.8b-c illustrates an example of a laser-structured aluminum surface in the form of grooves. The solidified portion on the groove top, indicated in Figure 2.8a and Figure 2.8c, is termed resolidified material and may increase the mechanical anchoring of the polymer on the surface and increase the mechanical strength. A laser beam with a high travel speed (500 to 2000 mm/s [111–113]) is frequently used to produce grooves on metal surfaces since it lowers the overlap area between irradiation regions and prevents the metal insert from becoming overheated, which might cause warping [114]. Rodríguez-Vidal *et al*. [14] demonstrated that the depth of the grooves and the height of the resolidified material sculpted on the surface of a steel substrate rose as the number of scans increased to a saturation point of 10 repetitions. Above this number, more remelted material was expelled from the cavity and deposited on the groove aperture, diminishing its width.

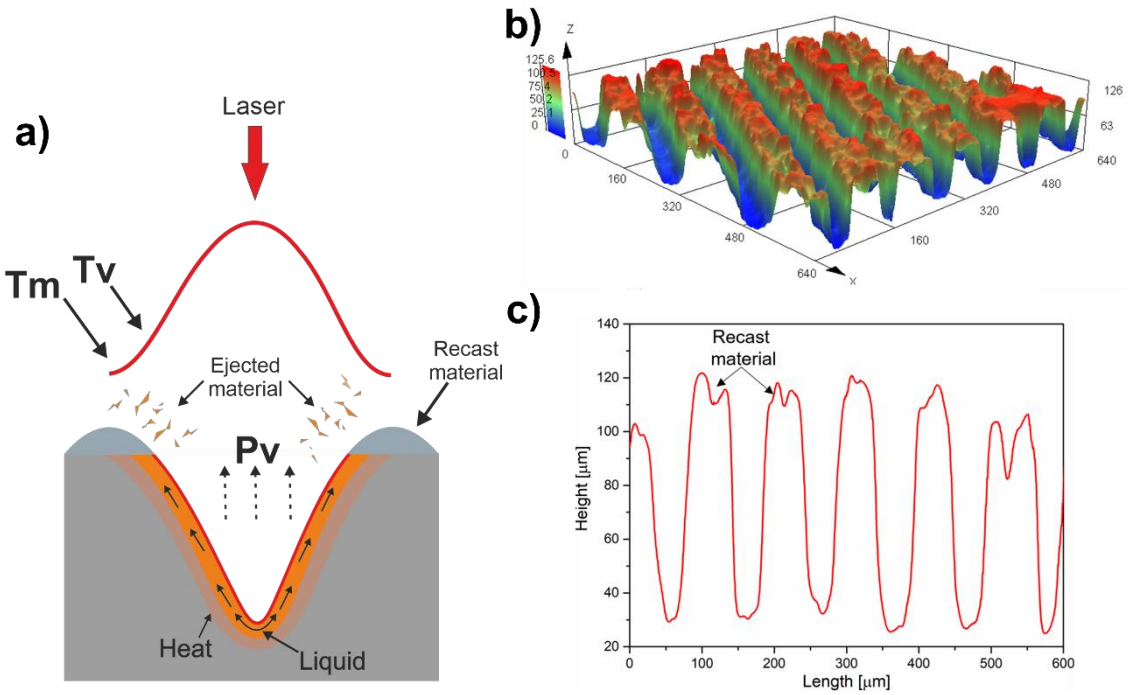

Figure 2.8: Laser texturing process and AA6061 laser textured surface. a) Schematic of the pulsed laser ablation process; b) 3D image of AA6061 surface obtained by laser confocal microscopy; c) profile of the metal surface; Laser texturing parameter was Ytterbium pulsed laser with laser power of 50 W, scan speed of 500 mm/s, frequency of 20 kHz and 3 laser scans. Source: The author.

The mechanism that contributes mainly to the high mechanical strength of injection overmolded polymer-metal joints is mechanical interlocking. The anchoring is accomplished by infiltrating molten polymer into the laser-formed grooves. However, the complete filling of these grooves is contingent on the injection settings being tuned for the polymer to infiltrate the grooves.

2.3.2 Additive manufacturing – Laser powder bed fusion

Additive manufacturing, often known as 3D printing, is based on constructing very complex geometries straight from computer-aided design (CAD) models without needing any tools.

Laser powder bed fusion (L-PBF) is an additive manufacturing process for metals, which is being increased selected as a tool to modify surface roughness [115–120] or add millimetric [43,45,121] and submillimetrical [16,91] features in

metals. The technology employs a high-intensity laser as an energy source to melt and fuse specific areas of metal powder, constructing a metal component layer by layer in an inert environment (nitrogen or argon gas) to prevent oxidation [122]. Figure 2.9 illustrates the L-PBF process and key process parameters [115,123], including laser power, laser scan speed, beam expander diameter (BED) or laser spot diameter, layer height, leaning angle and hatching distance. Consolidation of the part occurs by melting the powder particles or by diffusion bonding.

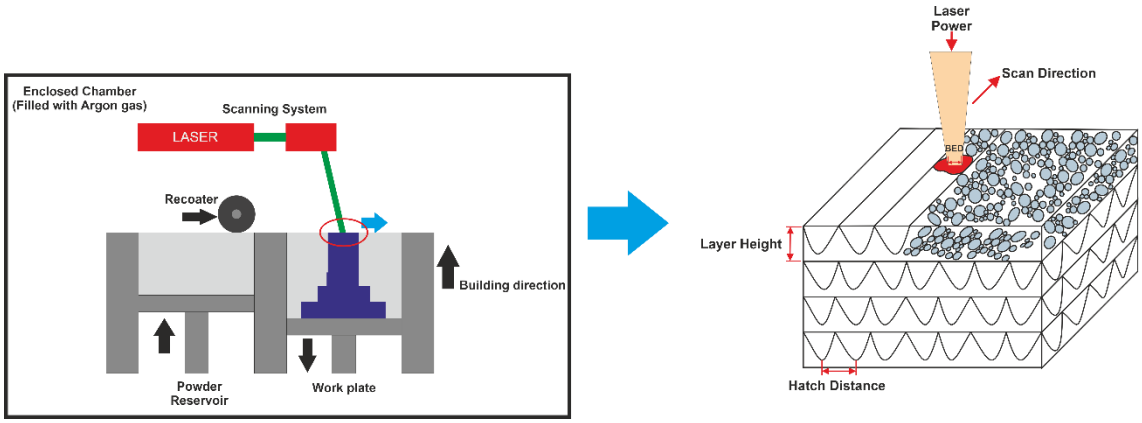

Figure 2.9: Schematic representation of laser powder bed fusion (L-PBF) components and main process parameters. Source: The author.

The control of the parameters of L-PBF allows for modifying the surface roughness of the melted region. Calignano at al. [124] investigated the influence of laser power, laser speed and spacing between the radiated points on the surface roughness of an aluminum alloy. The authors used the Taguchi method to determine the most influential process parameter and the surface of the samples was analyzed by scanning electron microscopy. The authors showed that the laser scan speed has a greater influence on the roughness than the other parameters studied. The higher the laser scan speed, the higher the average roughness (R_a). The increase in laser power and the distance between the radiated points also result in a higher value of average roughness (R_a) but with less influence when compared to the laser scan speed.

Figure 2.10 shows the correlation between laser scan speed and laser power on instability zones of L-PBF metal surface. On the one hand, low speeds

reduce the value of the average roughness (Ra) of the modified surface because it provides more heat and time for the surface irregularities to flatten by the effect of gravity before solidification [125]. On the other hand, very low speeds can increase the volume of liquid material due to the high temperature, generating more variation in surface stresses [125]. To reduce these differences in stresses, the liquid region can break into small pieces, also known as the "balling" effect, which solidifies at the surface of the liquid region. High-velocity values can improve the connection between the layers and increase the wettability of the molten region, reducing the variation in surface stresses. However, if the velocity is too high, abrupt vaporization of the melt can occur, disturbing the surface of the melt material, also known by the term "humping" [125,126].

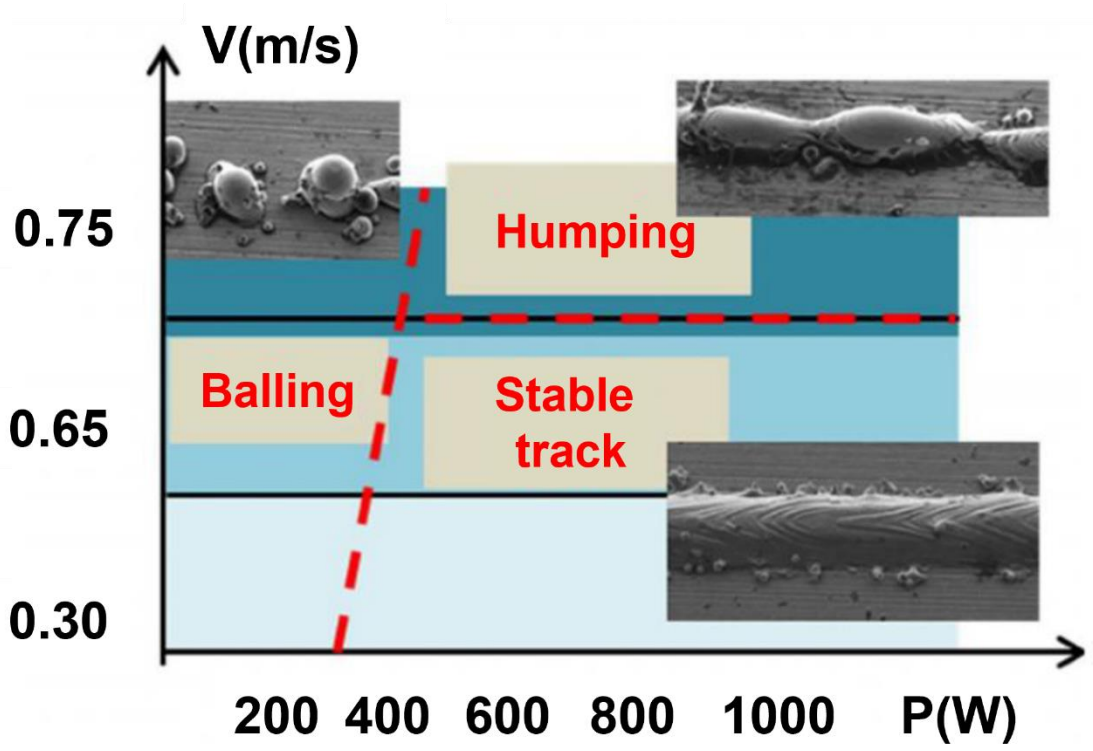

Figure 2.10: Correlation between laser scan speed (V) and laser power (P) indicating the instability zones of steel during L-PBF: "balling", "humping" and "stable track". Adapted from reference [125]

Skalon *et al*. [115] investigated the cause-effect between the stability of a melt pool and the roughness of an inclined, unsupported steel surface 3D-printed using the laser powder bed fusion technique. The authors observed that the melt-

pool varied in terms of its size, geometry, contact angles, and maximum length of stability as the angle of inclination of the unsupported surface increased. Moreover, using roughness measurements, the phenomena of balling was seen, measured, and compared; its geometry-dependent stability was impacted by the shape of the melt track. The authors suggest that a higher linear energy input reduces the roughness of unsupported surfaces with low inclination degrees, but a lower linear energy input might be more effective with higher inclination angles.

2.4 Injection overmolding of polymer-metal hybrids

2.4.1 Fundamentals of injection molding of polymers

Injection overmolding of polymer-metal hybrids is based on the injection molding of polymers. It is a highly automated method that enables manufacturing components with intricate geometries and high dimensional precision in seconds or a few minutes [76,127]. In polymer injection molding, polymer pellets are melted by thermomechanical action, forced through an opening (gate) into a closed mold, and then solidified in the form of the mold cavity. Figure 2.11 shows a schematic of a conventional injection machine containing three main components: (i) clamping unity, (ii) molding section, and (iii) injection unit.

The mold comprises at least two plates, one stationary and one mobile, each containing one or more: sprue, flow channel, gate, cavity with the shape of the final part and devices for ejecting the part from the mold cavity. The temperature of the mold is adjusted by electric heaters or a thermoregulator that circulates water or oil via channels within the mold. The clamping unit, hydraulic or electric, is responsible for the mold opening and closing actions and the ejection devices advance and retreat. The injection unit consists of an electric or hydraulic motor, and electrical or hydraulic system, a hopper, barrel (cylinder) and heating and cooling systems, a screw and an injection nozzle. The hopper feeds the polymer into the barrel/screw inlet, which is responsible for dosing and plasticizing before transferring the molten polymer to the mold cavity. The motor is responsible for screw rotation, while a hydraulic (or electrical) system is responsible for forward and reverse screw and barrel movements [128].

Polymer injection molding may be summarized in five sequential steps [129]: (i) dosing and plasticizing (melting/softening) of the polymer; ii) injection of the melted polymer into the mold cavity; iii) injection of additional material (holding or packing), by pressure and time control, to compensate for differential polymer shrinkage during cooling; iv) solidification of the polymer in the mold cavity by cooling; and v) extraction of the polymeric part from the mold The parameters of each step can be controlled to optimize the process and the final surface finishing and properties of the molded polymer part. In the dosing and plasticizing step, the barrel temperature, screw rotation speed and back pressure on the screw can be controlled. These are responsible for adjusting the degree of plasticizing and mixing and the temperature of the softened/melted polymer. In the injection stage, the injection speed (flow rate) is controlled by means of the screw forward movement, which is responsible for the shear rate and, therefore, for adjusting the polymer viscosity, as well as the degree of molecular orientation of the polymer. In the packing stage, the holding pressure and time are controlled, which are responsible for the dimensional accuracy, surface finish and internal stresses generated in the final part. In the cooling step, the temperature of the mold cavity and the residence time of the part inside the cavity is controlled, both of which influence the cooling rate and therefore, the surface finish and the degree of molecular orientation/crystallization of the polymer.

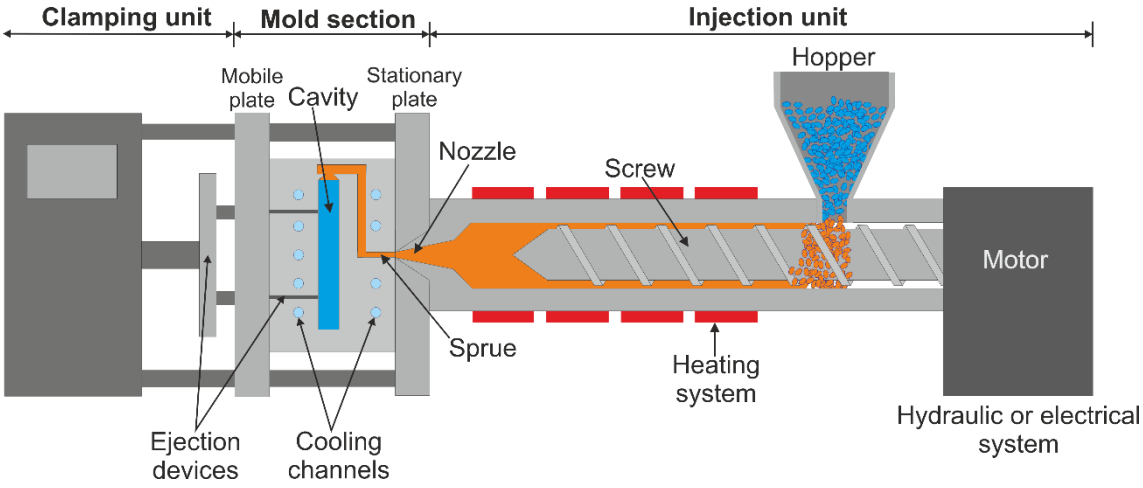

Figure 2.11: Schematic representation of a conventional polymer injection molding machine and components. Source: Author.

The filling of a rectangular mold cavity includes a complex non-isothermal transient flow [128], as seen schematically in Figure 2.12a-c (length L; width W; thickness H). During the earliest filling phases, the flow is radial and the melt front is circular (Figure 2.12a). As the melt front moves away from the gate, the flow pattern varies, so the front form is curved (for filling into molds with cold walls). Furthermore, the flow front deviates from a two-dimensional flow between parallel plates since shear forces impose a velocity gradient. The front flow material is pushed towards the cavity wall. This circulation pattern is known as "fountain flow" [128] (Figure 2.12b). The stretched outer surface of the melt front covers the inner wall of the cavity, whereas the subsequent melt mostly fills inside the fountain flow, resulting in a non-uniform polymer chain orientation pattern in the cross section of the molded item (Figure 2.12c).

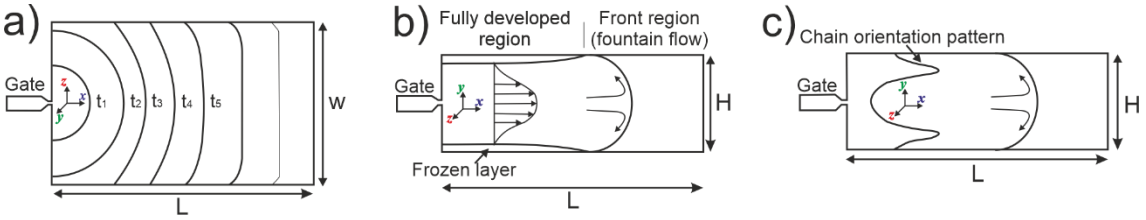

Figure 2.12: Schematic representation of the polymer flow pattern during filling a rectangular cavity with a length (L) and width (w) much higher than the thickness (H). (a) top view of the cavity to flow front at different times; b) Side view of the cavity with the flow velocity profiles in the fully developed region and representation of the front region, fountain flow effect; c) Polymer chain orientation across a section of the molded part. Adapted from reference [128].

In a fully developed flow in molds with cold walls, the shear rate is close to zero in the immediate proximity of the wall, reaches a maximum near the wall, and is extremely low in the core [130]. As a result of the fountain flow, the polymer layer originating from the central core of the flow front that experiences a constant elongation rate is deposited on the cold wall of the mold, where it solidifies and forms a "frozen (skin) layer" that retains a portion of the orientation caused by the elongation flow. The thickness of the frozen layer reduces as pressure, polymer

and mold temperatures and the part thickness increase. The layer that flows near the frozen layer and is subjected to high shear rates will solidify with a molecular orientation. The central core material, exposed to low shear rates, will solidify slowly, therefore relaxing and creating successive layers with very little molecular orientation [128,130,131].

2.4.2 Fundamentals of injection overmolding of polymer-metal hybrids

In injection overmolding of polymer-metal hybrids (PMH), a metal substrate (insert) is manually or automatically positioned inside the mold cavity at the beginning of the injection cycle, as shown in Figure 2.13. Following the insertion of the metal insert, the injection cycle continues as described previously, but with a more complicated melt flow front due to the varying thicknesses across which the polymer now flows. Furthermore, the surface temperature and thermal characteristics of the metal insert will influence the polymer-frozen layer on the metal insert. If the molten polymer meets a low-temperature metal insert, a thick solidified skin layer will occur, preventing the melt from infiltrating the metal surface features. Low temperature of the metal insert might additionally cause an unequal cooling rate of the polymer melt, resulting in residual stress at the bonding surface. On the other hand, if the metal insert is heated to a high enough temperature, the solidified skin layer will be thinner, which promotes the filling of the metal surface features by the melt and enhances the interfacial adhesion.

Using injection overmolding to manufacture polymer-metal hybrid structures was first introduced by Bayer, now Lanxess, in 1996 [132]. By the Bayer design, a stamped metal containing through holes is placed inside the mold cavity and overmolded with molten polymer, producing a metal structure reinforced by polymer ribs. In this case, the polymer-metal hybrid structures are predominantly formed by mechanical interference through rivets by filling the polymer into the through holes of the stamped metal structure. Although the technique provides good polymer-to-metal bonding, there might be problems related to fatigue of the polymeric material in the regions where the fasteners are formed due to the high concentration of stresses at the site.

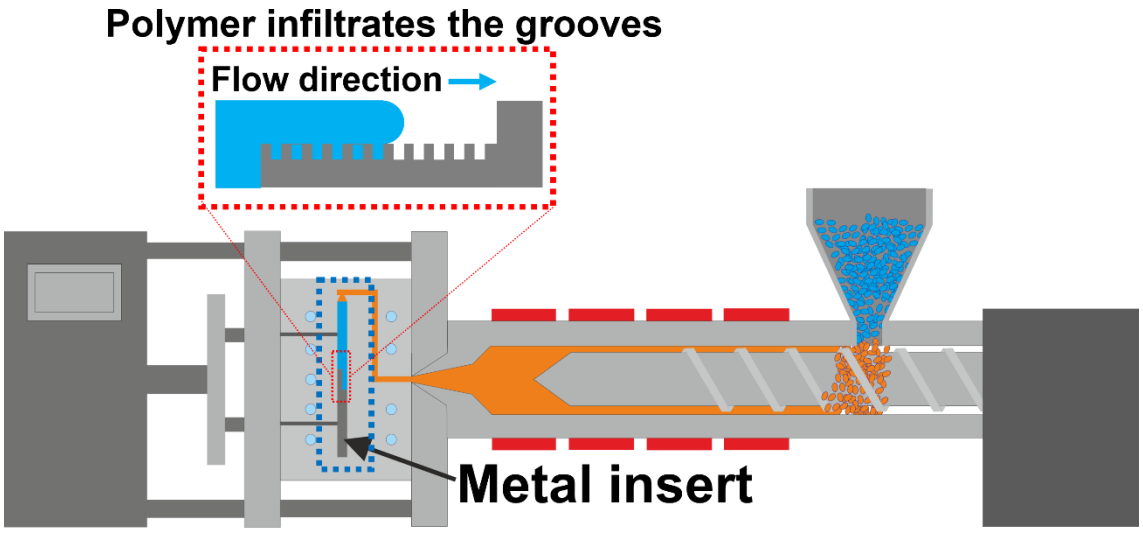

Figure 2.13: Schematic representation of a conventional polymer injection overmolding machine used for the injection overmolding process of polymer-metal hybrid structures. Detail to the metal insert positioned inside the mold cavity and the polymer-metal interface. Source: Author.

The joining of metal inserts with polymer based on injection overmolding has also been explored by Dow Automotive [131] and introduced in 2003 in front-end modules of Volkswagen automotive prototypes [133]. This injection overmolding methodology employs two consecutive steps, where the stamped metal and the polymer (previously injection overmolded), are joined by adhesive. This process variant has some disadvantages in relation to the others, such as the adhesive curing time for the finalization of the part and lower chemical resistance and durability.

The technique of polymer injection overmolding on metal insert with direct-adhesion ('direct-adhesion polymer-metal-hybrid technology [127]) presents itself as a viable alternative to circumvent the shortcomings of conventional injection overmolding techniques mentioned above. With the direct-adhesion process variant, the polymer component is bonded to the metal insert without the need for previous drilling of the metal insert or adhesive application. In the case of the direct-adhesion technique, the joining is achieved utilizing micro-mechanical anchoring generated by filling of the molten polymer with subsequent solidification on the surface irregularities purposely drawn on the metal insert

surface; Moreover, adhesive forces (Section 2.1) are also promoted at the polymer-metal interface. Additionally, good adhesive forces can be also achieved through application of adhesion promoter on the metal surface; this will induce covalent bonds with the injection overmolded polymer [57,76]. The direct-adhesion technique presents considerable advantages over other manufacturing methods based on injection overmolding, such as no need of placing through holes in the metal structures for polymer filling and the formation of fasteners, which may compromise the mechanical performance of the hybrid structure. Polymer-metal hybrid structures with high interfacial strength between components fabricated by this technique can be obtained via optimization of process parameters, chemical modification of the polymer and/or surface treatment of the metal [49,133].

2.4.3 Effects of injection overmolding parameters and metal surface structure on the joining strength of polymer-metal hybrid structures

The effects of injection overmolding process parameters and metal surface structure on the joining strength of polymer-metal hybrid joints produced via injection overmolding with direct-adhesion have been the subject of some studies. The published results available in the literature have been compiled in a review manuscript by the author and co-authors published elsewhere [76].

Data related to injection overmolding conditions and the metal surface treatments used in this PhD thesis, among others, are summarized in Table 2.1 and described below.

The study of Ramani and Moriarty [134] was one of the pioneers in injection overmolding with direct-adhesion. They investigate the joining of polycarbonate (PC) on AA6061-T6 alloy insert previously treated by abrasive blasting. Using a full-factorial (2^k) experimental design of experiments (DoE), the authors investigated the influence of the temperature of the contact surface of the insert with the polymer, injection speed and pressure on the tensile strength of butt joints. The authors were unable to produce joints without preheating the metal insert and identified that the insert temperature has the greatest influence on the tensile strength of the joints. It was observed by scanning electron

microscopy that the increase in insert temperature allowed the polymer to infiltrate the metal microcavities produced by abrasive blasting. The authors showed that the tensile strength of joints increases by 15% for every 13 °C increment in insert surface temperature.

Table 2.1: Materials, techniques of metal surface preparation, processing parameters, and mechanical strength of direct-adhesion injection overmolded polymer-metal hybrid joints.

Polymer component	Metal component	Metal surface preparation	Processing conditions	Joining strength*	Reference
PP-30-50GF PPS-40GF	AA6082	Corundum blasting	Injection speed [80 – 120 mm/s] Metal preheating temperature [300 – 450 °C]	0.58 – 0.97 MPa	[53]
PP	AA6061	Sandblasting	Metal temperature [60 – 150 °C]	Up to 250 N (overlap area of 10 × 15 mm²)	[62]
PC	AISI 1018 AA6061-T6	Grit blasting	Injection speed [5.8 – 10.688 cm/s] Holding pressure [129 – 190 MPa] Metal temperature [170 – 204 °C]	20.4 – 38.5 MPa (tensile testing, butt joint geometry)	[134]
PP	AA6061	Sandblasting	Metal temperature [60 – 150 °C]	Up to 248 N (overlap area of 10 × 15 mm²)	[78]
PPS-30GF	AA6061	Sandblasting	Metal temperature [30 – 150 °C]	56 – 652 N (overlap area of 10 × 15 mm²)	[79]
PBT-30GF	AA5052	Anodizing	Injection speed [10 – 300 mm/s] Packing pressure [20 – 110 MPa]	4 – 22 MPa (overlap area of 5 × 10 mm²)	[56]
ABS-30GF	Stainless steel	Embossing and laser structuring	Injection speed [100, 70, 150 and 180 mm/s] Packing pressure [60, 150 and 80 MPa]	Up to 2302 kPa (overlap region of 50.8 × 25.4 mm²)	[135]
PBT-30GF	AA5052	Laser structuring	Packing pressure [20 – 100 MPa]	14 – 23 MPa (overlap area of 5 × 10 mm²)	[84]

			Holding pressure [0 and 50 MPa] Melt temperature [220 – 245 °C]		
PC PMMA	AA50552	Laser structuring	Packing/holding pressure [80/60, 50/37.5 and 20/15 MPa] Injection speed [10, 50 and 100 mm/s]	Up to 30 MPa (overlap area of 5 x 10 mm²)	[83]
PPS-40GF	DIN 1.4301	Laser structuring	Not shown	300 – 1150 N (overlap area of 100 mm², double-lap joint geometry)	[80]
PA-35GF	Steel (grade HC 340/590DP)	Laser structuring	Kept constant	12.4 – 27.8 MPa (5 × 10 mm²)	[136]
PA66	EN AW-6082-T6	Laser structuring	Kept constant	Up to 11.9 MPa (overlap area of 25 × 12.5 mm²)	[81]
PBT-30GF	AA5052	Laser structuring	Kept constant	Up to 18 MPa (overlap area of 5 × 10 mm²)	[82]
PBT-30GF	AA5052	Laser structuring	Kept constant	Up to 22.4 MPa (overlap area of 5 × 10 mm²)	[85]
PAEK-GF	316L	Additive manufacturing	Not shown	Up to 73.8 MPa (overlap region of 5 × 5 mm², pull strength)	[91]

* Values determined by lap-shear testing by tensile loading, except when specified.

Li *et al*. [78] investigated the effects of metal surface temperature on the joining strength of single-lap joints using polypropylene (PP) and 6061 aluminum alloy. The sandblasted metal inserts had an average surface roughness (R_a) of 4.3 µm. During the injection cycle, the metal surface temperature was regulated using a custom-designed temperature control system consisting of heating rods and cooling tubes inserted within the mold. The authors showed that adhesion could not be achieved between PP and AA6061 at metal surface temperatures below 60 °C. This outcome was correlated with the formation of a thick solidified skin layer upon contact between the molten polymer and the cold metal surface; this prevented the polymer from filling the metal surface microstructures. In

contrast, PP and AA6061 were successfully joined at higher metal temperatures, with the joining strength improving steadily as the metal temperature increased up to 150 °C. This led to the formation of a thinner, solidified skin layer and facilitated the filling of surface microstructures. Furthermore, Li *et al*. [79] demonstrated in another work involving poly phenylene sulfide (PPS-30GF) and sandblasted AA6061 substrate that the joint strength increases with higher values of temperature and roughness in the metal insert. The authors attribute this increased mechanical strength to the filling of polymer into the roughness crevices and better polymer micro-interlocking at higher average roughness values.

Kadoya *et al*. [56] evaluated the effects of injection speed and packing pressure on the joining strength of PBT-30GF/AA5052 single-lap joints. Metal insert was first cleaned with 5 wt% NaOH and 30 wt% HNO_3 to remove the natural oxide layer and then anodized in a 5 wt% solution of phosphoric acid (H_3PO_4) at 15 °C, under a potential of 50 V for 30 or 60 minutes to produce a nanostructured layer with average pore diameters of 50 and 70 nm, respectively. Scanning transmission electron microscopy (STEM) analysis revealed that the overmolded polymer infiltrated the nanopores on the metal surface, albeit the filling depth was significantly less than the pore depth. As injection speed increased, joining strength decreased, which was linked to probable nanopore structural degradation. In addition, the joining strength increased somewhat with increasing packing pressure for the slower injection speed (10 mm/s), which was correlated with a higher degree of pore filling.

Kim and Lyu [135] manufactured single-lap joints of glass-fiber reinforced acrylonitrile-butadiene-styrene (ABS-30GF) and stainless steel. Metal surface was nickel electroplated with glass beads, ceramic beads, synthetic diamond particles, and aluminum oxide particles. The authors employed three diameter ranges for each particle set, resulting in embossed metal surfaces with varying patterns. Additionally, laser engraving was used to form grooves on the metal surface. In this instance, the authors altered the laser head angle (45°, 90°, and 135°), which resulted in distinct patterns on the metal surface at a depth of around 100 µm. Four levels of injection speed (100, 70, 150, and 180 mm/s) and three

levels of packing pressure (60, 150, and 80 MPa for 2, 6 and 2 s, respectively) were investigated. For embossed metal surfaces, plating with aluminum oxide particles resulted in maximum adhesive strength (average of 2.3 MPa for the bigger particles set). The result is attributed by the authors to the irregular form and rough surface of these particles, which increased the contact area between polymer and metal and produced recesses on the metal surface. The maximum adhesive strength (1.5 MPa) was found for laser-engraved metal surfaces with a 45° laser head incidence angle and a right-angle cross pattern. This outcome was also linked to the formation of recesses on the surface of the metal, which offers mechanical interlocking between the polymer and metal.

Zhao *et al*. [84] investigated the effects of packing and holding pressures, as well as polymer melt temperature, on the lap-shear strength of PBT-30GF/AA5052 single-lap joints. Using a nanosecond pulsed laser, micrometric dimples with a fixed aspect ratio (depth/diameter) of 1.5 were placed in a square pattern on metal inserts. The authors studied two groups of molding conditions: one with varying packing pressures from 20 MPa to 100 MPa and polymer temperatures from 220 °C to 245 °C, and another group with changing holding pressure from 0 MPa to 50 MPa and polymer temperatures from 230 °C and 245 °C, with a constant packing pressure of 100 MPa. For a packing pressure of 20 MPa, the joining strength increased as the polymer temperature increases.

Zhao *et al*. [83] examined the effects of injection overmolding parameters and the mechanical anchoring of amorphous polymers (polycarbonate - PC and poly(methyl methacrylate) - PMMA) onto laser-textured aluminum (AA5052). Holes of 50 µm in diameter, 100 µm in-depth, and spaced 60 µm apart were laser ablated into the metal surface. The injection speed varied between 10 mm/s and 100 mm/s, the packing pressure varied between 20 MPa and 80 MPa, and the holding pressure varied between 15 MPa and 60 MPa. Other parameters were kept constant. The authors found that high joining strength was achieved using high packing pressure and injection speed values. For a packing/holding pressure of 80/60 MPa, the ultimate lap-shear strength increased from 7.5 MPa and 5.5 MPa at 10 mm/s to 30 MPa and 20 MPa at 100 mm/s for PC and PMMA, respectively. This increased mechanical strength was attributed to increased

filling of the polymer into the grooves formed on the metal surface. Moreover, a linear increase between polymer filling depth and ultimate lap-shear strength was observed.

Byskov-Nielsen *et al*. [80] structured the metal surface using a nanosecond pulsed laser treatment in double-lap joints of glass-fiber reinforced poly(phenylene sulfide) (PPS-40GF) and stainless steel (DIN 1.4301). The laser treatment produced holes with a 110 µm diameter, 20–225 µm depth, and 100–300 µm spacing between holes. The conditions for injection overmolding were not supplied. According to the authors, the joining strength decreased as the distance between holes increased with hole depth up to 100 µm. A larger distance between the holes reduces the number of holes where the polymer can infiltrate and micro-mechanically anchor.

Huang *et al*. [136] utilized nanosecond pulsed laser treatment to produce periodic holes on the metal surfaces of single-lap joints with glass-fiber reinforced polyamide (PA-35GF) and steel (grade 340/590 DP). The distance between neighboring holes varied between 50 µm and 300 µm. Prior to being placed into the injection mold, metal inserts were heated to 350 °C and maintained at a mold temperature of 90 °C. The conditions for injection overmolding were held constant. Using a line point pattern (ratio between hole diameter and distance between adjacent holes), the authors noted that joining strength increased as surface roughness and distance between consecutive holes increased, reaching a maximum value (27.8 MPa) for a line point pattern of 1:3. According to the authors, the surface roughness improves the adhesive strength as a result of the increased effective contact area between the polymer and metal once the surface holes are produced.

Gebauer *et al*. [81] employed cw and pw laser treatments to structure the metal surface in single-lap joints of polyamide 66 (PA66) and 6082-T6 aluminum alloy, producing trench patterns with hatch distances of 150 µm and 100 µm and depths of 158 µm and 40 µm. Optimized injection overmolding settings were constant. Continuous wave laser (cw) structured metal surfaces led to joining strengths up to 11.9 MPa, whereas pulsed wave laser (pw) structured surfaces had no adhesion with polymer. The authors attributed this to the deep and rough

pits in the cw laser structured surfaces that compensates for volumetric shrinkage during solid solidification, resulting in good polymer-metal adhesion.

Enami *et al*. [82] used picosecond, nanosecond, and cw laser treatments to produce periodic dimples at square lattice vertexes on 5052 aluminum alloy surfaces to manufacture single-lap joints of glass-fiber reinforced poly(butylene terephthalate) (PBT-30GF) and AA5052. The authors examined how dimple sizes (40 μm – 80 μm) and aspect ratios (depth/diameter; 0.9 to 1.9) affected joining strength using the nanosecond laser. Injection overmolding parameters were constant. For the same structured area, specimens with smaller-diameter dimples had 10% higher joint strength. The load imparted to each polymer-filled dimple reduced as the number of dimples increased. The joining strength was positively correlated with the aspect ratio up to 0.6, but greater values did not appreciably alter it, even when the polymer entirely filled the dimples. According with the authors, polymer-metal adhesion at the dimple bottom had a minimal influence on joining strength. The picosecond laser treatment, which produced the most dimples, had the highest joining strength (18 MPa) for the same structured area.

Xu *et al*. [85] used a 355 nm ultraviolet (UV) laser to texture square grid-shaped grooves on the metal surface with line spacing of 30–240 μm, depth of 22–29 μm, and average width of 17 μm to evaluate the joining strength of PBT-30GF/AA5052 single-lap joints. Grid-shaped micro-level polymer rivets were formed after injection overmolding at constant parameters. At 30 μm line spacing, the joining strength reached 22.4 MPa. The aluminum alloy surface had 95.3% residual PBT-30GF, indicating cohesive failure through polymer interface fracture.

Verma *et al*. [91] used additive manufacturing to build lattice structures over a 316 L (stainless steel) substrate that function as mechanical interlocking components for injection overmolded glass-fiber reinforced polyaryletherketone (PAEK-GF). Body-centered cubic with z-axis reinforcement (BCCZ), cubic face-centered (CFCC) and truncated octahedron (Kelvin) lattice structures are three forms of struts-based unit-cell topologies with varying relative densities that were produced using L-PBF method. The injection overmolding parameters were not

shown. The authors employed tensile testing to determine the pull strength of the hybrid joints and finite element analysis (FEA) to simulate the polymer lattice assembly. The authors ascribed the disparities between FEA and experimental results to internal faults or porosities in the lattice structures produced by L-PBF process constraints. Experimental testing and FEA modeling yielded the highest pull strength for BCCZ struts (0.25 mm diameter and 29% relative density). The experimental pull strength was 73.8 MPa, with a mixed failure ratio of polymer and lattice. The pull strength estimated by FEA modeling was 85.34 MPa, with lattice failure. The authors ascribed BCCZ lattice superior performance to the absence of horizontal struts, which are susceptible to defects depending on SLM process settings and machine resolution.

Although these studies guide the influence of important injection overmolding parameters on the interfacial strength of the state-of-the-art polymer-metal joints, there are still gaps regarding the long-term performance of these joints, including fatigue and hygrothermal stability. Moreover, the hybridization by injection overmolding with direct-adhesion of polymer to metal inserts produced by additive manufacturing is very scarce. Finally, a detailed understanding study on the correlation between processing parameters, structures and properties is missing for a combination of diverse engineering materials, such as polycarbonate with rolled aluminum alloy 6061 and additive manufacturing alloys (e.g. AlSi10Mg).

2.4.4 Advantages, limitations and potential applications

The main advantages of injection overmolding over conventional mechanical fastening and adhesive bonding of PMHs are: (i) weight reduction due to the absence of mechanical fasteners or the addition of adhesives; (ii) absence of volatile compounds related to adhesives composition and fasteners that contributes to sustainability; (iii) high capacity to produce polymer-metal hybrid structures in a few seconds or minutes; (iv) suitable for a wide range of different materials, such as thermoplastic polymers, thermosets, and elastomers; (v) high freedom to produce structures with complex geometry design; (vi) improved or comparable quasi-static and dynamic mechanical performance. The

main limitations of the process are [137,138]: (i) high upfront costs for injection mold manufacturing; (ii) metal insert surface treatment is required (e.g., laser treatment); (iii) more energy expended due to higher process temperatures and heating of the metal insert.

Due to the advantages presented, injection overmolded polymer-metal hybrid structures have a high potential to replace all-metal components in many sectors, such as transportation, household, biomedical devices and electronics. There are several existing uses of injection overmolded polymer-metal hybrid structures in various fields and more future applications, as outlined below.

Vehicle weight reduction is a hot topic in the automotive sector for reducing greenhouse gas emissions and increasing the payload for heavy vehicles. It is estimated that fuel consumption is reduced by 7% for every 10% reduction in vehicle weight [139]. Furthermore, with the advent of electric cars and the European Union decision to zero CO_2 emissions from cars by 2035 [140], the need for lighter vehicles to compensate for the weight of the charge cells in the batteries is growing [138]. The Trelleborg Group, a global pioneer in engineered polymer solutions, designed a hybrid automobile brake pedal that combines a metal component with glass-fiber reinforced polyamide (GFRP) [141]. The procedure produces the final and full assembly in a single step. This new method of producing brake pedals saves 30% to 50% of the weight compared to an all-metal component while maintaining mechanical strength and durability and removing the costly metal stamping process [137]. Moreover, Mercedes-Benz produced a new front-end for cars manufactured by reducing weight by up to 40% and production costs by 20% through using an aluminum framework overmolded with glass fiber reinforced polyamide composite.

2.5 Materials Survey

2.5.1 Polycarbonate

Polycarbonate (PC) is an engineering thermoplastic widely used in the automobile industry due to high stiffness, strength, impact resistance and transparency allow it to replace windshields and headlamp housings [142]. In

addition, it may be combined with other polymers in blends or composites with other automotive applications [143,144].

PC is synthesized by polycondensation between Bisphenol A and phosgene [145,146]. The molecular structure of PC is shown Figure 2.14. On the one hand, the phenylene groups are responsible for the stiffness of the thermoplastic as well as a low index of crystallinity, high transparency, and dimensional stability. On the other hand, the isopropylidene and carbonate groups provide greater mobility to the molecular chain, contributing to its high toughness and impact resistance [147].

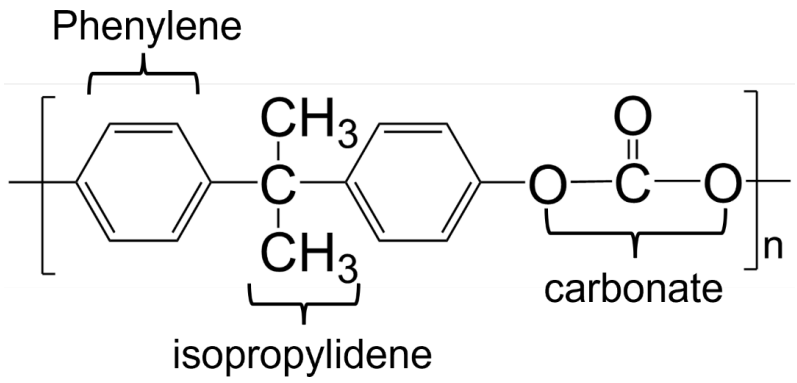

Figure 2.14: Molecular structure of PC produced from Bisphenol A. Source: Author.

In addition to its excellent transparency and mechanical properties, polycarbonate is extremely moldable via extrusion and injection molding. Moreover, it features excellent thermal stability, minimal water absorption, and low flammability [148].

2.5.2 Aluminum alloy 6061-T6

AA6061 aluminum alloy is a general-purpose metal produced in different shapes that enables countless applications in different sectors, from truck and railcar structures to aerospace and construction applications. This application versatility is due to its good mechanical properties and corrosion resistance [6].

AA6061 is a precipitation-hardenable alloy with magnesium and silicon as its main alloying elements. The nominal chemical composition of this alloy is shown in Table 2.2. The mechanical properties are highly dependent on temper, ranging from 125 MPa to 290 MPa in ultimate tensile strength for AA6061-O (annealed) and AA6061-T6 (solution treated and artificially aged), respectively [6,149]. However, Young modulus remains at 69 MPa regardless of the tempering [6]. After solubilization and tempering, the T6 heat-treated AA6061 material, which is one of the most used in the automotive industry, goes through artificial aging at temperatures. The T6 heat treatment induces the formation of β''-phase. ($AlSiMg_2$) as the primary precipitation phase of hardening, which leads to higher mechanical strength [150,151].

Table 2.2: Nominal chemical composition of AA6061 [6].

AA6061	Composition (wt%)							
	Si	Mg	Cu	Mn	Fe	Cr	Zn	Unspecified other elements
	0.40-0.80	0.8-1.2	0.15-0.40	0.15	0.70	0.04-0.35	0.25	0.35

2.5.3 AlSi10Mg

AlSi10Mg alloy belongs to the Al-Mg-Si casting alloy system and is utilized extensively in the automotive, aerospace, and electronic sectors [6]. Due to its optimal casting qualities, low weight and thermal expansion coefficient, and high mechanical strength, this alloy is a good alternative to cast iron for fabricating components [152]. Moreover, since the advent of additive manufacturing, AlSi10Mg powder alloys have been commonly employed to construct intricate geometries in additively manufactured components [153].

The main alloying elements are silicon and magnesium, with additional elements present in amounts less than 1 wt% (Table 2.3). This aluminum alloy can undergo various heat treatments to improve mechanical properties, such as annealing and typical T6 heat treatment [154]. Other methods, such as hot isostatic pressing (HIP), can be utilized to minimize the internal porosity of additive manufactured AlSi10Mg parts [155,156].

Table 2.3: Nominal chemical composition of AlSi10Mg [6].

AlSi10Mg	**Composition (wt%)**							
	Si	Mg	Cu	Mn	Fe	Ti	Zn	Unspecified other elements
	9 – 10	0.20 – 0.45	< 0.05	< 0.45	< 0.55	< 0.15	< 0.10	< 0.20

3. MATERIALS AND METHODS

3.1 Experimental approach

This PhD work was divided into two parts, as illustrated in Figure 3.1.

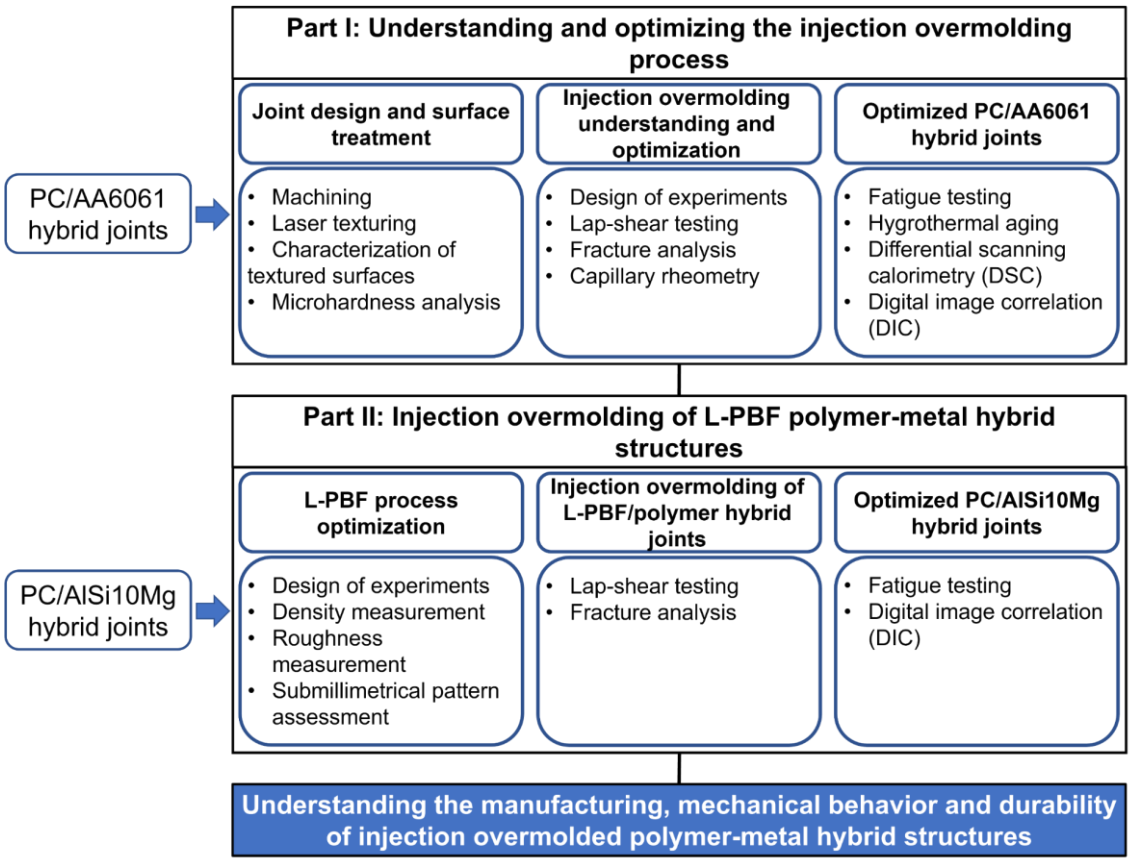

Figure 3.1: Experimental approach of this thesis.

In Part I, polycarbonate (PC) with 6061-T6 aluminum alloy joints were produced by injection overmolding with direct-adhesion and characterized. AA6061 rolled sheets were cut and machined in the form of specimens and subsequently textured with a pulsed laser to obtain deep grooves in the overlap joining surface. The injection overmolding joining process was optimized with a DoE followed by an analysis of variance (ANOVA). Three injection overmolding parameters that play a key role in the interfacial strength of polymer-metal joints were varied: barrel temperature, injection speed and holding pressure. The response value was the ultimate lap-shear force (ULSF) of the PC/AA6061 joints. Moreover, the fracture mechanisms of the PC/AA6061 joints were evaluated by scanning electron microscopy (SEM) and laser confocal microscopy.

Furthermore, the filling of polymer into the metal grooves formed by the texturization was correlated to the PC melt viscosity measured by capillary rheometry. In a further step, PC/AA6061 joints prepared with optimized injection overmolding parameters were subjected to hydrothermal aging and fatigue testing. Digital image correlation (DIC) was also employed to determine the displacement and stress distribution in the joints during lap-shear testing.

In Part II, the feasibility of metal additive manufacturing by laser powder bed fusion (L-PBF) was evaluated to produce AlSi10Mg substrates with submillimeter structures on the surface. For this, a DoE and ANOVA were employed on five important parameters for laser powder bed fusion to optimize the AM parts: laser power, laser scanning speed, laser spot diameter, layer height and hatching distance. The intrinsic roughness owing to the printing process in addition to three submilimetrical structures (i.e., as-built, inkpot, lattice and mushroom geometries), was explored. From the response values, the density of AM specimens was maximized. The level of defects on the substrate surface and in the submillimeter structures was also considered for the choice of the optimal printing parameter. The AM parts were produced using the optimized L-PBF parameters at various printing angles, and the resulting process-related surface roughness was measured. PC/AlSi10Mg joints were manufactured using the optimized injection overmolding parameters. All PC/AlSi10Mg with different submilimetrical structures were submitted to lap-shear testing. DIC was used to evaluate the joint mechanical behavior. The joint with the highest average lap-shear strength was selected for fatigue testing following the same approach adopted in Part I. A detailed description of materials and methods is provided in the following sections.

3.2 Materials

3.2.1 Polycarbonate

The polymer component used for injection overmolding was polycarbonate (PC), grade LEXAN 103, with a melt flow rate of 7 g/10min (ASTM 1238: 300 °C; 1.2 kg) and UV-protection additive supplied by SABIC Innovative Plastics, Brazil.

PC is an amorphous engineering thermoplastic widely used in automotive parts and household appliances that combines high stiffness, strength and toughness, good dimensional stability, and optical transparency. In addition to the engineering relevance of this polymer, it was selected due to the high intrinsic transparency, therefore allowing for an easier visual inspection of the joint overlap area after processing. Selected properties of PC are shown in Table 3.1.

Table 3.1: Selected physical and mechanical properties of LEXAN 103 [157].

Property	Value
Young modulus	2.35 GPa
Tensile strength	65 MPa
Yield strength	62 MPa
Strain at break	110 %
Density	1.19 g/cm^3
Thermal conductivity at 25 ^{o}C	0.19 W/m.°C

3.2.2 AA6061-T6

AA6061-T6 rolled sheets produced by Alcoa, USA were used in this work. The alloy properties of interest are shown in Table 3.2. AA6061-T6 was selected due to its widespread use in general applications, such as trucks, towers, canoes, railroads cars, pipelines and other structural applications where needed strength, weldability, and corrosion resistance.

Table 3.2: Selected physical and mechanical properties of AA6061-T6 [6].

Property	Value
Elastic modulus	68.9 GPa
Tensile strength	310 MPa
Yield strength	276 MPa
Strain at break	12 %
Shear strength	207 MPa
Fatigue strength at 10^8	97 MPa
Density	2.7 g/cm^3
Thermal expansion linear coefficient in the range 20 - 100 °C	23.6 µm/m.K
Thermal conductivity at 25 ^{o}C	167 W/m.k

3.2.3 AlSi10Mg

AlSi10Mg spherical powder (Figure 3.2) supplied by ECKART TLS (ALTANA, Germany). with a particle size distribution of 25 – 65 µm (D_{50} = 30-40 µm) was used to produce the metal insert by L-PBF. The AlSi10Mg was selected due to its relevance for lightweight industrial application and proven 3D-printability by L-PBF. Properties of interest are given in Table 3.3.

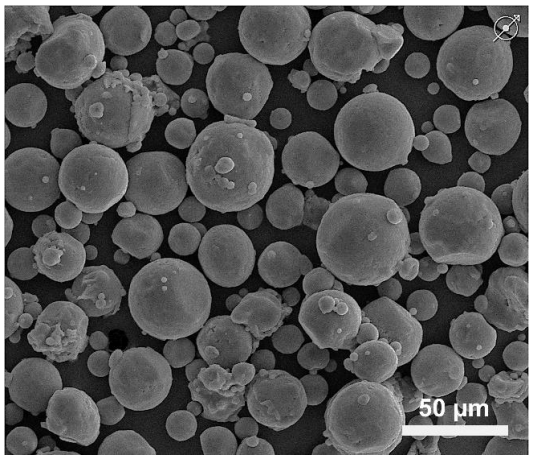

Figure 3.2: Scanning electron microscopy (SEM) micrograph of AlSI10Mg powder (D_{50} = 30-40 µm). Source: Author.

Table 3.3: Selected physical and mechanical properties of AlSi10Mg cast test bars [6].

Property	Value
Tensile strength	305 MPa
Yield strength	170 MPa
Strain at break	2.5 %
Shear strength	190 MPa
Elastic modulus	71 GPa
Fatigue strength at 10^{8} *	140 MPa
Density	2.63 g/cm^3
Thermal expansion linear coefficient in the range 20 – 100 ^{o}C	21 µm/m.K
Thermal conductivity at 25 ^{o}C	113 W/m.k

3.3 Capillary rheometry

The shear viscosity of the PC at temperatures and rates similar to those applied in the injection overmolding of the joints was evaluated using a capillary rheometer SR50 (Instron, USA), with a capillary with diameter of 1 mm and length to diameter (L/D) ratio of 30. The analyses were performed in the shear rate range of 10 s^{-1} to 10000 s^{-1} at three temperatures: 280 °C, 305 °C and 330 °C. The Rabinowitsch correction was employed to determine the shear rates at the inner wall of the capillary according to Equation 3.1 [158]:

$$\dot{\gamma}_w = \dot{\gamma}_A \left(\frac{3+b}{4}\right) \qquad (3.1)$$

Where: $\dot{\gamma}_w$ is the shear rate at the wall, $\dot{\gamma}_A$ is the apparent shear rate at the wall, b = 1/n and n is the power law index.

3.4 AA6061 metal inserts

The AA6061 metal inserts were cut and machined from the rolled sheets to the dimensions established in the 3D image of Figure 3.3. This metal insert is one symmetrical side of a half-lap splice joint. The insert consists of a rectangular part with dimensions of 56.5 mm in length, 24.8 mm in width and 3.2 mm in thickness. Moreover, a recess with 12.7 mm in length, 24.8 mm in width and 1.6 mm in thickness was machined on one end of the insert.

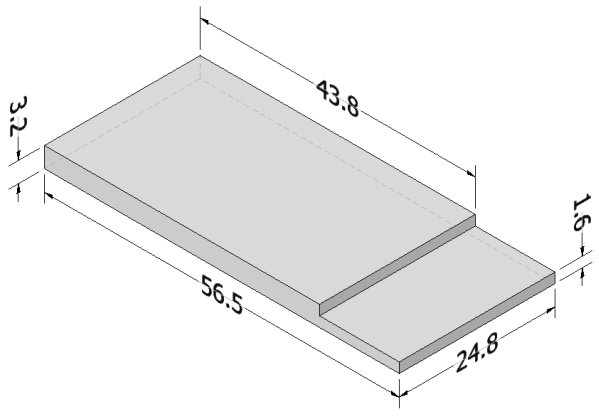

Figure 3.3: Metal insert design. Dimensions are given in mm.

3.5 AA6061 laser texturing

The recess area of the AA6061 insert (Figure 3.3) was texturized by laser to provide adhesion between the polymer and the metal. A pulsed Nd-YAG laser (Trotec SpeedMarker 50, Austria) with 20 watts of average power, wavelength of 1064 nm and laser spot diameter of 45 µm was used. A pattern of grooves spaced (center to center) of 100 µm each and oriented in the direction transverse to the length axis of the AA6061 insert was produced, as shown in Figure 3.4a. Laser scanning conditions were: frequency 20 kHz, speed 500 mm/s and 4 scans. The parameters used were selected from the laser texturing parameters surveyed in the literature review (Section 2.3.1) and preliminary testing with results published in conference proceedings (Section of PUBLICATIONS). The laser was scanned line by line, back and forth, 4 times, resulting in grooves with a width of 45 ± 1 µm and depth of 55 ± 5 µm, as schematically shown in Figure 3.4b. These laser texturing conditions were adjusted with preliminary testing to provide interfacial failure during lap-shear testing of PC/AA6061 joints and thus allow an optimization study of injection overmolding conditions (Section 3.9). Metal inserts were cleaned in an ultrasonic bath with isopropyl alcohol for 10 minutes and temperature controlled at 30 °C followed by cleaning with pressurized air before and after laser texturing. This cleaning procedure was applied to remove grease and debris that does not adhere to the textured metal surface and can act as a weak boundary layer.

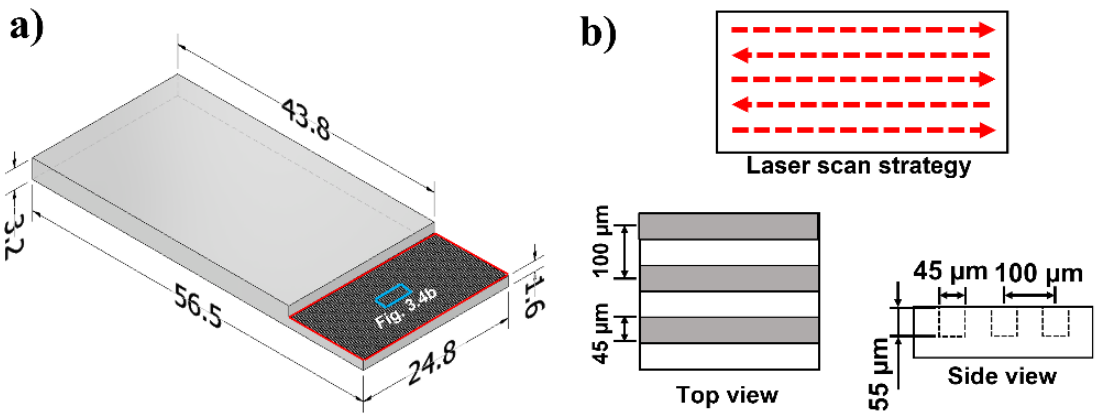

Figure 3.4: Laser texturing design over AA6061 substrates. a) Laser textured AA6061 insert; b) Laser scan strategy and grooves dimensions. Metal inserts dimensions are given in mm.

3.6 Microhardness testing

Hardness of laser texturized and machined (control) AA6061 inserts was measured by Vickers microhardness testing (EmcoTEST, DuraScan G5, Germany). Measurements were carried ou on the cross-section of the sample near the grooves formed by the laser texturization on the surface, as shown in Figure 3.5. The distance of the first indentation to the edges of the specimen was 0.5 mm. Individual indentations were additionally placed as close as possible to the grooves bottom to identify possible process-related thermal changes in the metal. The testing parameters were 0.5 kgf load for 15 seconds with a 40x magnification lens following ASTM E92-17 [159].

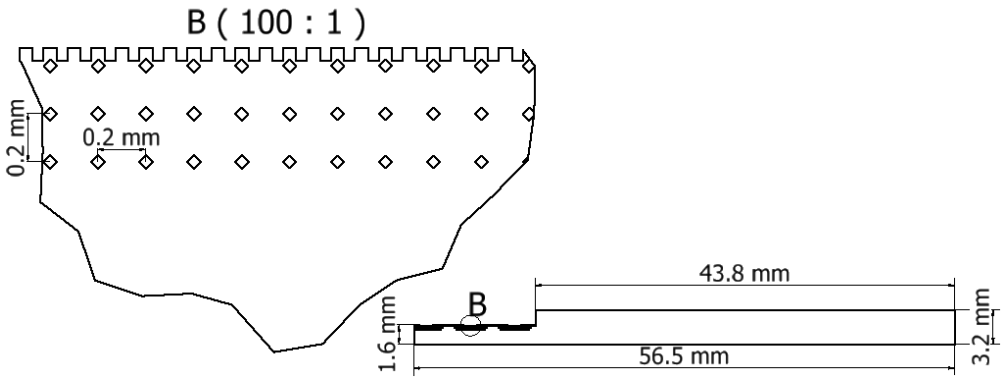

Figure 3.5: Position of indentations formed during cross-sectional microhardness testing in the recess region of AA6061 metal inserts without and with surface laser texturing.

3.7 AlSi10Mg laser powder bed fusion

The printing and the surface structuring of AlSi10Mg inserts were performed by laser powder bed fusion (L-PBF) using a Creator metal 3D-printer (Coherent, Germany) with a 250 W Yb-fiber laser, wavelength (λ) of 1070 nm, under inert gas (Ar) operation atmosphere. The L-PBF equipment is located in the Additive Manufacturing Laboratory of the Institute of Materials Science, Joining and Forming (IMAT) at Graz University of Technology (TU Graz, Austria).

For optimization of L-PBF process, a 2^{k-2} fractional factorial design of experiments with five factors and two levels (i.e. 2^{5-2}) was selected. As the correlation between L-PBF process parameters and relative density has already been described in the literature for this alloy [123] a rather simpler fractional factorial design with a smaller statistical resolution was selected. A detailed statistical analysis was not carried out. The 2^{5-2} fractional factorial design was performed with a center point and four replicates for each condition.

The range of values for the selected parameters was based on previous work with the same AlSi10Mg material and similar equipment, considering the processing window of this aluminum alloy [160,161]. The input parameters were laser power, laser scan speed, laser spot diameter, layer height and hatching distance. The L-PBF-conditions with range of each parameter are shown in Table 3.4. Print bed temperature was kept constant at 55 °C. No post-heat treatment was applied. The printing angle (θ) strategy was of θ = ±45° to the length of the

metal insert (Figure 3.3) and leaning angle (β) – i.e. the angle between the printed part and laser beam of 45° showed in Figure 3.6a. For the optimization step, prismatic specimens with 10 x 10 x 2 mm (length x width x thickness) were printed. The evaluated response was relative density.

In addition, after optimizing the relative density through DoE (refer to APPENDIX A for ANOVA results on the relative density), the influence of the leaning angle (β) on the surface roughness of L-PBF-printed specimens was investigated. For this purpose, identical parts were printed at following leaning angles: β= 0° to 90° with a step of 10°, as illustrated in Figure 3.6b; the resulting surface roughness was then measured by laser confocal microscopy.

Table 3.4: Conditions of the 2^{5-2} fractional factorial design of experiments used to maximize the relative density of AlSi10Mg specimens.

Condition	Laser power [W]	Laser scan speed [mm/s]	Laser spot diameter [µm]	Layer Height [µm]	Hatching distance [µm]
L-PBF - 1	150	750	40	60	120
L-PBF - 2	240	750	40	20	40
L-PBF - 3	150	1500	40	20	120
L-PBF - 4	240	1500	40	60	40
L-PBF - 5	150	750	60	60	40
L-PBF - 6	240	750	60	20	120
L-PBF - 7	150	1500	60	20	40
L-PBF - 8	240	1500	60	60	120
Center point (CP)	195	1125	50	40	80

Analysis of variance (ANOVA) with a confidence level of 95% was used to estimate the influence of studied L-PBF parameters. Minitab software was used to perform the DoE and ANOVA.

For the surface structuring of AlSi10Mg substrates, in addition to the as-built condition, three distinct types of structures with submillimetrical dimensions - namely mushroom, inkpot, and lattice patterns - were printed as presented in Figure 3.7 and Figure 3.8. These submillimetrical structures were added to provide mechanical anchoring of the consolidated polymer on the metal surface of the joints. Two L-PBF conditions with the highest relative density were selected out of the DoE runs: L-PBF-2, L-PBF-6. These two conditions with distinct energy

inputs were used to evaluate the influence of laser spot diameter and hatch distance on the roughness and geometry of submillimetrical structures. The DoE run leading to a more stable and reproducible printing of the futures was selected for further mechanical characterization.

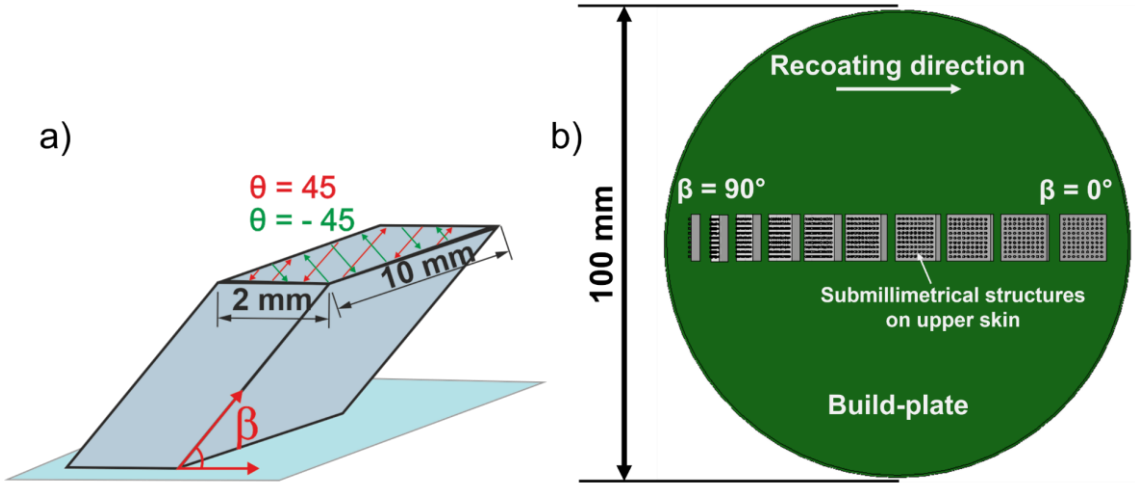

Figure 3.6: Schematic representation of printing strategy (θ) and leaning (β) angles: a) the geometric dimensioning and the printing angle of θ = ± 45°; b) Top view of the arrangement showing used leaning angles (β =0° to 90°, 10° pitch).

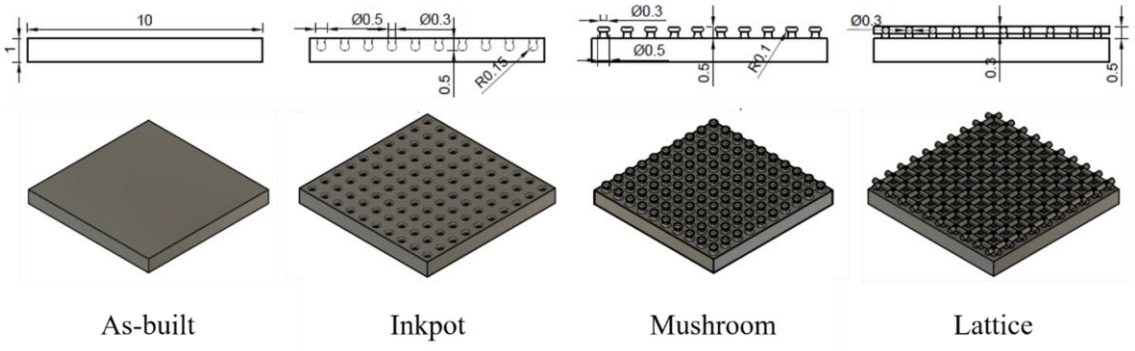

Figure 3.7: Schematic drawings of the submilimetrical structures on the surface of the AlSi10Mg substrates. Dimensions in millimeters.

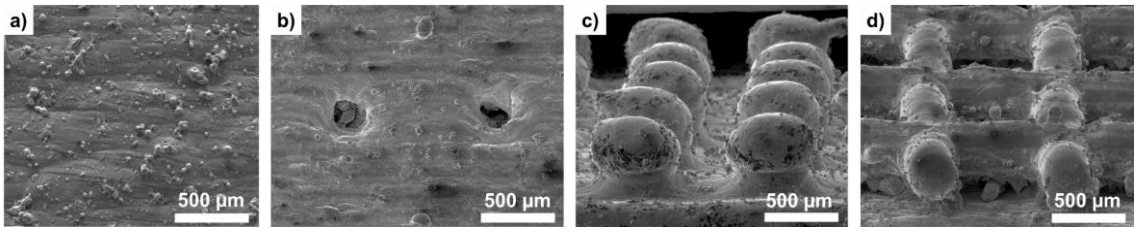

Figure 3.8: Examples of the submilimetrical structures patterns and as-built printed by L-PBF on the surface of AlSi10Mg substrates: a) as-built; b) mushroom; c) inkpot, d) lattice. Printing condition L-PBF-6, Table 3.4.

3.8 AlSi10Mg relative density measurements

The relative density of the AlSi10Mg printed parts was selected as the response to the design of experiments. The property was calculated by dividing the experimental density by the theoretical density of this aluminum alloy (2.63 g/cm^3) [6]. The experimental density was determined by Archimedes principle using a RADWAG WLC X2 precision balance (RADWAG, Poland) and ethyl alcohol for submerging the calibrated reference specimen and the L-PBF parts.

3.9 Injection overmolding

PC/AA6061 joints with half-lap splice configuration (Figure 3.9) were prepared using an Arburg Allrounder 270V injection molding machine (Arburg, Germany) operated in semi-automatic mode, with the metal inserts being manually positioned into the mold cavity before each molding cycle. Figure 3.10 shows a photograph of an injection overmolded PC/AA6061 hybrid joint specimen containing the sprue, runner and gate.

Design of experiments of the type 2^3-full factorial with one center point and five replicates for each condition was used for the injection overmolding understanding and optimization of the injection overmolding of AA6061 laser-structured inserts. The injection overmolding parameter values were set based on the PC processing window to produce integrate joints free of volumetric or surface defects. The DoE factors, namely, barrel temperature, injection speed and holding pressure were varied by 2 levels each, as shown in Table 3.5. Other injection overmolding conditions were kept constant as following: holding time of

6 s, mold temperature of 110 °C (taking as reference the heat distortion temperature (HDT) of 132 °C (ASTM D648 [162]: 1.82 MPa) and the glass transition temperature (T_g) of 145 °C of the PC, and cooling time of 25 s. The AA6061 substrates were preheated to 110 ºC in an electrical oven for 2 hours, manually positioned inside the mold cavity to support the heating process of the substrate inside the mold, shortening heating of the substrate inside the mold prior to polymer injection. A waiting time of 60 seconds was applied before each molding cycle to ensure temperature equalization of the metal insert with the mold cavity.

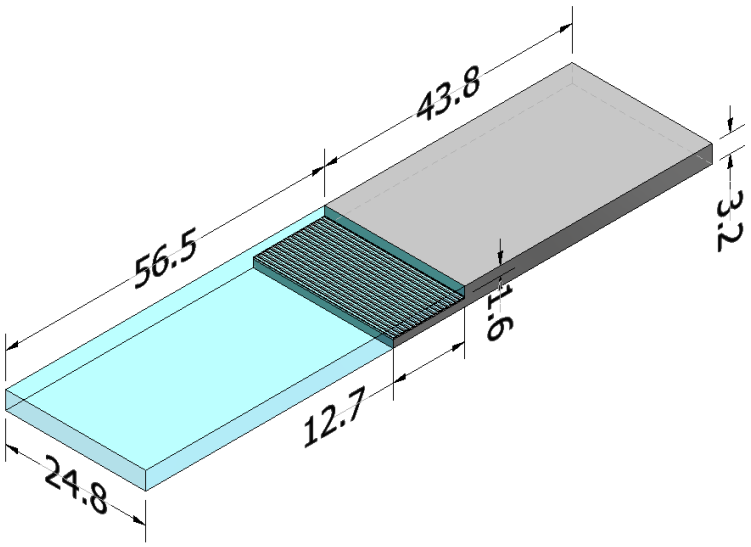

Figure 3.9: Geometry and dimensions of the injection overmolded PC/AA6061 hybrid joint specimens. AA6061 in light gray. Dimensions in millimeters (mm).

The investigate response to the design of the experiment was the joint ultimate lap-shear force (ULSF). ANOVA with a confidence level of 95% was used to estimate the influence of each injection overmolding parameter and its interactions. Minitab software (Pennsylvania State University, USA) was used for the statistical evaluation.

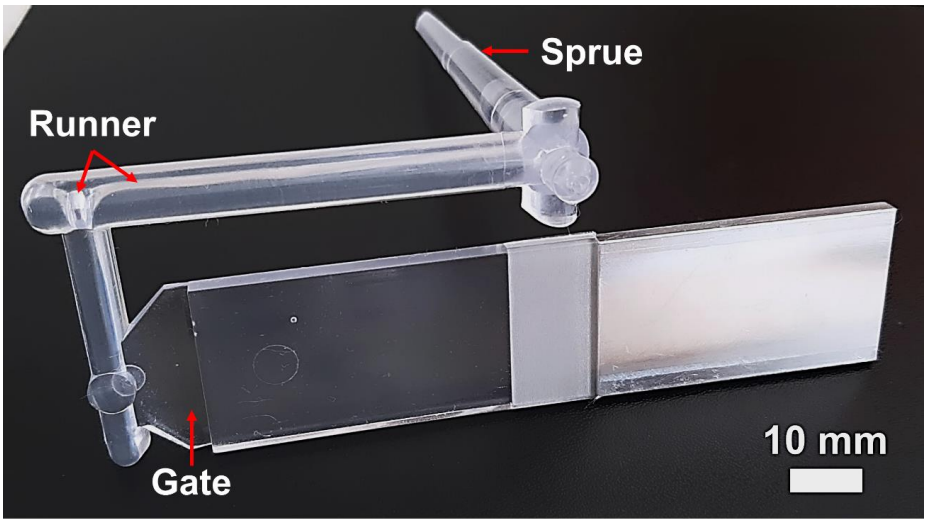

Figure 3.10: Photograph of an injection overmolded PC/AA6061 joint specimen containing the sprue, runner and gate.

Table 3.5: Conditions of the full factorial design of experiments (2^3) used to produce PC/AA6061-laser-treated hybrid joints via injection overmolding direct joining.

Condition	Barrel temperature [°C]	Injection speed [cm^3/s]	Holding pressure [bar]
C1	280	40	600
C2	330	40	600
C3	280	80	600
C4	330	80	1000
C5	280	40	1000
C6	330	40	1000
C7	280	80	1000
C8	330	80	600
CP	305	60	800

The PC/AlSi10Mg hybrid structures were prepared on the same injection overmolding machine in the form of a half-lap splice joint, whose geometry and dimensions are detailed in Figure 3.11. An area (6.35 × 12.4 mm^2) of ¼ the surface area of the metal insert recess was structured with submilimetrical patterns, as schematically shown in Figure 3.11. A smaller structured area (in comparison to the AA6061 inserts – Figure 3.9) was necessary to ensure

cohesive fracture at the polymer-metal interface. For the preparation of these joints, the injection overmolding conditions optimized according to the study for the AA6061 inserts were employed (i.e., the condition C4 in Table 3.5).

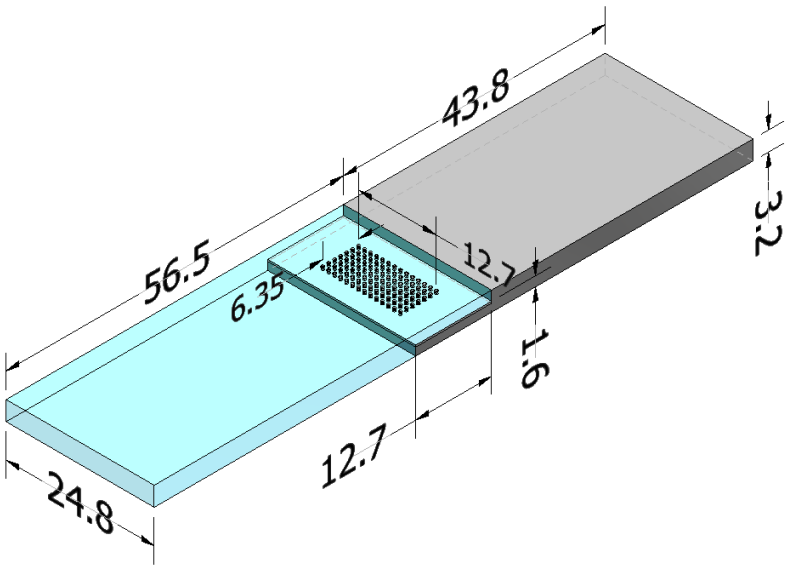

Figure 3.11: Geometry and dimensions of the injection overmolded PC/AlSi10Mg hybrid joint specimens. AlSi10Mg in light gray. Dimensions in millimeters (mm).

Moreover, PC tensile specimens with dimensions according to ASTM D638 - Type I [163] were injection molded (APPENDIX B) using the optimized injection overmolding parameters (i.e., condition C4 in Table 3.5).

3.10 Lap-shear testing

The joining strength of the PC/AA6061 and PC/AlSi10Mg joints were evaluated by lap-shear testing based on ASTM 1002 [164] using an Instron 5569 universal testing machine (Instron, USA), with a distance between grips of 60 mm and a crosshead speed of 1.27 mm/min (0.05 inch/min) and a load cell of 50 kN. Five replicates were tested for each condition.

The tensile properties of injection-molded polycarbonate specimens, both unaged and aged by immersion in water at 80 °C for 30 days, were determined based on ASTM D638 [163] using the same universal testing machine with a crosshead speed of 5 mm/min. Young modulus was determined in the deformation range of 0% - 1% using a strain gauge with 50 mm aperture. Ten

replicates were tested. Mechanical tests were performed at room temperature of 23 °C ± 1 °C and relative humidity of 50% ± 5%.

3.11 Confocal laser scanning microscopy

A confocal laser microscopy LEXT OLS 4100 (Olympus, Japan) with wavelength of 405 nm was used to examine the surfaces of the AlSi10Mg printed samples and laser-textured AA6061 samples. The surface roughness, area and volume calculations were performed using the OLS4100 software (Olympus, Japan).

Optical microscopy images were captured with the confocal laser microscope from the cross-section of the PC/AA6061 and PC/AlSI10Mg joints to observe the fillinf of the polymer into the features formed on the metal surface.

3.12 Scanning electron microscopy (SEM)

After shear testing, the fracture surfaces were examined using a FEI Inspect S50 scanning electron microscope (FEI, USA) equipped with secondary and back-scattered electron detectors operated at an accelerating voltage of 15 kV, work distance of 10 mm and vacuum atmosphere. Energy dispersive X-ray spectroscopy (EDS) was used to perform chemical composition microanalysis on the fracture surfaces of the joints. The analyzed samples were placed on carbon tapes and then covered with gold and palladium before analyzing.

3.13 Digital image correlation (DIC)

Digital Image Correlation (DIC) was applied along with lap-shear testing to PC/AA6061 and PC/AlSi10Mg injection overmolded hybrid specimens produced with the optimized condition (condition C4, Table 3.5).

Prior to DIC testing, hybrid specimens were sprayed with a thin layer of white paint on the sample surface in the region of interest (overlap region) to establish a ground coating. The area was then lightly sprayed with black paint to deposit black paint dots and provide contrast on the surface of interest.

During lap-shear testing, the DIC optical system method can precisely track the displacement of the joint through these dots. For this two CCD-cameras were utilized for image acquisition during lap-shear testing monitored by DIC. One camera was placed to record the joint front, where the polymer is on the metal; this camera will be identified as FC (frontal camera). The second camera was placed to record the specimen side; this camera will be designated as LC (lateral camera). Figure 3.12a depicts the schematics of the specimen areas recorded during mechanical testing. Figure 3.12b shows an overview photo of the the DIC system setup used. Universal joints were added to the testing jig on both sides of the mechanical gripping jaws to provide freedom of movement during shear testing. The details of technical specifications of the image acquisition system, DIC setup parameters and software can be found in APPENDIX C.

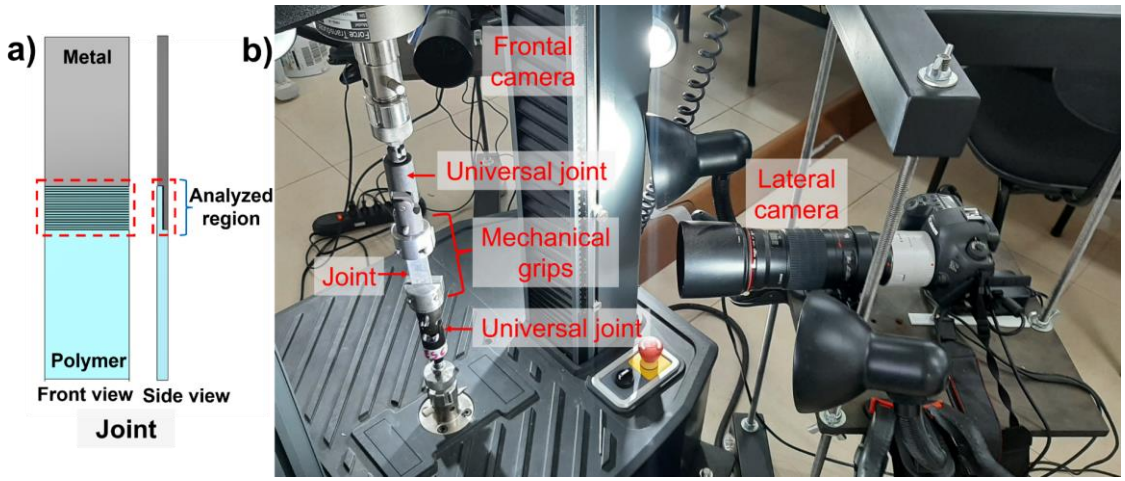

Figure 3.12: Set-up of the position of the cameras concerning the joint subjected to shear strength testing.

For the lap-shear testing with DIC analysis, an MTS E44 universal testing machine (MTS Systems Corporation, USA) equipped with a load cell of 50 kN) was used with 60 mm distance between grips, a crosshead speed of 0.5 mm/s, at room temperature. Reducing the crosshead speed relative to earlier lap-shear tests was required to maximize the data displacement acquisition to precisely measure the joint displacement. A loading and unloading protocol was applied to the lap-shear testing monitored by DIC, as shown in Figure 3.13. Correli 3.0 [165]

framework was used to analyze the captured images and identify the displacement fields on the joint surface.

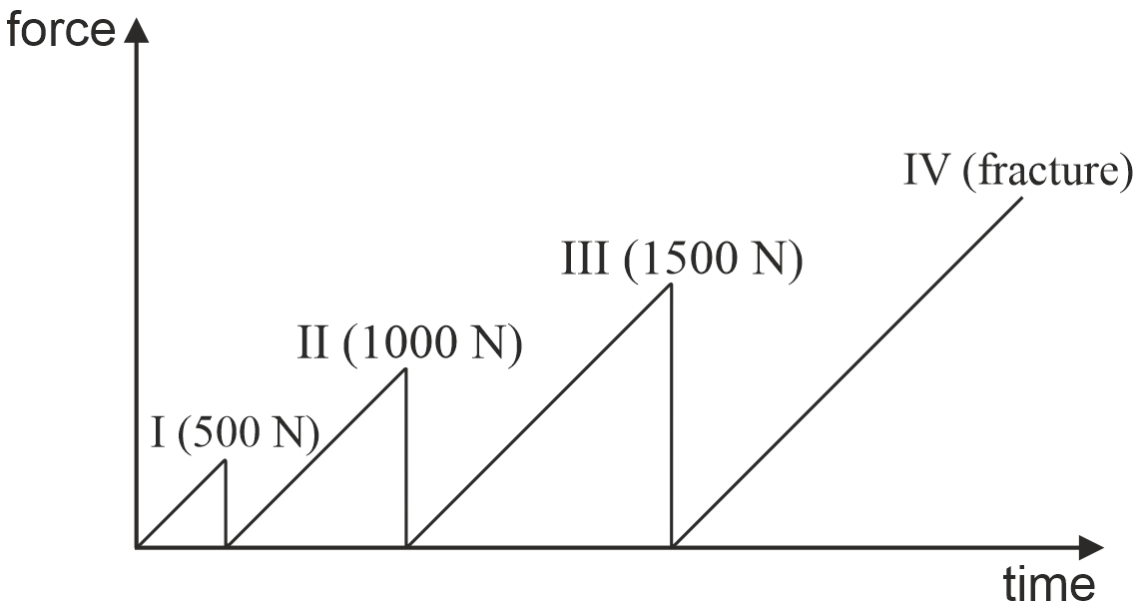

Figure 3.13: Loading protocol applied in the lap-shear tensile testing monitored by digital image correlation (DIC). Recurring loading-unloading cycles of I: 0 - 500 N; II: 0 - 1000 N; III: 0 - 1500 N; IV: 0 - fracture. Crosshead speed of 0.5 mm/min.

3.14 Fatigue testing

PC/AA6061 and PC/AlSi10Mg hybrid joints produced with the DoE optimized injection overmolding condition (i.e., condition C4 in Table 3.5) were subjected to dynamic fatigue testing to estimate the mechanical durability of these joints. An MTS Bionix® universal testing machine (MTS, USA) was used, operated under the following conditions: sinusoidal tensile mode (R = 0.1); frequency 5 Hz; 4 load levels: 30%, 40%, 50%, and 70% of the ULSF recorded under lap-shear loading (Section 3.10). All fatigue tests were performed at a room temperature of 23 °C ± 1 °C and a relative humidity of 50% ± 5%. Three replicates were tested for each condition. The measurement of the temperature during fatigue test was manually performed with a laser thermometer on the surface of the overlap area. No relevant variation in temperature was detected (25 °C ± 3 °C). The exponential model is one of the most used technique for evaluating the fatigue life of overlap joints [166–168]. ASTM standard E739 [169] describes in

detail the approach for fitting fatigue data using the exponential model. Using the aforementioned standard, 3.2 is used to establish the form of the S–N curve:

$$\log(N) = a + bF \qquad (3.2)$$

Where N is the fatigue life data, F is the maximum value of cyclic force and a and b are the model parameters determined using a linear regression model.

3.15 Hygrothermal aging

PC/AA6061 hybrid joints produced under optimized injection overmolding condition C4 (Table 3.5) were subjected to accelerated hygrothermal aging with a procedure adapted from ASTM D1151. The joints were immersed in a deionized water bath at 80 ^{o}C for different periods; 1 day, 7 days, and 30 days, and then subjected to lap-shear testing. The weight of the joints was measured before and after aging to evaluate the water intake. Five replicates were tested for each condition following the testing procedure described in (Section 3.10).

3.16 Differential scanning calorimetry (DSC)

PC samples extracted from half of the cross section at the midpoint of the length near the overlap region of aged hybrid joints and unaged (control) PC specimens were subjected to differential scanning calorimetry (DSC) using a Q2000 equipment (TA Instruments, USA) for determining the glass transition temperature (T_g) of the polymer. Samples weighing 8.5 ± 0.2 mg were placed in aluminum crucibles and subjected to the following thermal cycle: (1) heating from 23 °C to 330 °C at 10 °C/min; (2) cooling at 10 °C/min to room temperature, under nitrogen atmosphere (50 mL/min). These analyses were performed in duplicate.

4 RESULTS AND DISCUSSION

4.1 PC/AA6061 hybrid joints

As described in Section 3.1, this first part consisted of joint design, laser texturing of the metal insert and optimization of the injection overmolding process parameters through lap-shear testing joint response. Moreover, fracture analysis was performed through scanning electron microscopy (SEM) and digital image correlation (DIC) analyses. Furthermore, the durability of PC/AA6061 joints produced with optimized injection processing parameters was investigated through fatigue testing and hygrothermal aging.

4.1.1 Surface analysis and microhardness testing of laser textured AA6061 inserts

Figure 4.1a-b shows images and height profiles obtained by laser scanning confocal microscopy of the machined and laser textured surfaces of the overlap region of AA6061 inserts. The machined surface showed surface irregularities with an average depth of 0.8 ± 0.2 µm and roughness R_a and R_z values of 0.1 ± 0.01 µm and 0.4 ± 0.3 µm, respectively. The laser textured surface showed grooves with depth of 55 ± 5 µm and roughness R_a and R_z values of 8 ± 0.5 µm and 27 ± 1 µm, respectively. Moreover, resolidified material can be observed on the laser-textured surface (Figure 4.1b). During the laser scanning, the heated material is expelled from the radiated spot and displaced onto the surface and/or in the grooves next to it, thereby solidifying in place [170]. Resolidified material, also known as slag, can aid in the micro-anchoring of the polymer on the metal surface when properly attached to the surface [14]. The center-to-center distance of the radiated lines remained constant at 100 µm, and the average width between peaks was 47 µm ± 2 µm, close to the diameter of the laser beam at the focus as well as the dimensions depicted in Figure 3.4.

The areas and the feature volumes of the analyzed surfaces (640 × 640 μm^2) were determined using the laser confocal microscope software and extrapolated to the total area of the insert recess (12.7 × 24.8 mm^2). The surface areas for the machined and laser-textured samples were 315 mm^2 and 715 mm^2,

respectively. Analogously, the feature volumes for the surface of the machined and laser-textured samples were 0.22 mm^3 and 10.6 mm^3, respectively. Therefore, laser texturing produces a huge increase (approx. 4,800%) in the micrometric volume available for filling of the polymer into the metal surface grooves. Nonetheless, laser texturing and groove design parameters on the AA6061 inserts were chosen to induce fracture at the PC/AA6061 hybrid joint interface in order to explore the effects of injection overmolding conditions on the joining strength, as will be shown in the next section.

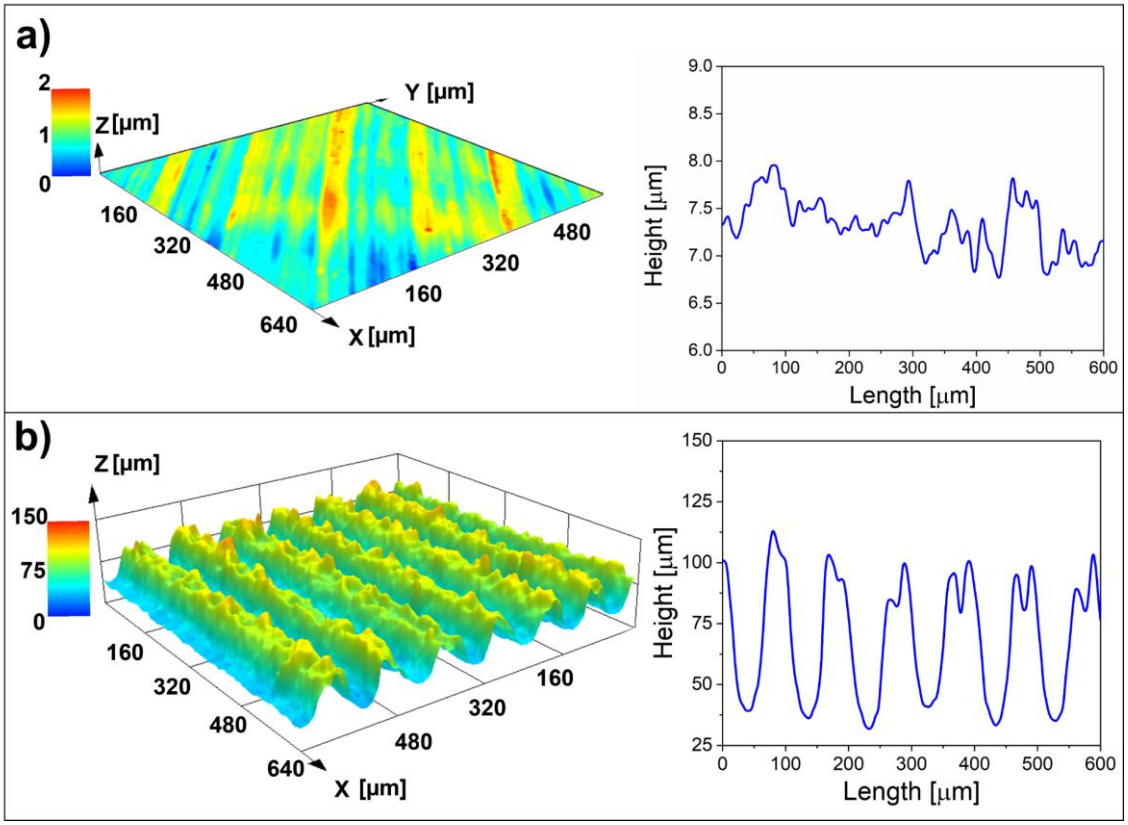

Figure 4.1: Laser scanning confocal image and height profile of the machined (a) and laser textured (b) AA6061 surfaces.

The local mechanical properties of machined and laser-textured AA6061 substrates were investigated using Vickers microhardness testing (Section 3.6). This investigation was conducted because laser texturing may alter the metal microstructure due to the significantly high energy input to the substrate. Figure 4.2 depicts the microhardness results for the two substrates. After laser texturing,

no significant difference in Vickers hardness was detected; the average microhardness was 109 ± 4 HV and 112 ± 4 HV for the machined and laser-textured substrates, respectively. However, the study of the process-related microstructural changes was out of the scope of this work. Based on the microhardness measurements, one may infer that laser texturing did not significantly alter the microstructure of the metal surface. This is probably because of the combination of the aluminum high surface reflectivity and poor absorption of electromagnetic radiation [171], along with the applied low laser power (20 W on average), the metal surface microstructure was not compromised. Nevertheless, this should be investigated in greater depth using microscopy techniques.

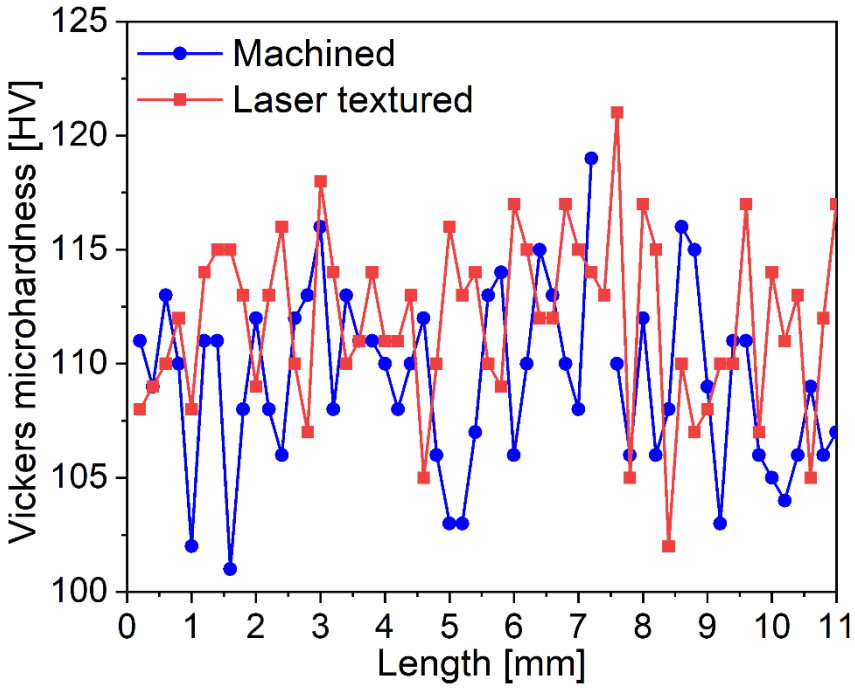

Figure 4.2: Vicker microhardness line measurements at the cross section (Figure 3.5) of the machined and laser-textured AA6061-T6 substrates.

Therefore, it is possible to conclude that laser texturing is not strongly changing the original AA6061-T6 base materials properties.

4.1.2 Effects of injection overmolding conditions on the interfacial structure and joining strength of PC/AA6061 joints

Figure 4.3 shows the mean values and respective standard deviations for the ultimate lap-shear forces (ULSF) of the PC/AA6061 joints injection overmolded at different conditions (Table 3.5). ULSF values ranged from 191 ± 58 N to 2149 ± 127 N. Typical force vs. displacement curves are shown in APPENDIX D. The highest ULSF value of hybrid lap-shear specimens corresponds to about 94% of the force required for the ductile failure of PC component (2285 N, value obtained in the tensile strength testing presented in Section 4.1.5). All hybrid specimens presented shear fracture at the interface – i.e., delamination (Section 4.1.3, Figure 4.10) – (this will be addressed in the next section). It is worth mentioning that interfacial failure was intentionally provoked (by adjusting the laser texturing conditions of the metal) so that the effects of the injection overmolding conditions on the bonding strength could be evaluated at the interface between metal and polymer. In other words, net-tension failure (PC part failure) was intentionally prevented. Metal laser texturing conditions can be adjusted to cause the ductile failure of the polymer component and thus superior joining strength (this will be addressed at the end of this section).

Using the Pareto chart (Figure 4.4) with a significance level (α) of 0.05 it was showed that the factors barrel temperature, injection speed, and holding pressure exert significant influences on the joining strength of the PC/AA6061 joints, with the barrel temperature being the most significant factor, followed by the holding pressure, and then the injection speed. Moreover, the Pareto chart showed that interactions between these components are not statistically significant for the examined response.

Analysis of variance (ANOVA) with a 95% confidence level was used to estimate the influence of the factors on the analyzed response. The ANOVA for the ultimate lap-shear force of PC/AA6061 joints is summarized in Table 4.1. The F-values for the main effects and their interactions are calculated by dividing the mean square of the effect of interest by the mean square of the error. The barrel temperature showed the highest effect on the statistical model with an F-ratio of 60.84, followed by the holding pressure with an F-value of 45.47

and injection speed with a minor significant value of 4.59. Furthermore, the p-value indicates if the parameter or interaction is significant to the model when α is lower than 0.05.

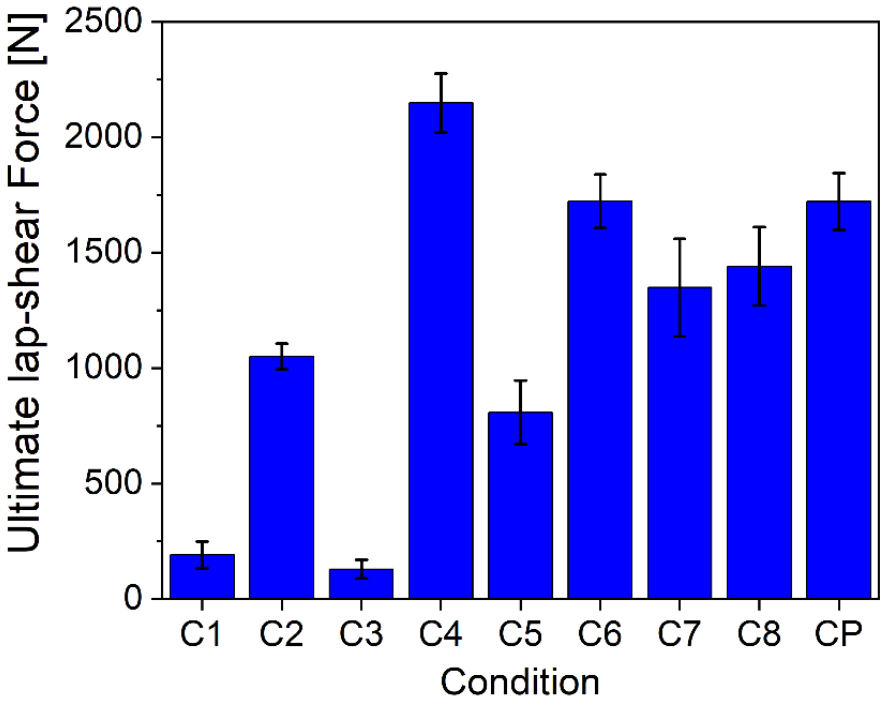

Figure 4.3: Ultimate lap-shear force of PC/AA6061 joints as a function of injection overmolding conditions (see Table 3.4).

The "mean of means" plot for ULSF in Figure 4.5 which compares the arithmetic mean of the response ULSF for minimum (-1) and maximum (+1) levels of the factors with the total arithmetic mean of all samples, indicates that the three factors analyzed (barrel temperature, injection speed and holding pressure) have a positive effect on the joining strength of the PC/AA6061 joints. The statistical model produced an adjusted R^2 equal to 81%. The regression model equation is given in Equation 4.1 [172], where the first term is the total variation in the response y, the second is the variation in mean response and the last term is the residual value.

$$\sum(y_i - \bar{y})^2 = \sum(\hat{y}_i - \bar{y})^2 + \sum(y_i - \hat{y}_i)^2 \qquad (4.1)$$

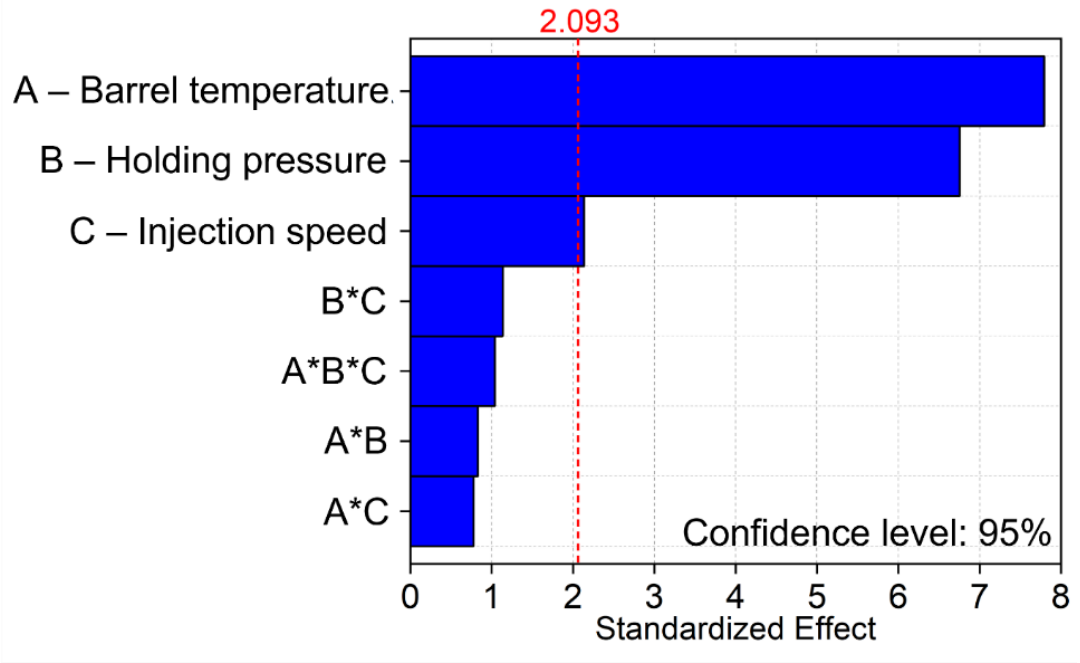

Figure 4.4: Pareto chart of standardized effects for the ultimate lap-shear force of PC/AA6061 hybrid joints.

Table 4.1: Analysis of variance (ANOVA) of the ultimate lap-shear force of PC/AA6061 hybrid joints.

Source	DF	Adj SS	Adj MS	F-Value	p-Value
Model	8	10952755	1369094	56.61	0.001
Linear					
Barrel temperature	1	5183600	5183600	214.33	0.001
Injection speed	1	391408	391408	16.18	0.001
Holding pressure	1	3874731	3874731	160.21	0.001
2-Way Interactions					
Barrel temperature*Injection speed	1	52311	52311	2.16	0.159
Barrel temperature*Holding pressure	1	60697	60697	2.51	0.131
Injection speed*Holding pressure	1	112039	112039	4.63	0.055
3-Way Interactions					
Barrel temperature*Injection speed*Holding pressure	1	94368	94368	3.90	0.064
Error	18	435327	24185		
Total	26	11388082			

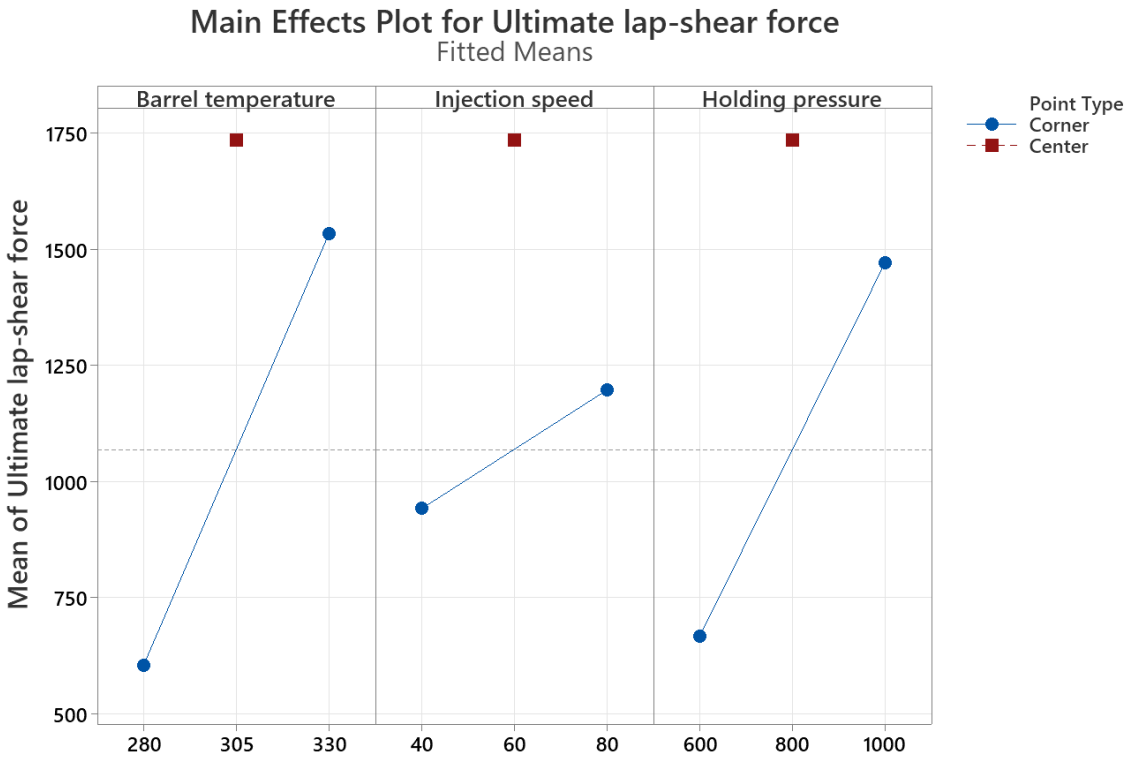

Figure 4.5: Main effect plots illustrating the influence of the injection overmolding parameters (barrel temperature, injection speed, and holding pressure) on the ultimate lap-shear force PC/AA6061 joints.

Increasing the factors that exert a positive influence on this response, i.e., barrel temperature, injection speed, and holding pressure, resulted in greater fillinf of the PC into the grooves of the AA6061 surface, as shown for the polymer fracture surfaces and cross-sections (Figure 4.6a-c) of PC/AA6061 joints injection overmolded in the conditions C1, CP and C4. The joint which presented the lowest ULSF value (condition C1) exhibited a relatively little filling of the polymer into the metal grooves of 25 µm ± 1 µm, which corresponds to approximatively 50% of the average groove depth (55 µm ± 5 µm). Condition CP with intermediate ULSF value showed higher polymer filling of 41 µm ± 3 µm (75% of the average groove depth). Condition C4 (Figure 4.6c) with the highest ULSF value showed polymer filling of 55 µm ± 5 µm, filling completely the grooves formed on the metal surface.

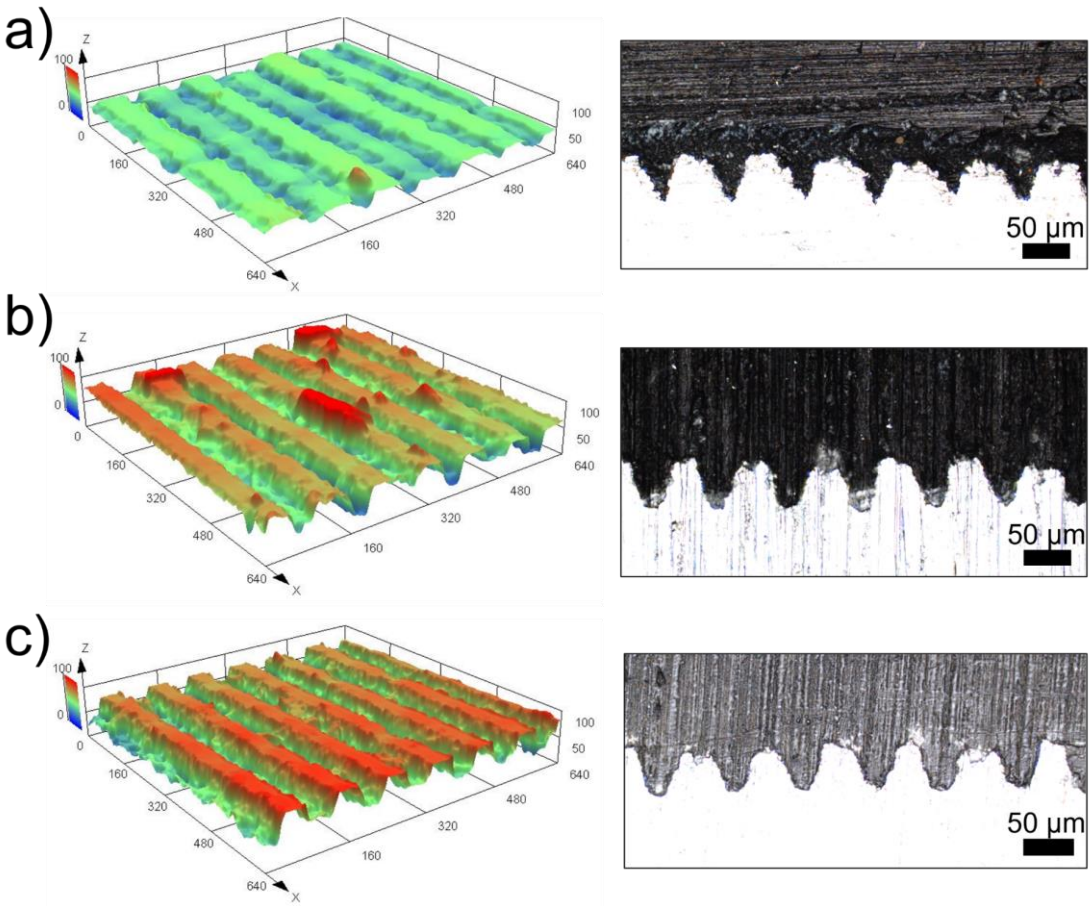

Figure 4.6: On the left-hand side laser confocal microscopy images of polymer fracture surfaces and on the right-hand side color images obtained in the laser confocal microscope of the cross-section of PC/AA6061 joints injection overmolded under the following conditions: a) C1 (minimum levels); b) C9 (center point - CP); and c) C4 (maximum levels). Metal and polymer parts appear as light and dark, respectively.

In direct-adhesion injection overmolding of PMHs, the degree of polymer filling into metal grooves is dependent on the rheology of the polymer. Based on this, the PC was subjected to capillary rheometry to estimate viscosity under conditions similar to those produced in the injection overmolding of PC/AA6061 joints.

The viscosity curves for the PC at 280 °C, 300 °C and 330 °C are shown in Figure 4.7. In Figure 4.7, the range of shear rate to which the polymer is exposed in the polymer-metal joining zone during injection overmolding is depicted as a light gray area. For this estimation, Equation 4.2 was used, assuming that the PC flow in the overlap area (Figure 3.4, W = 24.8 mm and H = 1.6 mm) is similar to a pressure-driven isothermal flow of a power law fluid in between parallel plates, where Q is the flow rate (injection speed), W is the width and H is the thickness of the channel [173]. For simplification purposes, the grooves structures were not considered.

$$\dot{\gamma}_w = \left(\frac{2n+1}{n}\right)\frac{2Q}{W.H^2} \qquad (4.2)$$

As expected, the melt viscosity of PC decreases with temperature and shear rate applied. The increase in the temperature increases the mobility of polymer chains and the higher free volume between polymer chains generates less friction, decreasing viscosity. The viscosity lowers as shear rates increase because, at high shear rates, the polymer chains tend to align in the direction of flow, reducing the degree of entanglement and flow resistance [173,174]. By examining the viscosity curve and the shear rate estimated for the joining region, one can estimate that the viscosity of the PC ranges from 215 Pa.s to 50 Pa.s, depending on the injection molding conditions.

When the molten polymer hits the surface of the metal insert at a lower temperature (e.g. condition C1 with a barrel temperature of 280 °C), a thin solidified skin layer is formed; the magnitude of the thickness, depending on the injection overmolding conditions, will restrict the filling of the polymer into the grooves of the metal as seen in Figure 4.6a. Thus, as shown above, increasing barrel temperature decreases the viscosity of the polymer during the cavity filling, reducing the thickness of the frozen layer and facilitating the filling of the polymer into the metal grooves. Increasing injection speed results in a higher shear rate at the polymer-metal interface and a shorter filling time, which reduces the viscosity of the polymer melt and the thickness of the frozen layer, improving the filling of polymer into metal grooves. Increased holding pressure leads to

increased deformation of the frozen layer during the packing process, allowing for higher polymer filling into the metal grooves. Therefore, the maximum values of these parameters (barrel temperature, injection speed and holding pressure) assist in infiltrating the polymer into the grooves on the metal surface, as shown in Figure 4.6c for condition C4 (Table 3.5). Moreover, holding pressure acts to compensate for the thermal contraction of the polymer during the solidification in the mold cavity, helping to keep the polymer infiltrated into the metal grooves. In APPENDIX E, a pvT curve of a PC is shown in which it is possible to have an estimate of the polymer shrinkage after pressure and temperature relief in injection molding. As PC is an amorphous polymer, its volumetric shrinkage after injection molding is considerably low, allowing the metal grooves to remain completely filled with PC after joint cooling.

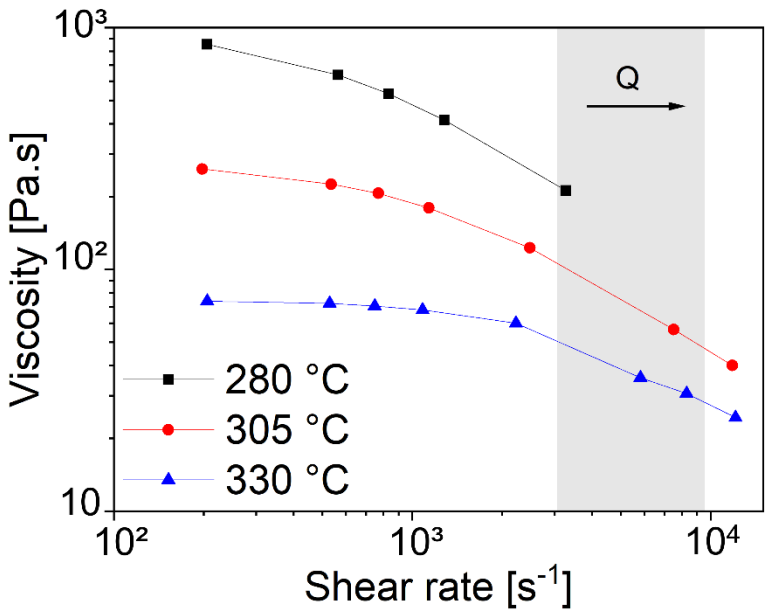

Figure 4.7: Capillary rheometer viscosity curves of PC (LEXAN 103) at temperatures similar to that employed in the injection overmolding of the joints (see Table 3.4). Viscosity data at 280 °C were measured at shear rates below 2 $\times$ 10^3 s^{-1} since the upper limit of the rheometer load cell was reached. The range of shear rate to which the polymer is exposed in the polymer-metal joining zone during injection overmolding is depicted as a light gray area.

Effects of injection overmolding conditions on the mechanical strength of injection-molded polymer-metal overmolded joints have been explored in the literature with other combinations of polymers and metals and with various types of metal surface preparation. Zhao *et al*. [84] examined the effects of barrel temperature and packing and holding pressures on joints of PBT-30GF composite and laser-textured AA5052 insert. The authors noticed an improvement in the mechanical strength of the joints with increasing packing and holding pressure. At the same time, barrel temperature only positively affected joints molded with low packing pressure. The mechanical strength of these joints correlated well with the degree of PBT-30GF composite filling into the AA5052 surface grooves. Lucchetta *et al*. [53] observed a positive effect of injection speed on the mechanical interfacial strength of PPS-40GF composite joints with AA6082 that had been treated with abrasive blasting. Overall, injection overmolding studies [50,53,56,83,84,90] have shown good correlations between the mechanical strength of the joints and the degree of polymer filling into the metal surface microcavities. According to published studies [55,62,78,134,175,176], the temperature of the metal insert, which is controlled by insert preheating and mold temperature, has a favorable impact on the interfacial mechanical strength of polymer-metal joints produced by injection overmolding. It is because the temperature of the metal insert increases and the thickness of the solidified polymer layer decreases, allowing for easier filling of the polymer into the metal microcavities, providing a larger contact area between the polymer and metal. Based on these studies, the AA6061 inserts were preheated and the mold temperature was adjusted to 110 °C using the heat distortion temperature (HDT) of 132 °C (ASTM D638: 1.82 MPa) and the glass transition temperature (T_g) of the PC as a reference guide. This approach allowed the PC to infiltrate the grooves of the AA6061 insert (Figure 4.6) while simultaneously allowing the PC/AA6061 joints to be extracted from the injection mold without affecting their dimensional integrity.

Furthermore, the response (ULSF) was maximized for "higher is better" and the following parameters resulted from this optimization: barrel temperature 330 °C, injection speed 80 cm^3/s and holding pressure 1000 bar. Based on this,

condition 4 (Table 3.4) has the same parameters as the optimization response and was selected as optimized injection overmolding parameters to produce PC/AA6061 joints for digital image correlation (DIC), fatigue testing and hygrothermal aging analysis.

The joining strength of the PC/AA6061 joints, as measured by the ultimate lap-shear force (ULSF), was shown to be linearly dependent on the filling depth of the PC into the grooves of the AA6061 surface, as shown in Figure 4.8. Increasing the filling depth of the PC into the grooves of the AA6061 increases the interference volume between the polymer and metal components, resulting in PC/AA6061 joints that are mechanically stronger. This behavior is consistent with the findings of previously published papers [80–82,85,90,136] on injection overmolded joints using different polymer-metal combinations.

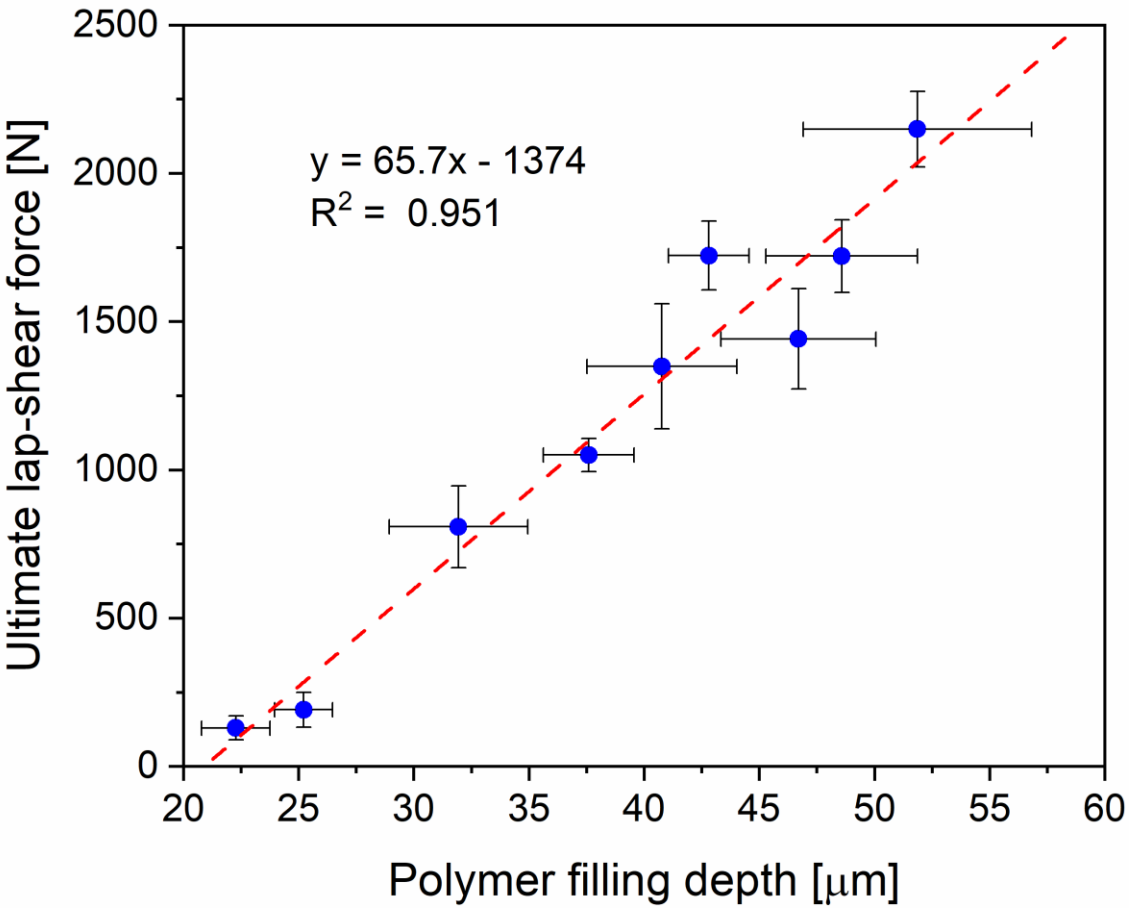

Figure 4.8: Ultimate lap-shear force of PC/AA6061 joints injection overmolded under different conditions as a function of the filling depth of the PC into the AA6061 grooves.

It is worth mentioning that the polymer-metal bonded area is not microscopely uniform in the overlap zone of PC/AA6061 joints. As can be seen in the top-view photograph of the PC/AA6061 hybrid joint (Figure 4.9) produced with injection overmolding parameters set on the center point (CP), there is a darker region in the center of the overlap zone indicating that the polymer is effectively bonded (attached) to the metal part. It seems that the polymer has detached from the metal surface at the outskirt regions of the overlap area. This is most probably due to inhomogeneous volumetric shrinkage after cooling, which produces residual stresses on the polymeric side [177–179]; these will induce delamination. In general, samples with lower ULSF values showed slightly smaller bonding areas.

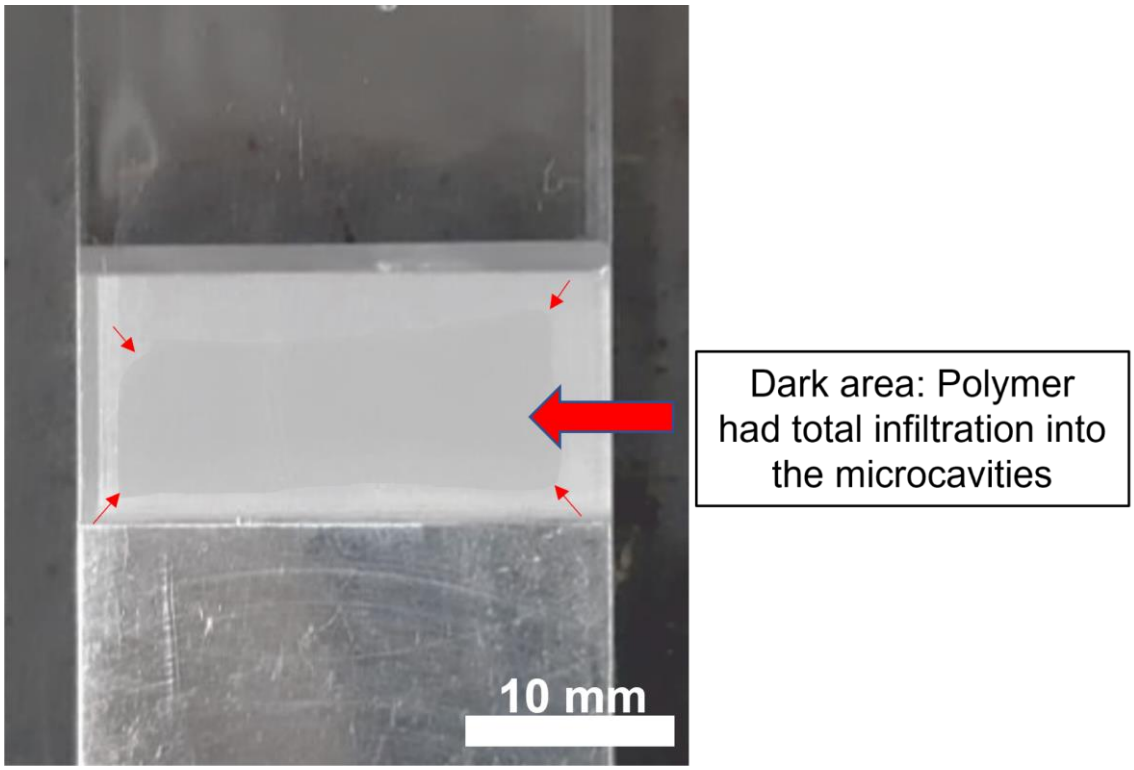

Figure 4.9: Top view of the overlap zone of a PC/AA6061 joint injection overmolded at condition CP (center point). The red arrows indicate the central region where polymer is bonded (attached) to the metal surface. At the surrounds polymer has delaminated from the metal surface after joint cooling owing to warpage (release of thermal-induced residual stresses).

However, the precise determination of the real bonded area is very complicated without destructing the specimens. Therefore, a common practice in joining and additive manufacturing of hybrid structures [1], the nominal overlap area is used to calculate joint strength. Considering that a NDT approach, such as X-ray microtomography, was out of the scope of this study, the overlap area was taken as being equal to the nominal area of the metal insert recess that had been laser textured, that is, 12.7 x 24.8 mm^2 (Figure 3.4). As a result, the PC/AA6061 joint injection overmolded in the optimized condition, which obtained complete PC filling in the grooves of the metal (Figure 4.6c) and ULSF of 2149 ± 127 N (Figure 4.3), has a nominal ultimate lap shear strength (ULSS) of 6.8 ± 0.4 MPa.

It is worth remembering that in order to make the study of the effects of injection overmolding conditions on the joining strength possible, laser texturing conditions applied on the metal surface were adjusted to provide interfacial shear failure during lap-shear testing of PC/AA6061 joints. Stronger joints could have been obtained by increasing the depth of the grooves produced on the metal surface.

To try to confirm this assumption, a set of hybrid joints were produced under optimized injection overmolding condition (C4) using laser textured AA6061 inserts (produced with frequency 20 kHz, speed 500 mm/s and 8 scans) with deeper grooves (65 ± 6 µm against 55 ± 5 µm). The force-per-displacement curves and the cavity depth measurements are shown in APPENDIX F. In this case, the grooves on the metal surface were also completely filled by the polymer, ensuring adequate micro-mechanical anchorage of the polymer. A ULSF of 2249 ± 53 N was obtained (APPENDIX F). If the joining area is assumed to be equal to the nominal area of the recess of the metal insert that had been laser textured, i.e., 12.7 x 24.8 mm^2 (Figure 3.4), thus a ULSS of 7.2 ± 0.5 MPa is obtained.

The increase in nominal ULSS of the hybrid joints produced with deeper grooves at the metal surface were only 6 % (from ULSS of 6.8 MPa to 7.2 MPa) larger than the specimens C4 produced with shallower grooves metal inserts. This small increase in ULSS is due to the minor variation between the depth of

the grooves on the metal insert (55 µm for 4 scans and 65 µm for 8 scans). As observed by Rodrguez-Vidal *et al.* [14], this slight increase in depth is due to a saturation of scans, making it unable to produce deeper grooves.

This magnitude of joining strength is comparable to other polymer-metal joints produced by injection overmolding with metal inserts structured by laser-texturing [80–85,180], as well as those with metal inserts structured by sandblasting [53,62,78,89,134,181–183], anodizing [56,96,184,185], additive manufacturing [91], electron beam surface structuring [186], chemical treatments [50,86–90] and silanization [99–102].

4.1.3 Fracture analysis of PC/AA6061 joints

Figure 4.10 shows photographs of the fracture surface s after lap-shear testing on PC/AA6061 joints produced under C1, C4 and CP injection overmolding conditions (see Table 3.5). The joint produced with condition C1 failed locally with adhesive fracture. The little filling of polymer into the metal laser-formed grooves (Figure 4.6) led to a low level of micro-anchoring of the polymer on the metal surface and, thus lower ULSF (Figure 4.3). Under the optimized injection overmolding condition (C4) with complete filling of polymer into the metal grooves, one can see signs of cohesive fracture of the metal, which remained bonded to the polymer side (shown by the red squares, Figure 4.10b). Likewise, the PC/AA6061 joint produced under the center point condition (CP) with intermediate polymer filling level exhibits signs of cohesive metal fracture (Figure 4.10b, red squares) but in a smaller region than joint C4.

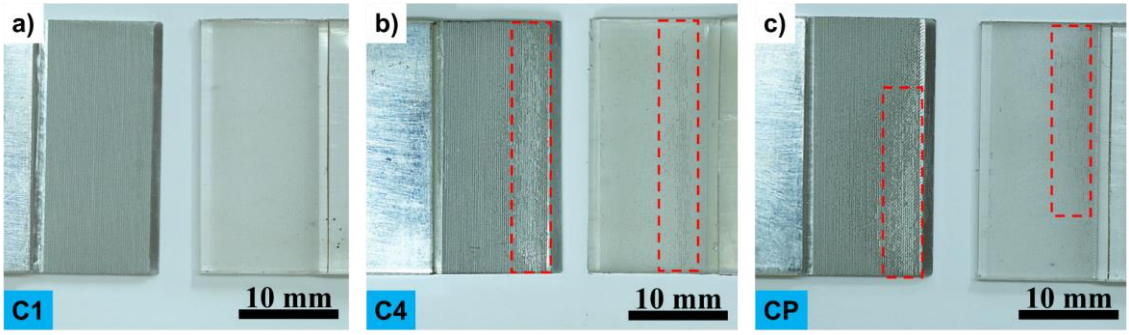

Figure 4.10: Fracture surface photographs of PC/AA6061 joints produced under a) C1, b) C4 and c) CP injection overmolding conditions. Red arrows indicate fracture of the strips formed on the metal surface.

Figure 4.11a-c shows SEM images (secondary electrons) of the fracture surface on the metal part of the PC/AA6061 joint produced at condition C4. Indications of cohesive fracture can be seen. It is possible to identify that a portion of the metal strips in between the grooves formed by laser texturing has been displaced in the longitudinal direction of the joint (Figure 4.11b). It is also possible to observe that a portion of the strips has been pulled out from the metal (Figure 4.11c).

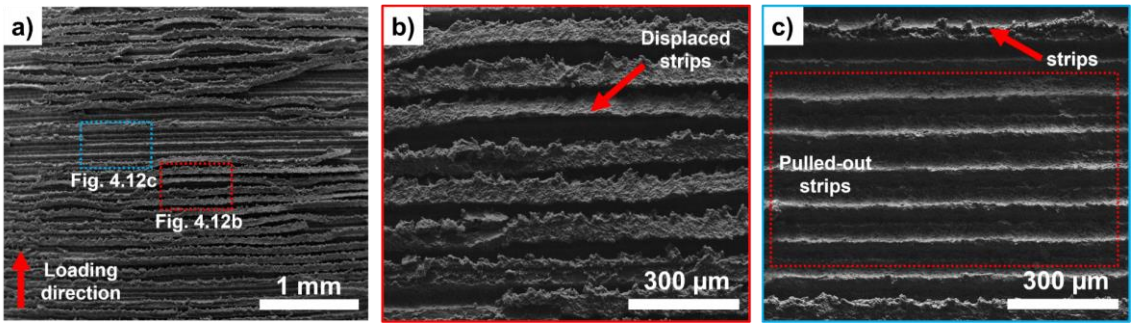

Figure 4.11:Scanning electron microscopy (SEM) images (secondary electrons) of the metal fracture surface of the PC/AA6061 joint produced with injection overmolding condition C4. a) Image with indications of cohesive fracture; b) Magnification of the region marked with red square where the strips were displaced; c) Magnification of the region marked with blue square where the strips were pulled out.

Figure 4.12 shows the fractured surface on the polymer side of the same joint viewed by SEM images with backscattered electrons (BSE) and energy-dispersive X-ray spectroscopy (EDX) mapping. Pieces of strips detached from the metal surface can be seen in the zone of cohesive fracture (Figure 4.12a and b). At higher magnification (Figure 4.12c and d), one can also observe aluminum fragments, which can be attributed to the resolidified metal (refer to Section 4.1.1, Figure 4.12), a material volume that is weakly adhered to the metal surface and was pulled out during joint lap-shear testing.

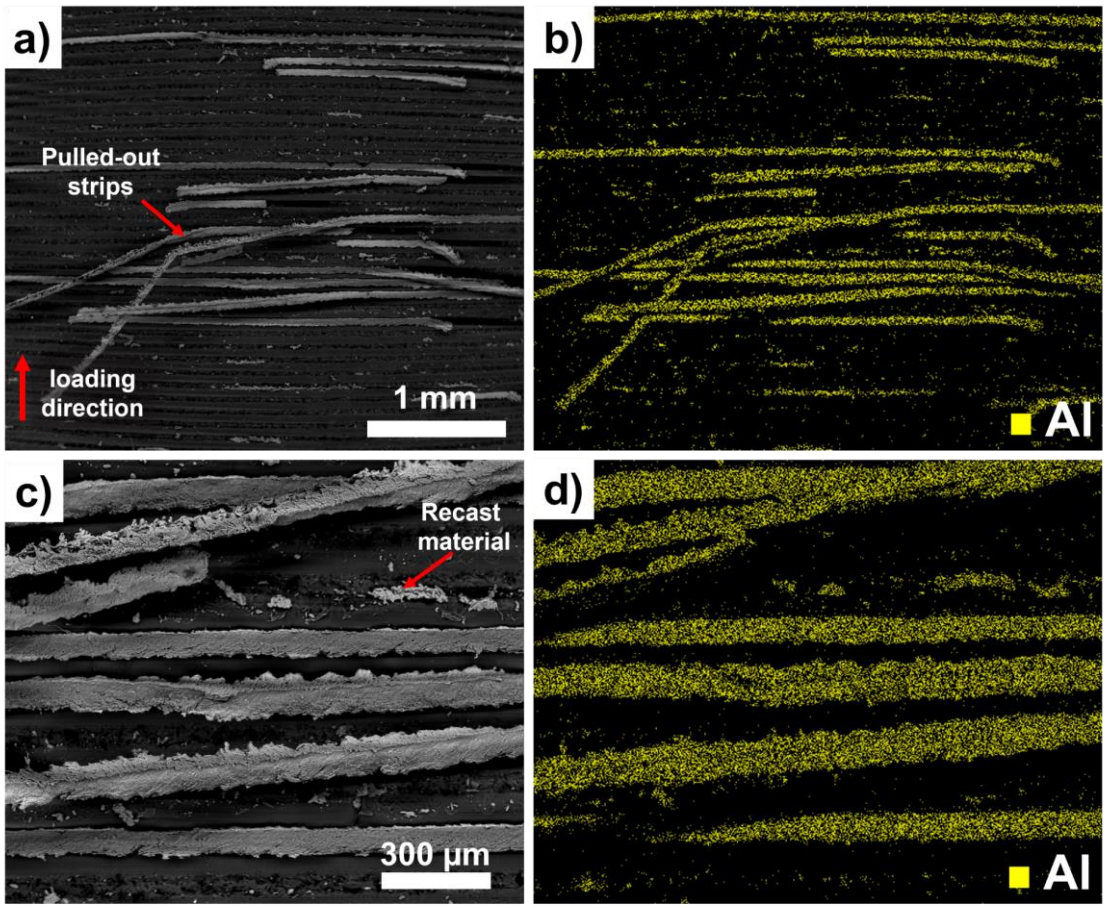

Figure 4.12: Scanning electron microscopy (SEM) images with backscatter electrons (BSE) (left side) and energy-dispersive X-ray spectroscopy (EDS) mapping of aluminum (right side) of the fracture surface on the polymer side of a PC/AA6061 joint produced in injection overmolding condition C4, a) and b) Low, and c) and d) high magnifications.

The main adhesion mechanism of the PC/Aluminum joints is the mechanical interlocking of the polymer into the metal grooves and this has been explored in the literature with different material combinations. Rodríguez-Vidal *et al*. [14] observed a dependency between the resolidified material height, density and aspect ratio (depth/diameter) of laser-formed grooves on ultimate lap-shear strength of joints with laser-textured low-alloy steel HC420 substrate and glass fiber reinforced polyamide 6 hybridized by injection overmolding. Byskov-Nielsen [80] observed an increase in joint strength with a higher density of dimples formed on the metal insert surface by laser. Similarly, Xu *et al*. [85] also observed that a higher density of grid-shaped grooves increases joint strength due to the greater number of grooves for mechanical interlocking with the polymer. Furthermore, one can speculate that the carbonyl groups on the PC chains (Figure 2.14) form Al–O–C chemical (covalent) bonds with the alumina layer on the surface of AA6061, as suggested by the studies of Li *et al*. [57] and Goushegir *et al.* [58].

Furthermore, digital image correlation (DIC) was used to monitor the displacement fields during lap-shear testing and thus provide additional information regarding the global failure mechanism of PC/AA6061 joints. A sample produced in the optimized injection overmolding condition (C4) was used.

Figure 4.13a-b depicts the maximum primary displacement field for a PC/AA6061 joint at a loading level of 1 kN. Figure 4.13a overlays with horizontal lines indicating the location of each groove engraved on the metal surface. The regions called front view and lateral view are shown in Figure 3.12. This qualitative DIC analysis was performed to determine the highest principal displacement fields in the PC/AA6061 joint manufactured with optimized parameters (C4). For quantitative analyses, greater refinement of DIC accompanied by finite elements analysis should be performed to obtain quantitative values of maximum principal displacement and force. However, this was out of the scope of this study.

The high displacement region at the top and bottom of the displacement field area in Figure 4.13a is due to the separation of the splice polymer-metal joint ends. These ends are not laser-textured and thus have poor polymer-metal adhesion, so they are quickly detached (delaminated) during the lap-shear

testing. The deformations on the overlap region are generally uniform, with a slightly higher displacement in the textured area on the polymer side. Moreover, it is noted that there is no considerable deformation at the lateral borders of the laser-textured area (region of the horizontal lines) due to the detachment of the polymer side owing to warpage [177–179], as shown and discussed in Figure 4.9. Figure 4.13b shows the lateral view of the joint with a quiver diagram superposed over the joint area. Due to the out-of-plane eccentricities of the structure and the difference in stiffness between the materials (see Table 3.1 and Table 3.2), secondary bending occurs at the metal end on the polymer side when the polymer-metal joint is subjected to loading [184,187–189]. This bending stress is responsible for the crack initiation in the lap-shear testing of the PC/AA6061 joint.

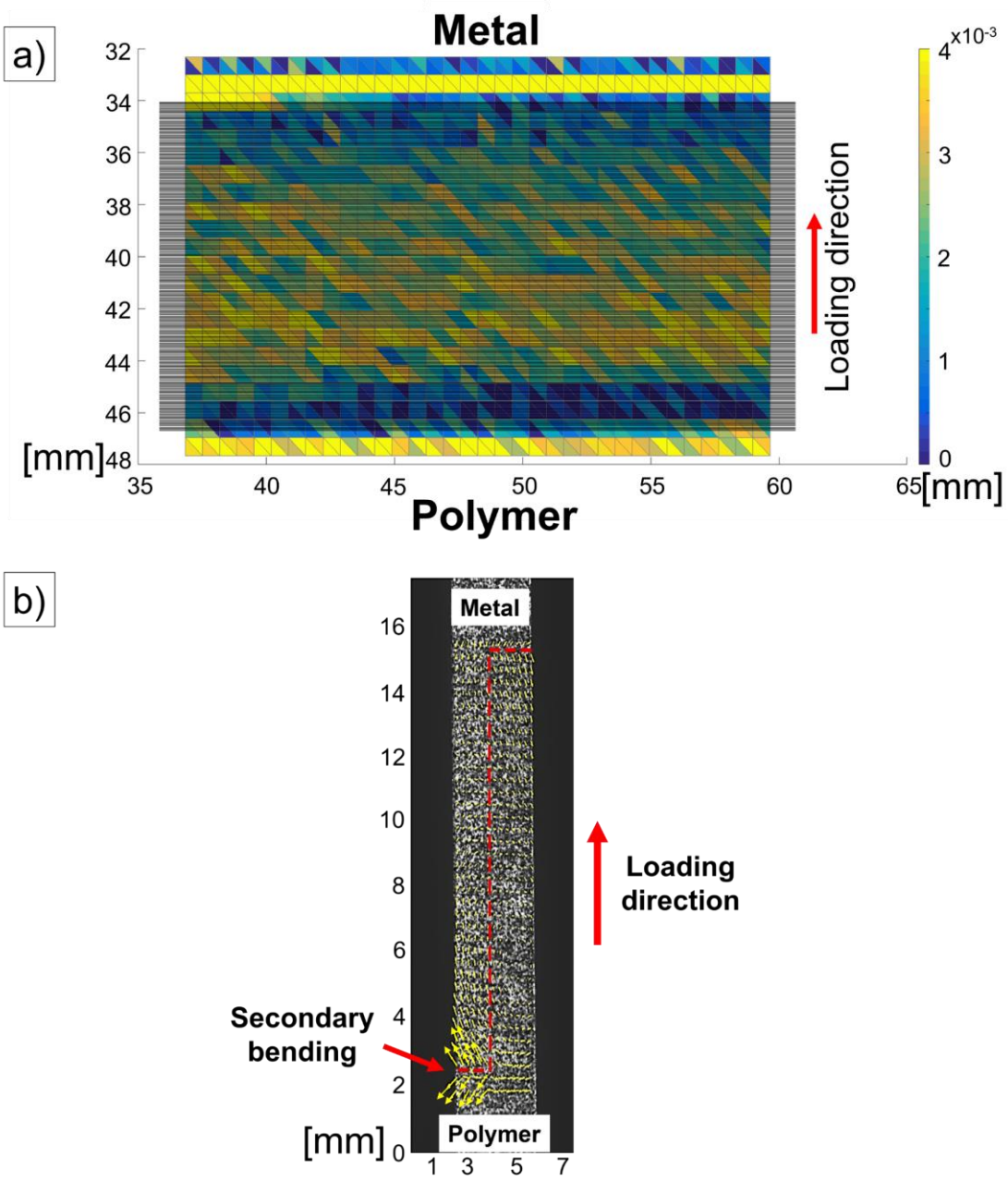

Figure 4.13: Images captured by digital image correlation (DIC) analysis for a PC/AA6061 joint injection overmolded in the optimized condition C4. a) frontal view: the maximum displacement at load level of 1 kN. On the displacement composition, a schematic depicting the position of the grooves textured by pulsed laser is superimposed; b) lateral view: Quiver diagram of deformation direction showing a secondary bending in the polymer side.

4.1.4 Fatigue behavior of PC/AA6061 joints

PC/AA6061 joints produced in the optimized injection overmolding condition (Table 3.4; Condition 4) were subjected to dynamic fatigue testing at 4 loading levels: 30%, 40%, 50% and 70% of the ULSF. Notably, all data reported in this section are displayed as load–life (F–N) graphs. Nonetheless, the term S–N curve (strength–life) is employed due to its extensive use in the scientific literature. The S-N curve is shown in Figure 4.14. Joints subjected to loads of 70%, 50%, and 40% failed after N = 70,000 ± 7,000; N = 464,000 ± 11,000; and N = 256,000 ± 17,000 cycles, respectively, by brittle net-tension fracture of the PC part near the end of the AA6061 insert (Figure 4.15), whereas joints subjected to a load of 30% endured 10^6 cycles without failure (the so-called run-out specimens), but with a visual onset of a transverse crack nucleating in the PC part near the end of the AA6061 insert.

For all loading levels applied, the polymer-metal interface of the joints remained intact, which attests to outstanding interfacial mechanical durability under cyclic loading. In the region where the joints failed, the PC part is subjected to a combined tensile (principal) and bending (secondary) stress, as indicated in the digital image correlation test (Figure 4.13b). If we make an approximation that this region, with a cross-sectional area of 24.8 $\times$ 1.6 mm^2 (width $\times$ thickness), is subjected to uniaxial tensile stress, then stresses of approximately 38 MPa, 27 MPa, 22 MPa, and 16 MPa would be developed, respectively, for 70%, 50%, 40%, and 30% of ULSF. PC tends to exhibit brittle fracture under these fatigue-loading conditions [190], which has been attributed to the plastic deformation mechanisms of PC - shear bands and crazing - do not develop sufficiently under cyclic loading; they rather act as stress concentrators through which a crack nucleates and propagates, resulting in brittle fracture of the polymer [191].

Furthermore, it should be noted that the high degree of PC molecular orientation resulting from injection overmolding high shear rates might increase the fatigue life of PC/AA6061 joints [191–193]**.** A log-linear (exponential) model [169] was utilized to fit the experimental S-N curve data. It is important to note that the inclusion of the point at 30% of ULSF is an approximation because under this condition, the run-out specimens did not fully fail; instead of this a crack was

initiated. These joints were subsequently subjected to quasi-static lap-shear testing resulting in a 61% residual strength, as shown in Table 4.2. In any event, the asymptotic behavior of the S-N curve suggests that the endurance limit of the PC/AA6061 joints is about 30% of ULSF.

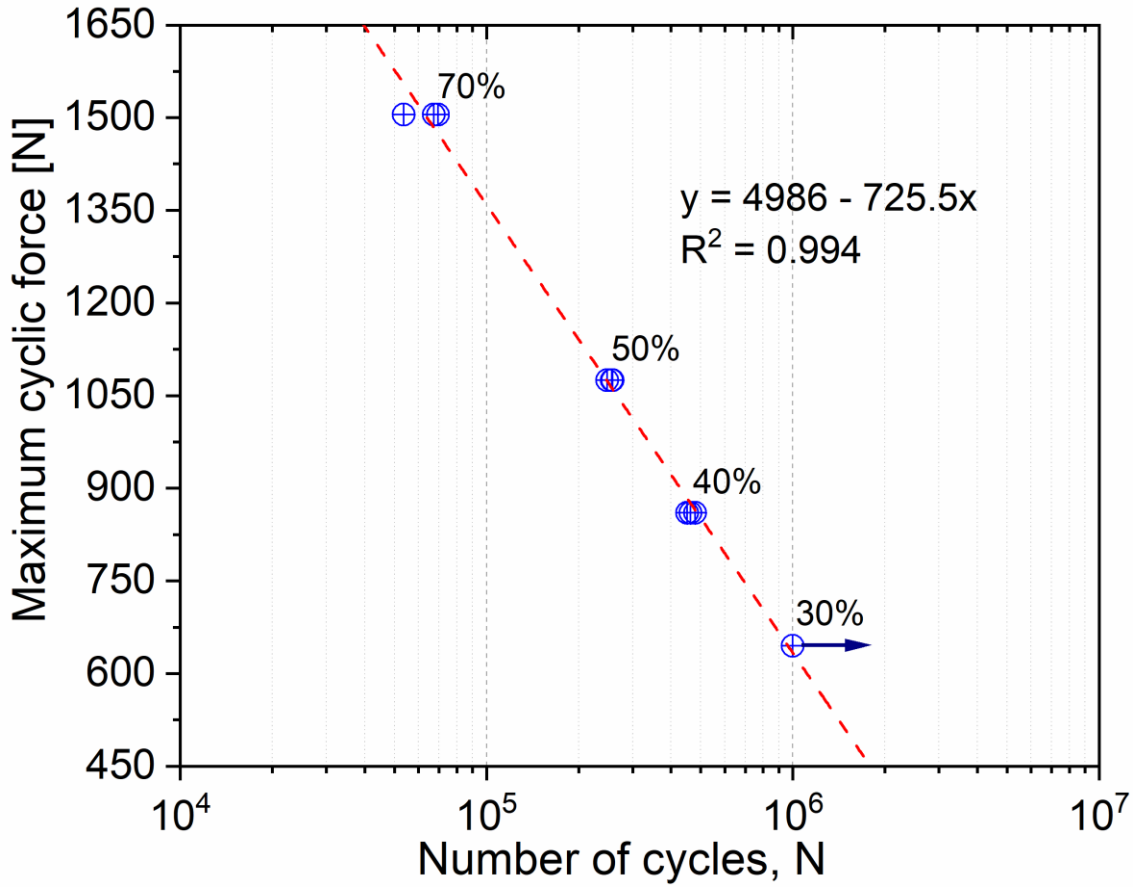

Figure 4.14: S-N curve in tensile mode (R = 0.1) at 5 Hz at load levels of 30%, 40%, 50%, and 70% of the ULSF for PC/AA6061 joints produced in the optimized injection overmolding condition. The experimental data were fitted by log-linear (exponential) model.

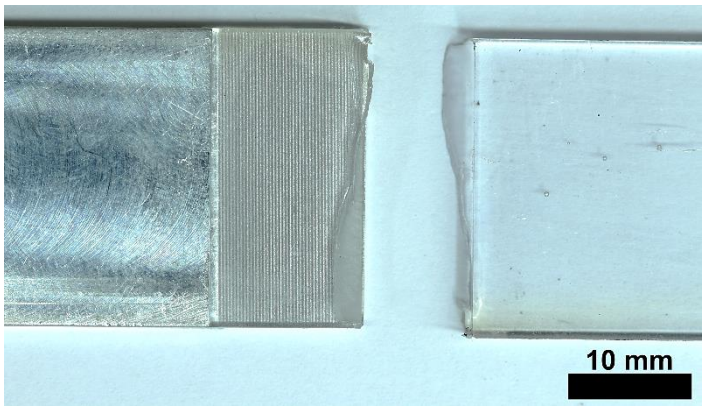

Figure 4.15: Photograph exemplifying the failure mode of the PC/AA6061 joints injection overmolded in the optimized condition (C4) subjected to fatigue (tensile; R = 0.1; 5 Hz) testing at loading levels of 40%, 50% and 70% of the ULSF. Detail of the transverse brittle fracture of PC near the end of the metal insert.

Table 4.2: Quasi-static residual lap-shear strength of PC/AA6061-laser-textured joints.

Samples	Force [N]
PC/AA6061-laser-textured	2149 ± 127
After 10^6 cycles	1315 ± 285

Fatigue strength studies on polymer-metal joints produced by injection overmolding are scarce in the literature. Nevertheless, the fatigue behavior of the PC/AA6061 joints is comparable or superior to those reported in the literature for similar systems. For instance, Zhao *et al*. [90] evaluated the fatigue strength of injection overmolded joints of PBT-30GF with AA5052 nanostructured by chemical and hot water treatment. They observed that optimized joints reached 10^5 cycles when subjected to milder conditions than those employed in this study, with cycling at 2 Hz and a tensile load of 15% of the ULSF.

4.1.5 Hygrothermal aging of PC/AA6061 joints

PC/AA6061 joints produced in the optimized injection overmolding condition (Table 3.4; Condition 4) were subjected to accelerated hygrothermal aging in a water bath at 80 °C for 1 day, 7 days, 30 days and then submitted to lap-shear testing. The samples were weighed before and after aging to evaluate

the water uptake. The ULSF after aging and the water absorption values are shown in Figure 4.16. The ULSF showed a 10% decrease after 1 day of hygrothermal aging, which were recovered after 7 days of hygrothermal aging. After 7 days of hygrothermal aging, the PC/AA6061 joint attained saturation (0.19%) for water uptake. Similar to unaged joints (Figure 4.10), hygrothermal aged joints exhibited mixed interfacial failure (adhesive-cohesive) in the lap-shear testing.

A possible explanation for the recovery in ULSF after 7 days of hygrothermal aging may be related to the polymer enhanced stiffness. Other studies have observed a similar trend with bonded joints [194–196].

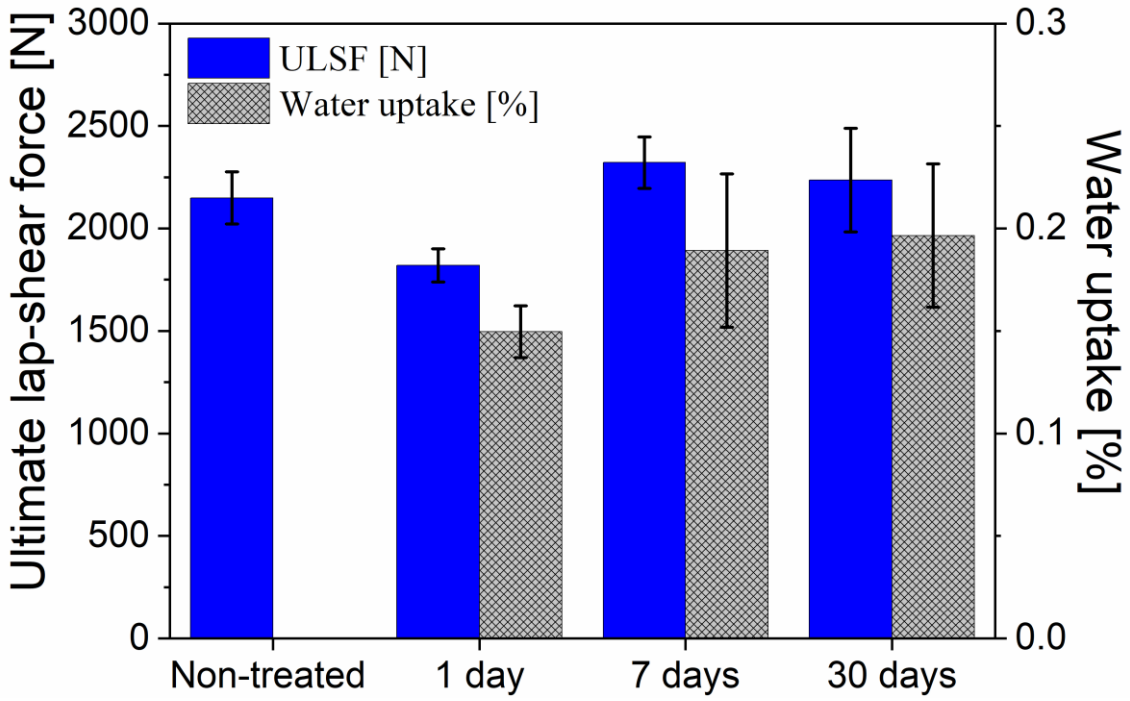

Figure 4.16: Ultimate lap-shear force (ULSF) and water uptake of PC/AA6061 produced in the optimized injection overmolding condition (C4) subjected to accelerated hygrothermal aging (immersion in an 80 °C water bath) for different periods.

Since the polymer component of the joints is primarily responsible for water absorption under the hygrothermal aging conditions adopted, i.e. water absorption by the AA6061 component is negligible. The glass transition

temperature (T_g) of the PC was determined using differential scanning calorimetry (DSC) analysis on samples taken from aged and unaged (control) PC specimens. DSC curves (Figure 4.17) revealed that the T_g, defined by an endothermic inflection of the heat flow curve at about 150 °C, is not appreciably affected by hygrothermal aging in water at 80 °C from 1 day to 30 days. Moreover, the unaged PC sample exhibits an endothermic event immediately above T_g (black arrow, Figure 4.17) which is not detected in the aged samples. This endothermic event above T_g is caused by the relaxation of polymer chains, which are initially in a glassy state but become mobile when heated over T_g. This relaxation results from the release of residual stresses associated with the orientation of the polymer chains, which are a result of the high shear and cooling rates imposed by the injection overmolding of PC specimens [197–199]. Therefore, the lack of the endothermic event slightly above T_g in the DSC curves of the PC samples aged in water at 80 °C at various periods suggests that hygrothermal aging of the PC/AA6061 joints led to release of residual stresses in the injection overmolded PC component.

Relaxation of the PC chains in PC/AA6061 joint samples submitted to hygrothermal aging may result in physical aging of the PC. When an amorphous, glassy polymer such as PC is exposed to extended hygrothermal aging, particularly around its glass transition temperature, these two opposing processes, water absorption and chain relaxation are observed. While water diffusion causes the polymer to expand, physical aging, which consists of the chains in the glassy state relaxing to an equilibrium state, causes the polymer to shrink (densification) [200].

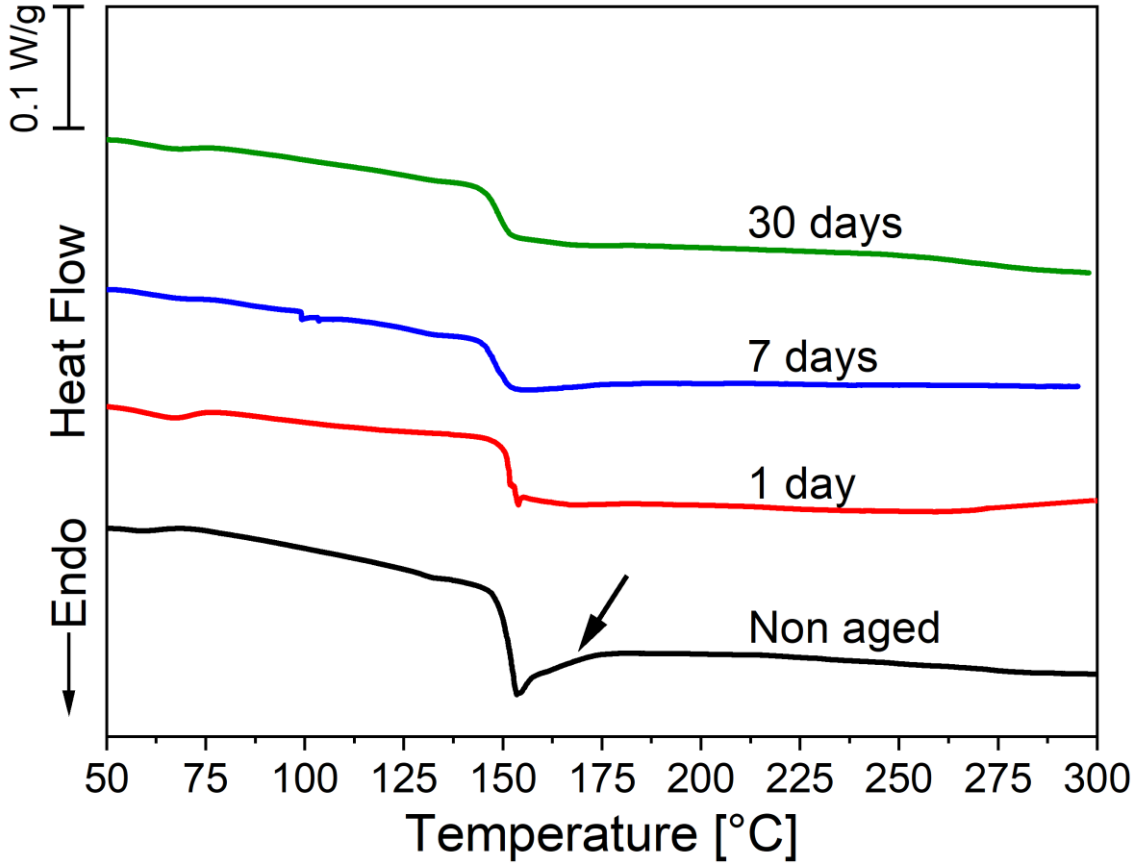

Figure 4.17: DSC curves (heating at 10 °C/min) of samples extracted from injection overmolded PC subjected to hygrothermal aging by immersion in water at 80 °C for 1 to 30 days.

In order to test whether there is competition between these two processes, polymer expansion and physical aging, PC samples were subjected to tensile testing before and after immersion in water at 80 °C for 30 days. In this hygrothermal aging condition, the PC sample absorbed 1% of water. The tensile properties of aged and unaged PC samples are shown in Table 4.3. The 30-days hygrothermal aging of PC did not significantly alter the stiffness (see Young modulus values) or yield stress, but it did reduce the ductility (see strain at break values) of the polymer. The comparable Young modulus and yield stress values of the 30-day aged and unaged samples show that the water absorption of the PC, which would lead to plasticization and a decrease in these properties, was probably counterbalanced by physical aging, which would lead to an increase in these properties. The decrease in the strain at the break of the aged sample

demonstrates that the two competing mechanisms, namely water diffusion and physical aging, result in structural defects that limit the ductility of the polymer.

Moreover, since the unaged and aged PC/AA6061 joints exhibited similar failure mechanisms in the lap-shear testing, with a mixture of adhesive fracture of the interface and traces of cohesive fracture of the AA6061 surface, and with little contribution of viscoelastic or plastic deformation of the PC component, water diffusion and physical aging of the PC component due to hygrothermal aging did not significantly contribute to the ULSF of these joints. Therefore, the residual strengths of the aged PC/AA6061 joints were close to those of the unaged joints (Table 4.3), indicating that the PC/AA6061 joints have good hygrothermal stability.

Table 4.3: Mechanical properties under tensile testing for injection molded polycarbonate grade LEXAN 103 before and after 30 days of hygrothermal aging.

	Young Modulus (GPa)	Yield stress (MPa)	Strain at break (%)
Non-aged PC	2.4 ± 0.1	58.6 ± 0.9	79 ± 10
30 days aged PC	2.3 ± 0.1	59.1 ± 0.5	39 ± 23

4.2 PC/AlSI10Mg hybrid joints

As presented in Section 3.1 (Figure 3.1), this second part consisted of additive manufacturing and characterization of AlSi10Mg inserts followed by lap-shear testing, fracture analysis and fatigue testing of PC/AlSi10Mg joints produced with the optimized injection overmolding condition.

4.2.1 Density and surface roughness analyses of 3D-printed AlSi10Mg inserts

Figure 4.18 shows the average relative densities for AlSi10Mg printed parts as a function of the laser powder bed fusion (L-PBF) parameters (see Table 3.4). Experimental values of relative density ranged from 91.5 ± 1.2% (condition 5) to 98.5 ± 0.2% (condition 2).

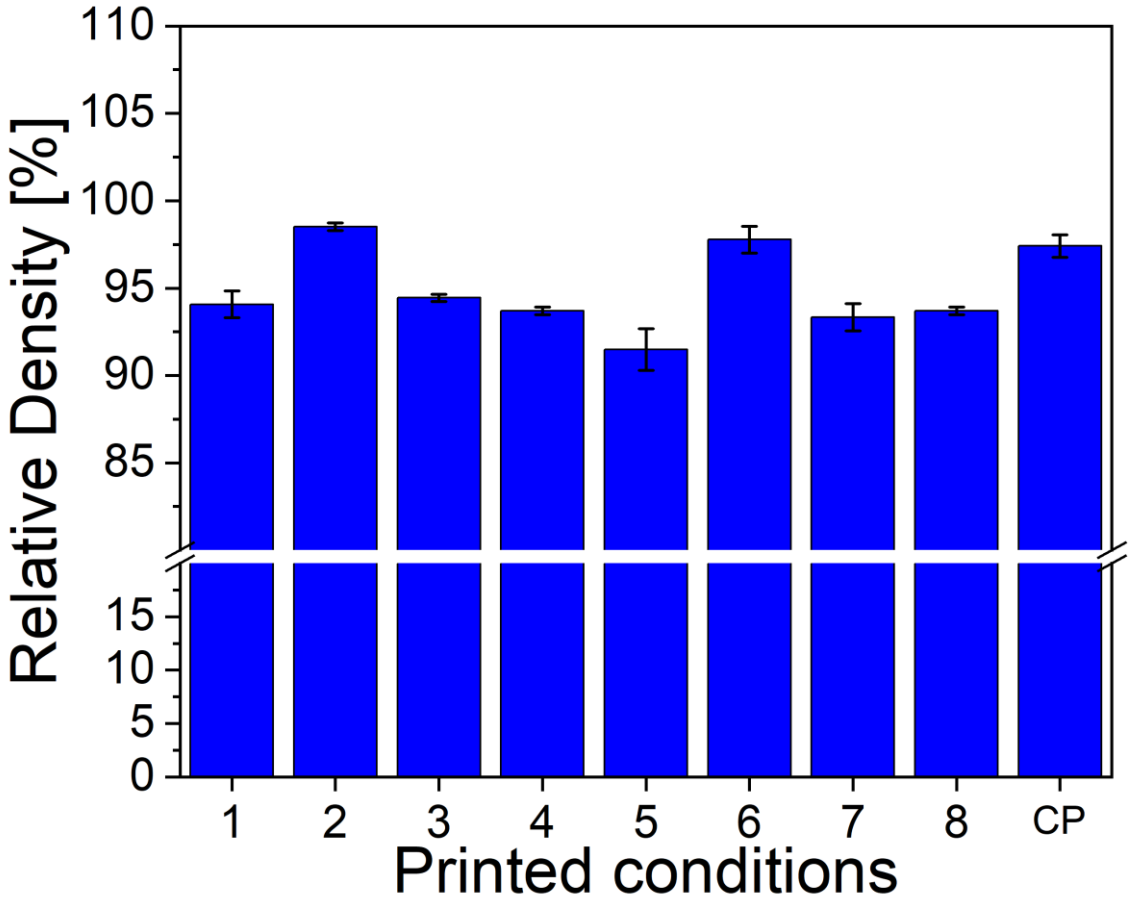

Figure 4.18: Relative density of AlSi10Mg parts printed via laser powder bed fusion (L-PBF) as a function of the printing parameters (Table 3.5).

After identifying the parameters with the highest effect on the relative density via DoE and ANOVA (see APPENDIX A), samples were printed with mushroom-like structures on the substrate surface with higher relative density conditions (conditions L-PBF-2, L-PBF-6 see Table 3.4) for roughness measurement and assessment of the definition of the submillimeter structure dimensions. SEM images of mushroom-like structures with printed under the two largest L-PBF conditions are depicted in Figure 4.19. The R_a for the substrate printed with the condition L-PBF-2 was 45 µm ± 18 µm, higher than the R_a of 26 µm ± 14 µm for condition L-PBF-6 with a similar relative density (98%), as shown in Figure 4.18. When visually comparing the dimensions and surface finishing of the mushroom-like structures 3D-printed in the condition L-PBF-2 (Figure 4.19a) to those using the L-PBF-6 (Figure 4.19b) conditions, a clearer definition of the

contours and proportions of the mushroom-like structure was achieved for the condition L-PBF-6.

In order to understand the influence of process parameters on the roughness, one may use Energy density (Ψ) as the measure of heat input by the L-PBF process. There are two ways of calculating Ψ [201] 1) one considering the laser power (P), laser scan speed (v), layer height (h) and hatching distance (HD) showed in Equation 4.3 [202]; and 2) considering the time interaction (D_b/v) and laser spot diameter (D_b) in place of their implicit addition from hatching distance (HD) showed in Equation 4.4 [203].

$$\Psi_1 = \frac{P}{v * HD * h} \tag{4.3}$$

$$\Psi_2 = \frac{4P}{\pi D_b^2} * \frac{D_b}{v} \tag{4.4}$$

On the one hand, the condition L-PBF-2 has the highest energy density among the two 3D-printing conditions (see Table 4.4) because of its smallest hatching distance (HD = 40 µm) and laser spot diameter (D = 40 µm) at the same laser power and laser scanning speed than L-PBF-6, increasing Ψ (Equations 4.3 and 4.4). This probably causes an excessive increase in the temperature to the point where the metal melts and forms a molten pool. This melt pool surface is also accompanied by more intense alloy element evaporation, and the powder surrounding the irradiated region is ejected during the process and then falls on the surrounding surface by gravity and adheres to the surface of the melted pool during solidification [204]. On the other hand, the condition L-PBF-6 has a higher laser spot diameter (60 µm) than the L-PBF-2 (40 µm) and larger hatching distance (120 µm), which reduces the intensity of energy irradiated by the laser and reduces the intensity of the evaporation on the melt pool surface, i.e. decreases Ψ (Equations 4.3 and 4.4). This decrease in energy density seems to have led to a more stable printing of the mushroom patterns at such submilimetrical scale. It is speculated when the energy density is high, the laser

energy is concentrated in a small volume of the powder bed, leading to rapid melting and consolidation of the powder particles. This rapid heating and cooling can cause distortions in the dimensions of the submillimetrical structures. Moreover, for an optimal energy density, the laser energy is distributed more evenly across the powder bed, and the melting and consolidation of the particles occur gradually. As a result, the molten material has more time to solidify and coalesce, leading to a smoother surface finish and higher submillimetrical structures definition.

Table 4.4: Conditions of the design of experiments and volumetric energy density Ψ_1 e Ψ_2 according Equations 4.3, and 4.4 respectively.

Condition	P $[w]$	V $[mm/s]$	D $[\mu m]$	h $[\mu m]$	HD $[\mu m]$	Ψ_1 $[j/mm^3]$	Ψ_2 $[j/mm^3]$
L-PBF - 1	150	750	40	60	120	28	6.4
L-PBF - 2	240	750	40	20	40	400	10.2
L-PBF - 3	150	1500	40	20	120	42	3.2
L-PBF - 4	240	1500	40	60	40	67	5.1
L-PBF - 5	150	750	60	60	40	83	4.2
L-PBF - 6	240	750	60	20	120	133	6.8
L-PBF - 7	150	1500	60	20	40	125	2.1
L-PBF - 8	240	1500	60	60	120	22	3.4
CP	195	1125	50	40	80	54	4.4

Furthermore, using the parameters improved (condition L-PBF-6; Table 3.4) with one of the largest relative density of 98% AlSi10Mg parts printed by laser powder bed fusion (L-PBF), a total of three submilimetrical structures – i.e. mushroom, inkpot, and lattice (see Figure 3.7) - were produced on the metal surface. Different leaning angles ranging from 0° to 90° with a 10° pitch (see Figure 3.6b) were tested to further evaluate the influence of downskin on the roughness influencing the 3D-printing integrity of the parts. The average surface roughness (R_a) as a function of the entire range of printing angles is shown in Figure 4.20. Figure 4.21 shows SEM images of these structures produced with selected parts printed at 0°, 45°, 90°. One can identify two plateaus of surface

roughness in Figure 4.20, the first from 0° to 50° with R_a of approximately 20 µm and the second from 60° to 90° with R_a of approximately 35 µm.

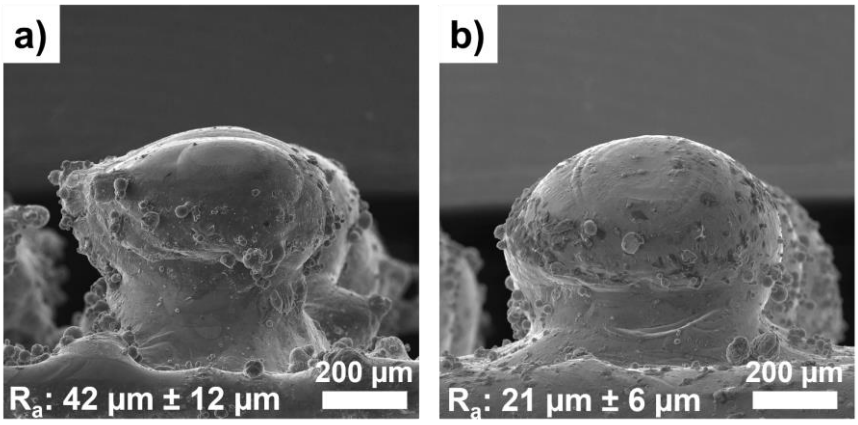

Figure 4.19: Scanning electron microscopy (SEM) images and average roughness (Ra) of a submillimeter mushroom-like structure printed on the AlSi10Mg part at different laser powder bed fusion (L-PBF) conditions. a) condition 2 (L-PBF-2); b) condition 6 (L-PBF-6), see Table 3.4.

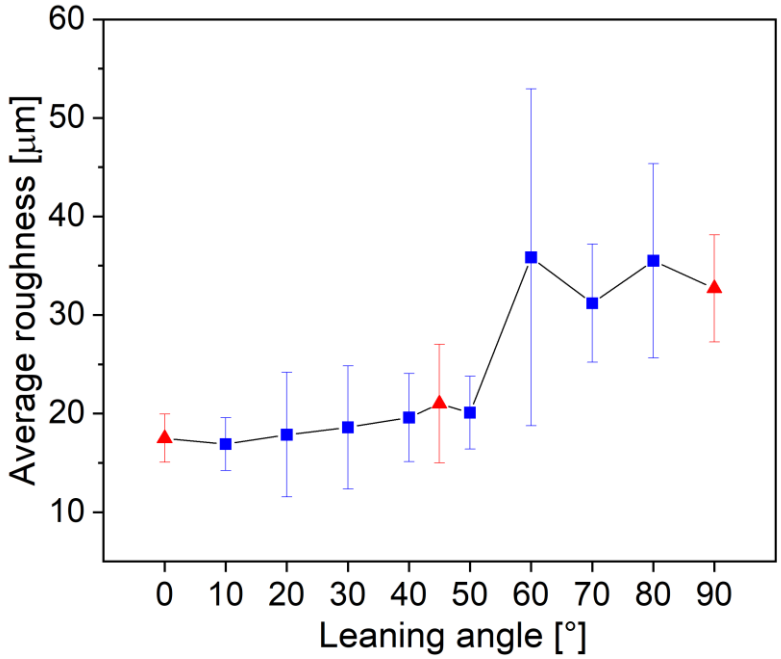

Figure 4.20: Average surface roughness a L-PBF-printed part with mushroom-like structures on the surface and parameters from condition L-PBF-6 (see Table 3.4) at different leaning angles (see Figure 3.6b). The structured surfaces at the angles marked by the red triangle symbol plot are shown in Figure 4.21.

This increase in the average roughness occurs due to the effect of the molten pool constantly moving downward by gravity during solidification, and the tensile effect at the solid-liquid interface is not sufficient to restrain the movement of the molten pool [115,204]. Moreover, when the molten material solidifies, the surrounding powder is continuously absorbed and drawn around it, forming partially melted particles on the solidified surface [116], as shown for all structures depicted in Figure 4.21 in different leaning angles. Furthermore, for surfaces with submillimetrical structures, there is a collapsed of the structures in the part printing angle range of 50° to 90° caused by gravity during solidification, as depicted in the SEM images of Figure 4.21 for the submillimetrical surfaces (inkpot, lattice and mushroom) printed at angle of 90º.

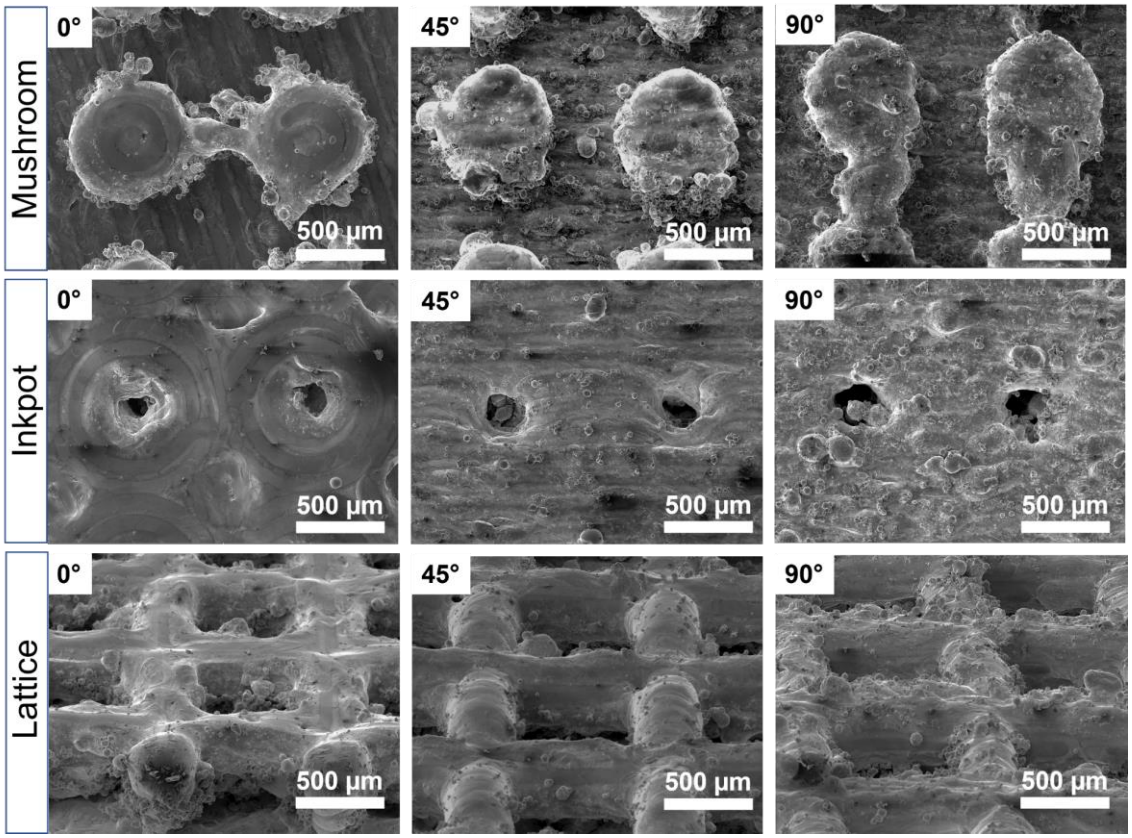

Figure 4.21: Images of scanning electron microscopy (SEM) of the AlSi10Mg printed surface with three types of submillimetrical structures (mushroom, inkpot, and lattice) (see Figure 3.7) manufactured with part printing angles of 0°, 45°, 90° (see Figure 3.6b).

The L-PBF-6 condition with a 45° printing angle, which resulted in a relative density of 98 ± 0.7% and R_a of 21 ± 6 μm was selected based on the study of the influence of the L-PBF-parameters and leaning angle on the relative density, average roughness, and definition of the structures. Metal inserts without and with submillimeter structures (inkpot, mushroom, and lattice) were 3D-printed following this procedure.

4.2.2 Lap-shear behavior of PC/AlSi10Mg joints

The PC/AlSi10Mg hybrid joints were manufactured using an injection overmolding machine as a half-lap splice joint (Figure 3.11). Submillimetrical structures (inkpot, mushroom, and lattice) were printed on an area of roughly ¼ square inch (half the surface area of the recess of the metal insert) with parameters from condition L-PBF-6 and leaning angle of 45°. The as-built condition (without submillimetrical patterns) were additionally 3D-printed for comparison purposes. For manufacturing these joints, the optimized injection overmolding condition selected with AA6061 inserts was employed (Condition 4 in Table 3.5).

The PC/AlSi10Mg joints were subjected to lap-shear testing and experimental results are shown in Figure 4.22. Typical force vs. displacement curves are shown in APPENDIX G. PC/AlSi10Mg joints prepared with as-built and inkpot structured metal inserts presented very low ULSF and displacement at break values. In contrast, the lattice and mushroom metal structuring resulted in strong PC/AlSI10Mg joints with excellent ULSF of 1400 N ± 230 N and 1613 N ± 303 N, respectively. The highest ULSF value of PC/AlSi10Mg specimens corresponds to about 70% of the force required for the ductile failure of PC (2285 N, value obtained in the tensile strength testing, Section 4.1.5) component to undergo yielding during lap-shear testing.

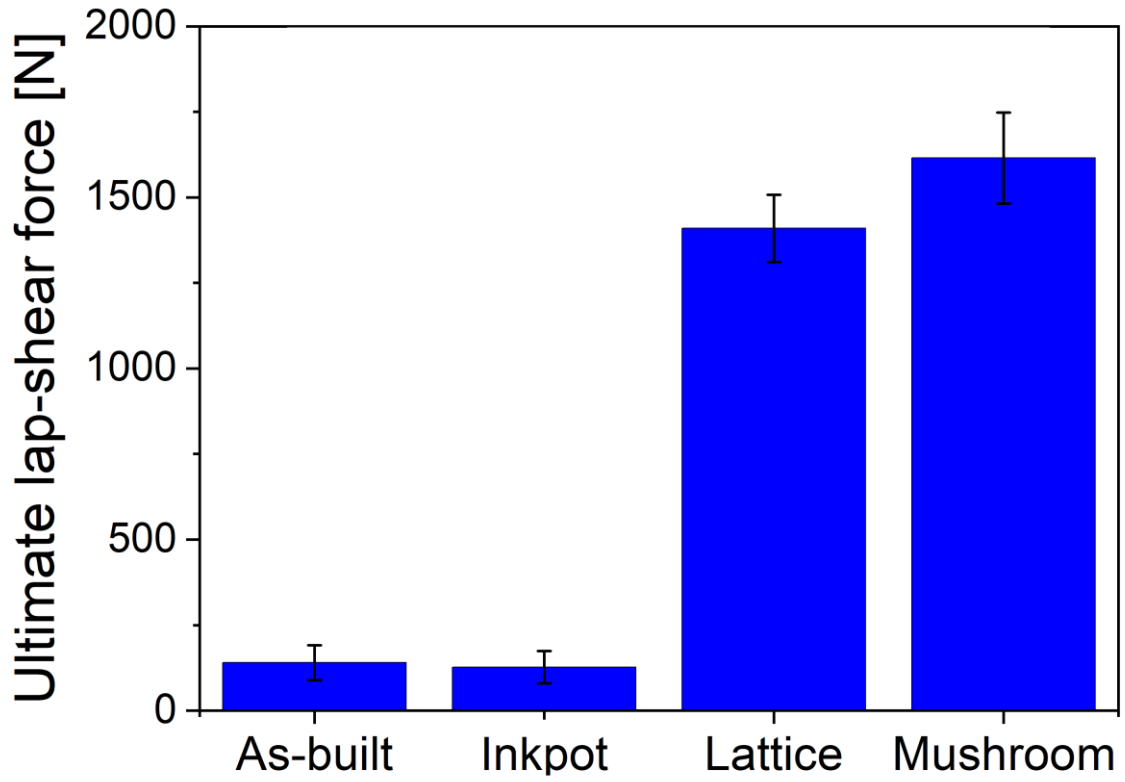

Figure 4.22: Ultimate lap-shear force (ULSF) of injection overmolded PC/AlSi10Mg joints injection overmolded in the optimized condition C4 (see Table 3.5).

Optical microscopy images of the cross-section of PC/AlSI10Mg joints prepared with additive manufactured metal inserts with different surface structures are shown in Figure 4.23a-d. For the as-built AlSI10Mg structuring, the injection overmolded PC could wet and adhere to the metal surface irregularities produced by additive manufacturing (Figure 4.23a). In the case of the inkpot structuring, as shown in Figure 4.23b and indicated by the red arrow, the injection overmolded PC was unable to fill completely the inkpot cavities. This can be attributed to air trapping within the inkpot that prevents the molten polymer from infiltrating into the metal cavities [52,79,205]. The PC/AlSI10Mg joints prepared with the as-built metal structuring presented low ULSF (Figure 4.22). Likewise, the ULSF of the PC/AlSI10Mg joints prepared with the inkpot structuring was also low (Figure 4.22). For the lattice structuring, the injection overmolded PC partially filled the spaces between the metal structures; voids (indicated by the blue arrows in Figure 4.23c) are formed at the bottom of the metal structures. In the case of

PC/AlSI10Mg joints prepared with metal inserts containing mushroom structures on the surface, the injection overmolded PC filled the space between the structures completely, as shown in Figure 4.26d. The PC filling obtained in the lattice and mushroom structures made it possible to obtain good mechanical anchoring and thus strong PC/AlSi10Mg joints (Figure 4.22). The PC/AlSi10Mg joints prepared with metal inserts with lattice and mushroom structures on the surface achieved lap-shear strengths of 17.8 ± 2.9 MPa and 20.5 ± 3.8 MPa, respectively, if the joining area was assumed to be equal to the nominal area of the recess of the metal insert that had been structured by additive manufacturing, i.e., 6.35 x 12.4 mm^2 (Figure 3.11). These lap-shear strengths are about 2-3 times higher than the 7.3 ± 0.4 MPa achieved for the PC/AA6061 joints prepared with laser-textured metal inserts (Section 4.1) and can be considered above-average when compared to those of other polymer-metal joints produced by injection overmolding with metal inserts structured with other techniques such as laser-texturing [80–85,180], sandblasting [53,62,78,89,134,181–183], anodizing [56,96,184,185], additive manufacturing [91], electron beam surface structuring [186], chemical treatments [50,86–90] and silanization [99–102]. Studies on injection overmolded polymer-metal hybrid structures prepared with metal inserts produced by additive manufacturing are scarce in the literature. No data was found for the combination of materials used in this work. An example of the literature by Verma *et al*. [91] used lattice-structured 316L stainless steel inserts prepared by L-PBF to manufacture joints with glass-fiber reinforced polyaryletherketone composite (PAEK-GF). Joints presented outstanding pull strength and mixed cohesive failure, confirming the potential of this approach.

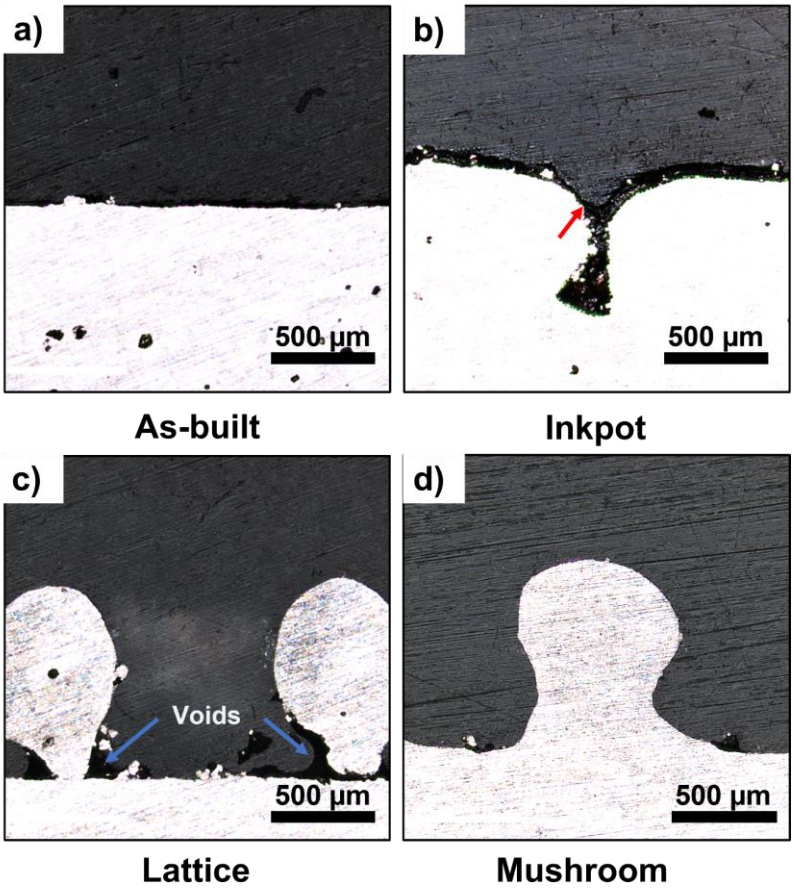

Figure 4.23: Optical microscopy (OM) images of the cross-section of PC/AlSi10Mg joints prepared with additively manufactured metal inserts with structured surfaces with: a) as-built; b) inkpot; c) lattice; and d) mushroom. Dark area: PC. White area: AlSi10Mg. Red arrow: the injection overmolded PC was unable to fill the inkpot cavities completely. Blue arrow: voids due to lack of polymer filling.

4.2.3 Fracture analysis of PC/AlSi10Mg joints

The failure mechanisms of the PC/AlSi10Mg hybrid joints subjected to lap-shear testing depend on the surface structure applied to the metal insert. Photographs of the metal and polymer fracture surfaces of the joints are shown in Figure 4.24.

PC/AlSi10Mg hybrid joints prepared with as-built metal inserts failed mostly due to interfacial shear failure, as shown in Figure 4.24a. In addition, SEM analysis (Figure 4.25) revealed a few metal particles - which were presumedly

weakly adhered to the metal surface - attached to the polymer surface (as illustrated by the red arrows in Figure 4.25b). This suggests that local cohesive fracture took place on the surface of the as-built lap-shear specimens. However, these polymer-metal interactions were not enough to ensure strong adhesion leading to weak joints with low ULSF value of 140 N ± 50 N (Figure 4.22).

The PC/AlSI10Mg joints with inkpot-type structures likewise failed mostly due to interfacial shear failure (Figure 4.24b). SEM analysis (Figure 4.26) showed incomplete polymer filling in the metal cavities. SEM analysis also revealed isolated metal particles adhered to the polymer surface, as indicated by the red arrows on the polymer side (Figure 4.26d). This weak interfacial interaction also resulted in a low ULSF value (130 N ± 47 N), which is comparable to that of the joint with an as-built metal insert (Figure 4.24).

In the case of PC/AlSI10Mg hybrid joints with lattice structuring, failure was caused by a combination of delamination at the ends of the metal side followed by a tear-out failure (Figure 2.7c) of the PC component outside the overlap zone (Figure 4.24c), indicating good interfacial adhesion, which led to an excellent ULSF value (Figure 4.22). The maximal interfacial strength of this structure, however, could not be determined due to ductile polymer fracture. The fracture mechanisms of polycarbonate have already been extensively studied in the literature and yield shear band deformation or occur by sliding in specific shearing planes [206,207]. Moreover, the shear bands, which are narrow, flat zones of high shear deformation, are started in locations with a stress concentration or minor internal or external imperfections [146]. Thus one may deduce that the crack initiation occurred at the ends of the region with lattice structures on the polymer side.

The PC/AlSI10Mg joints with mushroom structuring failure occurred mostly due to cohesive fracture at the base of the metal mushrooms. This helps to confirm the presence of micro-mechanical interlocking between metal mushrooms and the polymer part (Figure 4.24d). SEM analysis indicates the first row of pins was fractured by the action of a mixture of local tensile and bending loads related to the secondary bending (Section 2.2, Figure 2.4), i.e. out-of-plane

loading, as depicted in Figure 4.27a (first row of mushrooms indicated by white arrows) showing stretched pins.

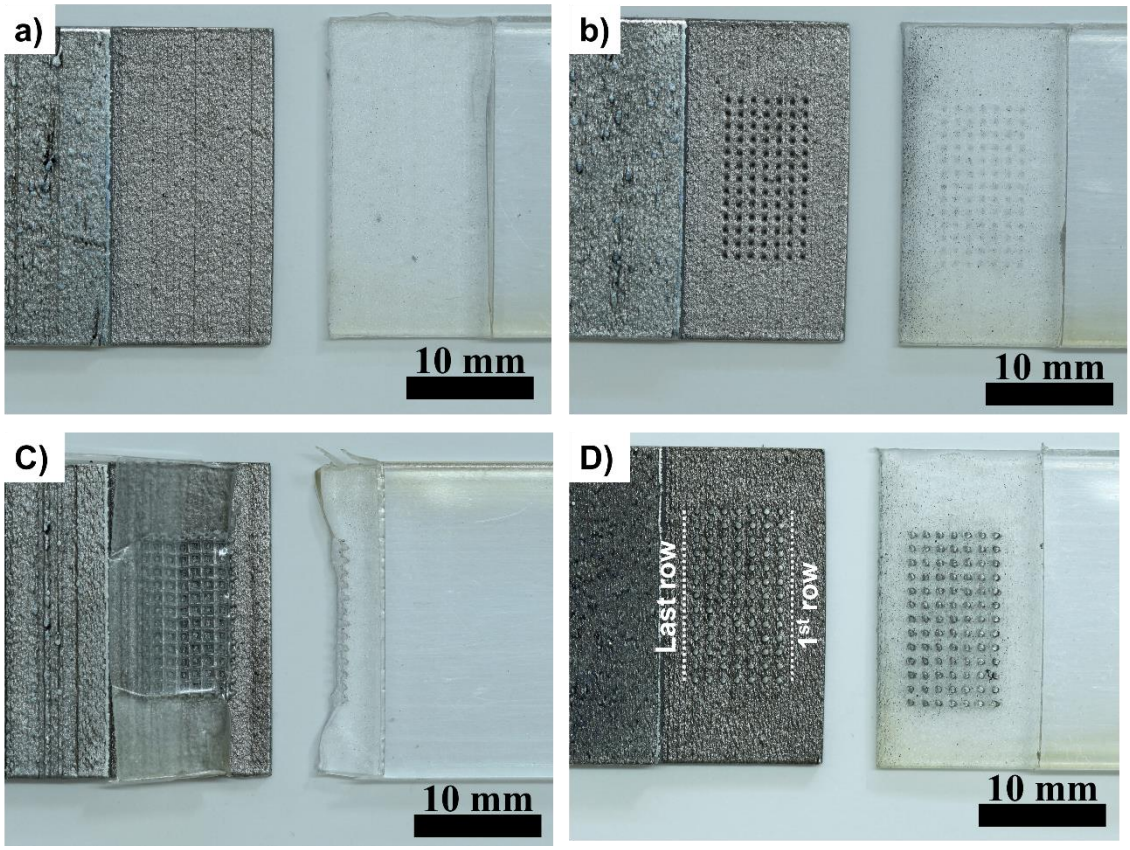

Figure 4.24: Metal and polymer fracture surfaces of PC/AlSi10Mg hybrid joints prepared with additively manufactured and structured metal inserts subjected to lap-shear testing. a) As-built surface; b) Inkpot-like structures; c) Lattice structures; d) Mushroom-like structures. Hybrid joints were produced with the optimized parameters Condition C4 (Table 3.5) and L-PBF-6 (Table 3.4) for injection overmolding and 3D-printing of metal inserts, respectively.

In Figure 4.27b shows an example of a stretched mushroom displaying this mixed type of cohesive failure. The adjacent rows were fractured by shear near the base of mushrooms (Figure 4.24b-c), as a change in the state of stress and strain distributions took place as the crack front propagates along the metal-polymer interface.

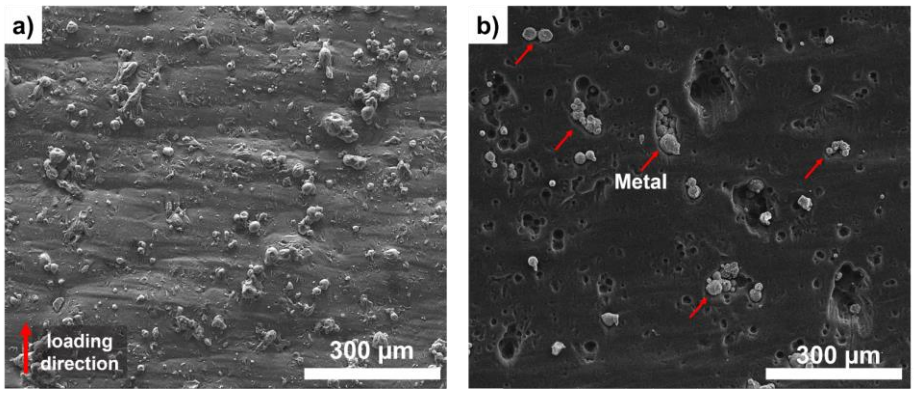

Figure 4.25: SEM images of the fracture surfaces of a PC/AlSi10Mg hybrid joint prepared with as-built L-PBF metal structuring subjected to lap-shear testing. a) metal surface; b) polymer surface (red arrows indicate metal fragments adhered to the polymer).

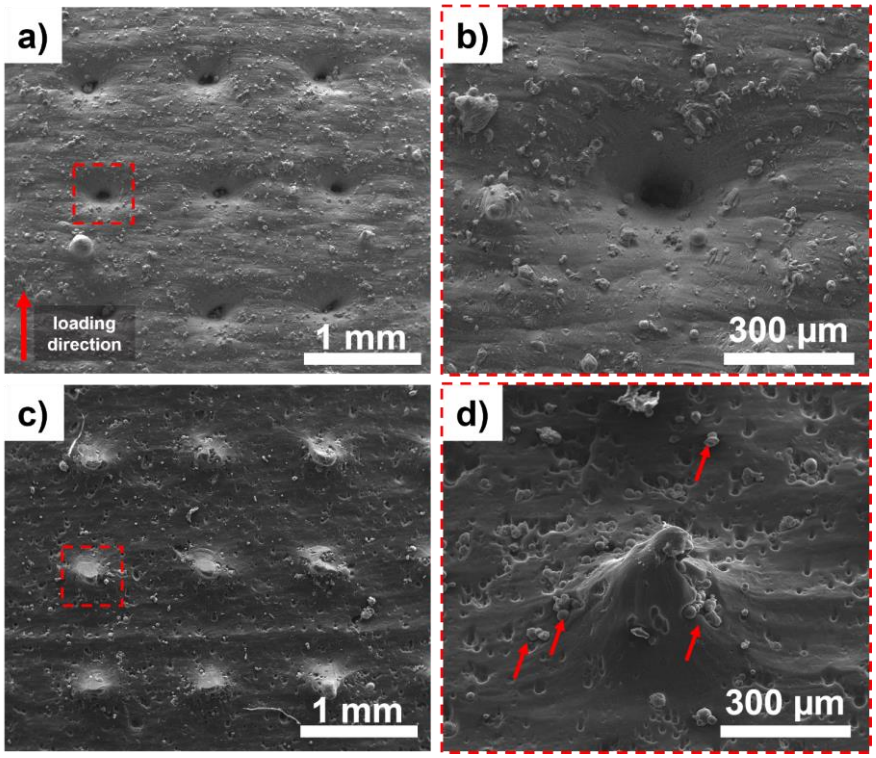

Figure 4.26: SEM images of the fracture surfaces of a PC/AlSi10Mg joint prepared with inkpot metal structuring subjected to lap-shear testing. Metal surface: low (a) and high (b) magnifications; polymer surface: low (c) and high (d) magnifications (red arrows indicate metal fragments adhered to the polymer).

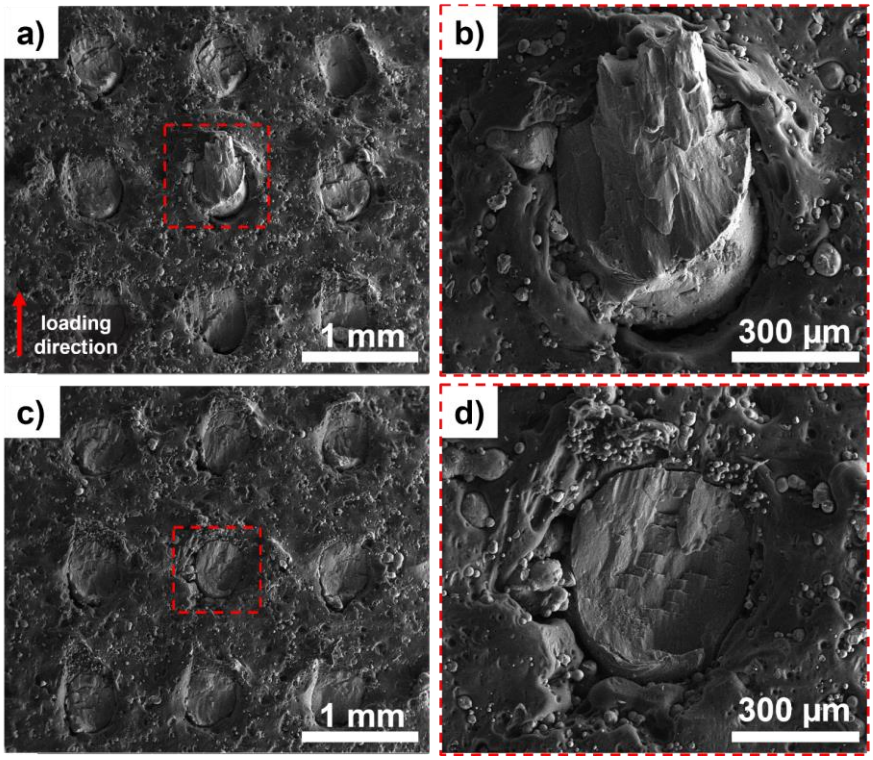

Figure 4.27: SEM images of the polymer fracture surface of a PC/AlSi10Mg joint prepared with mushroom metal structuring subjected to lap-shear testing. First row of mushrooms as indicated in Figure 4.24d: low (a) and high (b) magnifications; last row of mushrooms as indicated in Figure 4.24d low: (c) and high (d) magnifications.

Digital image correlation (DIC) was also used to monitor the displacement fields during lap-shear testing and thus provide additional information regarding the failure mechanism of PC/AlSi10Mg joints. A sample with mushroom-like structuring was chosen due to its resulting highest ULSF value (1613 N, 4.2.2, Figure 4.22). as well as because of its distinctive fracture at the base of the mushroom-like structures (Figure 4.27).

Figure 4.28a depicts the maximum principal displacement field of a loaded joint at 1 kN. On the displacement fields, a diagram depicting the dimensions and position of each structure mushroom head is superimposed. Moreover, the range of displacements values on the color map was constrained to 0.01 to emphasize the values in the region containing the mushroom-like structures due to the extremely high deformation values in the upper, final region of the polymer-metal

overlap on the polymer side. It is important to note that this is an exploratory study since a more complex DIC treatment must be conducted to account for out-of-plane surface deformations. The calculated displacement fields in the polymer reveal a concentration of displacement in the lowest row of mushrooms, referred to as the first row. The second row is positioned in a zone with minimal deformation, showing that the first and second rows anchor the polymer and limit its deformation. In addition to the interfacial shear stress, the polymer component (PC) is subjected to a secondary bending at the region towards the end of the metal component (Figure 4.28b), similar to the secondary bending effect found for PC/AA6061 joints (Figure 4.13b).

In a nutshell, as for the laser treated AA6061 substrates, the AlSi10Mg structured substrate joint showed improved bonding strength at the interface by mechanical micro-anchoring of the PC to the 3Dprinted structures (i.e. the submilimetrical structures), especially the mushroom and lattice types. Similarly, Verma *et al*. [91] obtained high mechanical strength joints by soft anchoring glass-fiber reinforced polyaryletherketone (PAEK-GF) on 3D-printed steel substrates with different surface structures. Finally, it is important to add that covalent bonds may also have occurred between the CP and the metal insert, as identified in the studies of Li *et al.* [57] and Goushegir *et al.* [58]

Another side-study led by the PhD-thesis author also used those metal inserts with mushroom-like structures printed in condition L-PBF-6 to produce strong PC/AlSi10Mg hybrid joints entirely through additive manufacturing, in which PC was deposited on the metal side by fused filament fabrication (FFF) [16]. The large lap-shear strength results reported in this s study help to support the choice of the mushroom structures as the most adequate submillimetrical feature when combining AlSi10Mg with PC.

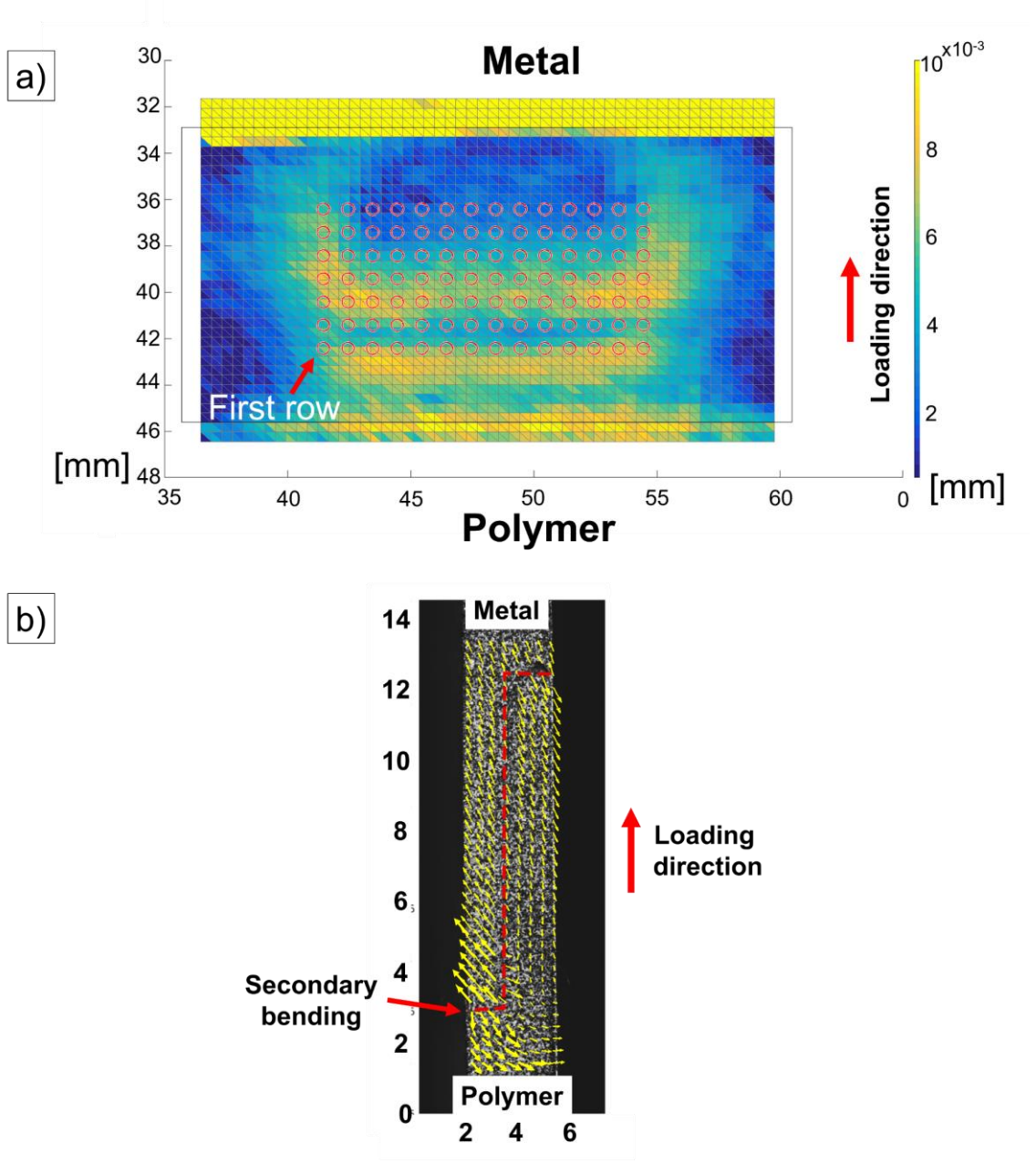

Figure 4.28: Images captured by digital image correlation (DIC) analysis for a PC/AlSi10Mg joint with mushroom-like metal structuring. a) frontal view: the maximum principal deformation at load level of 1 kN. On the displacement composition, a schematic depicting the position of the mushroom-like structures is superimposed; b) lateral view: Quiver diagram of displacement direction showing a secondary bending in the polymer side.

4.2.4 Fatigue behavior of PC/AlSi10Mg joints

PC/AlSi10Mg hybrid joints with mushroom-like metal structuring were subjected to fatigue testing at 4 loading levels: 30%, 40%, 50% and 70% of the ULSF following the same procedure adopted for the PC/AA6061 hybrid joints and described in Section 3.14 Fatigue testing. The resulting S-N curve is shown in Figure 4.29.

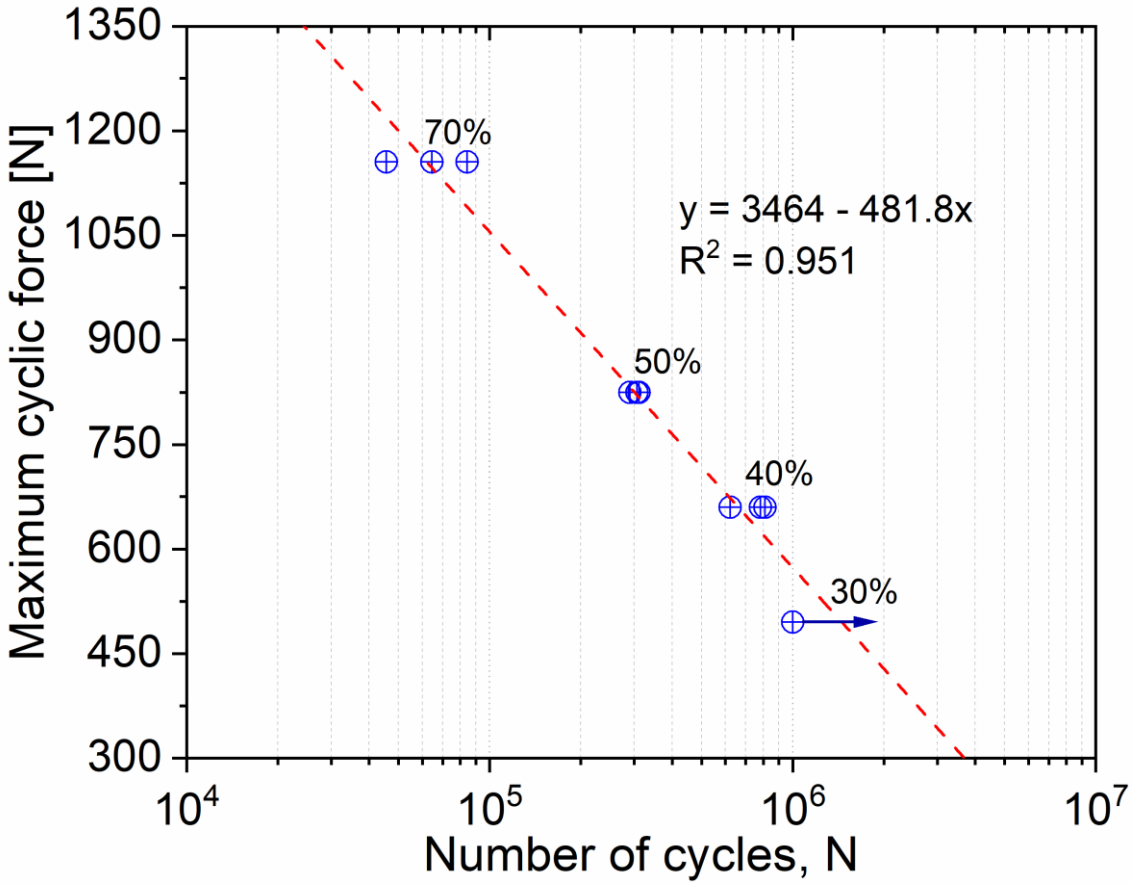

Figure 4.29: Force-life (S-N) curve in tensile mode (R = 0.1) at 5 Hz at load levels of 30%, 40%, 50%, and 70% of the ULSF for PC/AlSi10Mg joints with mushroom-like metal structuring produced in the optimized injection overmolding. The experimental data were fitted by a log-linear (exponential) model (Equation 3.2).

The PC/AlSi10Mg hybrid joints with mushroom-like metal structuring presented distinct failure modes as a function of the loading level in the fatigue test. PC/AlSi10Mg hybrid joints subjected to 70% loading showed mixed failure by delamination, cohesive fracture of the metal pins, and the formation of

transverses cracks in the polymer part near the metal end and in the metal insert near the beginning of the recess (Figure 4.30a). One can also see two distinct fracture zones of metal mushrooms (separated by the dashed red line in Figure 4.30a. The first zone (Figure 4.30a-i) comprehends the central mushrooms except for the first row. The second zone (Figure 4.30a-ii) consists of the contours of the first zone involving part of the first row (near the tip of metal insert).

Figure 4.31a-d shows SEM images of the contour zone (zone (i)) for both metal and polymer sides for the regions demarcated by the red squares in Figure 4.30a. One can see presence of ductile fracture of the mushroom-like structures, which broke at their base, leaving shallow oval holes on the metal surface (Figure 4.31the crack initiation in the base of the fracture mushrooms followed a stable crack propagation (beachmarks) and a final failure (Figure 4.31b) are characteristics of fatigue failure. This suggests a slower crack propagation in this zone [208]. This ductile fracture with slow crack propagation indicates that the interfacial failure of the PC/AlSi10Mg joints with mushroom-like structures originated near the endpoints of the structured area, mainly in the first mushroom row. Possibly at this loading level of 70% of ULSF, the first row undergoes greater deformation, as observed by digital image correlation (DIC) in Figure 4.28, justifying slow crack propagation during each applied loading cycle in the mushroom structures on the first row. Figure 4.32 shows SEM images of the central zone (zone ii) for both metal and polymer side, a magnified view of the region demarcated by the yellow squares in Figure 4.30a, a unique brittle shear fracture is observed. Therefore, after initial ductile fracture of the mushrooms in the contour zone, cracks appear to propagate toward the central zone, whereby the mushrooms fracture rapidly, evidencing a brittle fracture surface.

PC/AlSi10Mg joints subjected to 50% and 40% loads showed brittle fracture in the PC near the first row of the metal pins (Figure 4.30b). PC/AlSi10Mg joints subjected to 30% loading withstood 10^6 cycles without failure, as for the case of PC/AA6061 hybrid joints. The experimental data of the S-N curve were fitted by a log-linear (exponential) expression.

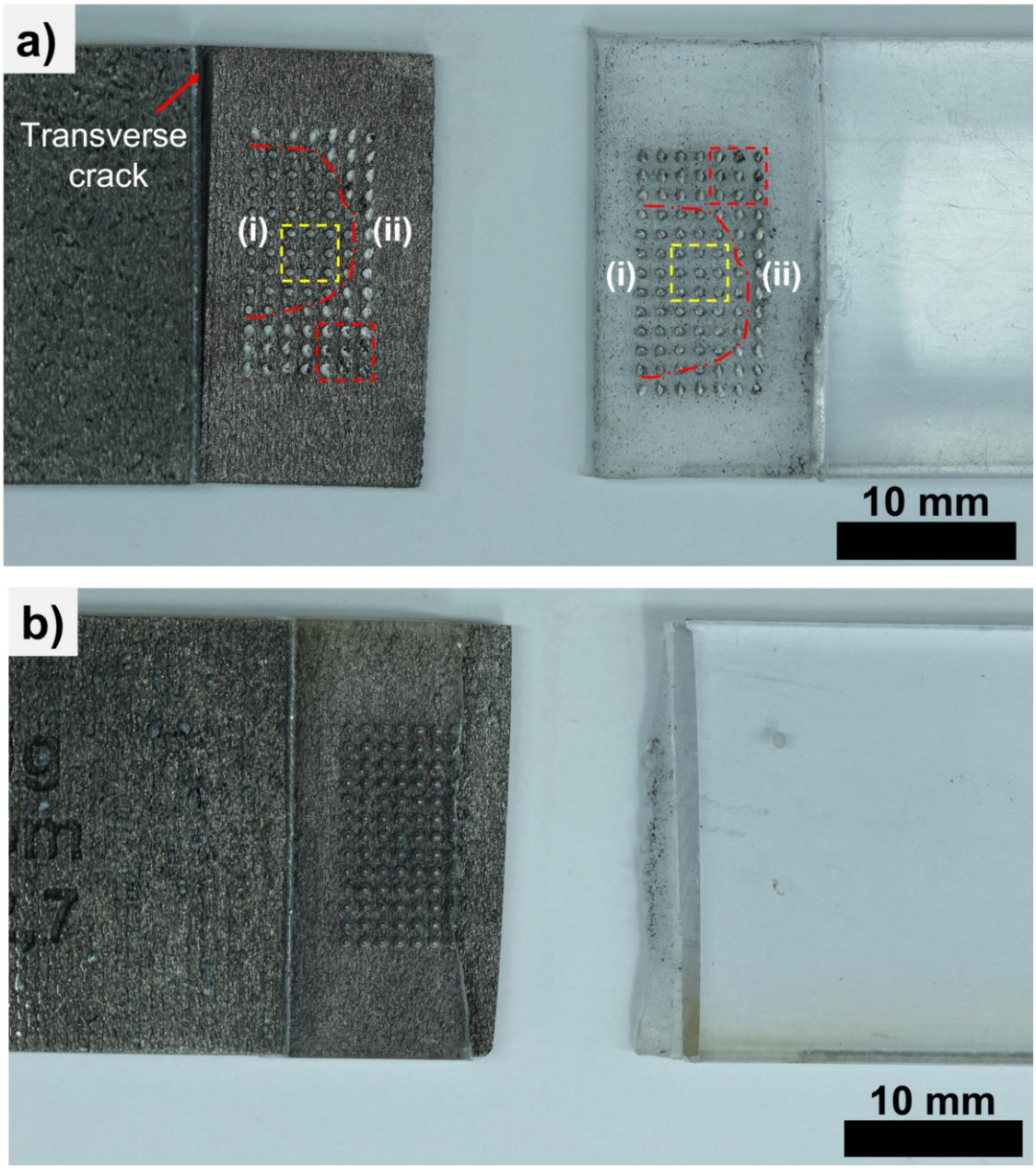

Figure 4.30: Metal (left) and polymer (right) fracture surfaces of PC/AlSi10Mg joints with mushroom-like metal structuring produced in the optimized injection overmolding subjected to fatigue (tensile; R = 0.1; 5 Hz) testing at loading levels of a) 70% (image above), b) 40%-50% (image below) of ULSF.

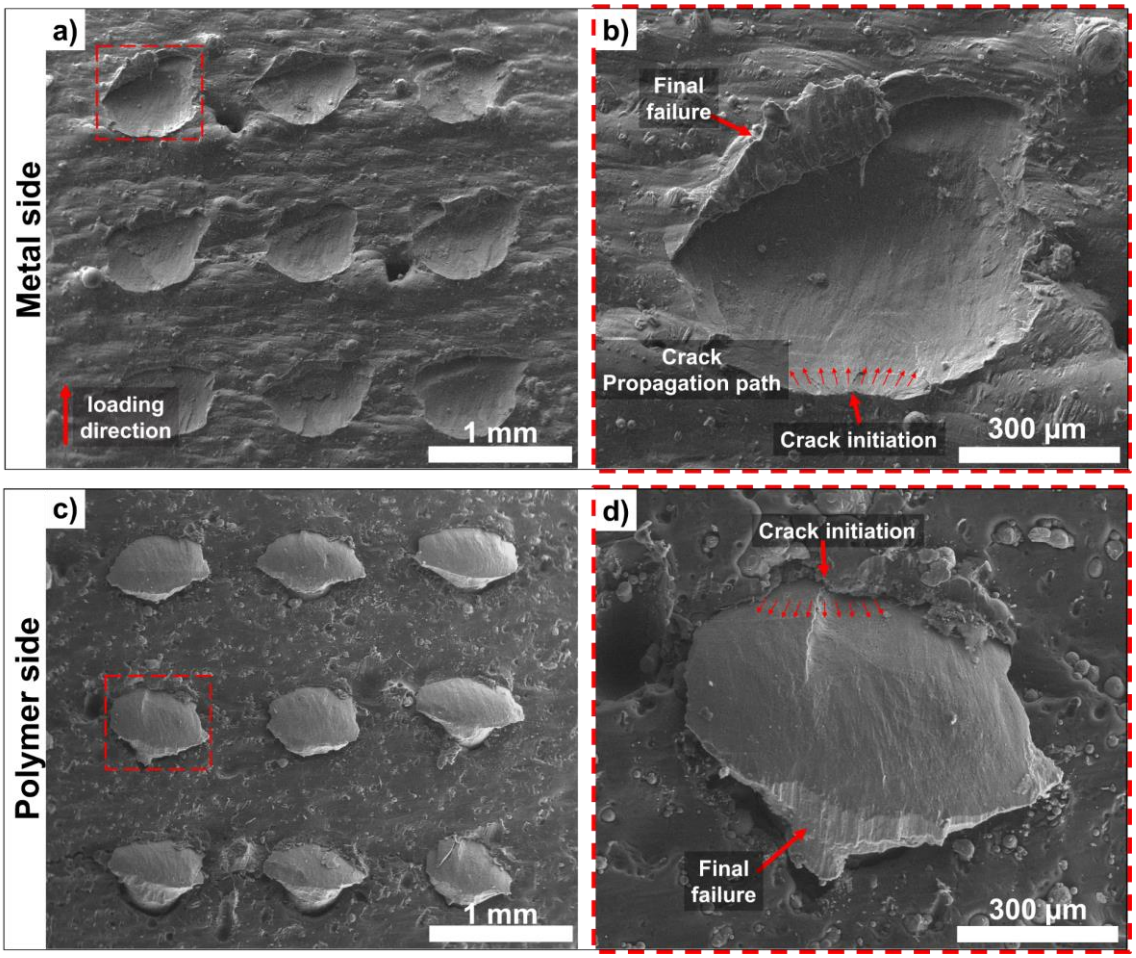

Figure 4.31: Zone (ii) showed in Figure 4.30 of the fracture surface of a PC/AlSi10Mg joint with mushroom-like structuring after fatigue testing at 70% of ULSF. Low (a) and high (b) magnifications of the fracture surface of the base of mushroom-like structures on the metal part; low (c) and high (d) magnifications of the fracture surface of the polymer part showing the base of mushroom-like structures ruptured and attached to the polymer part.

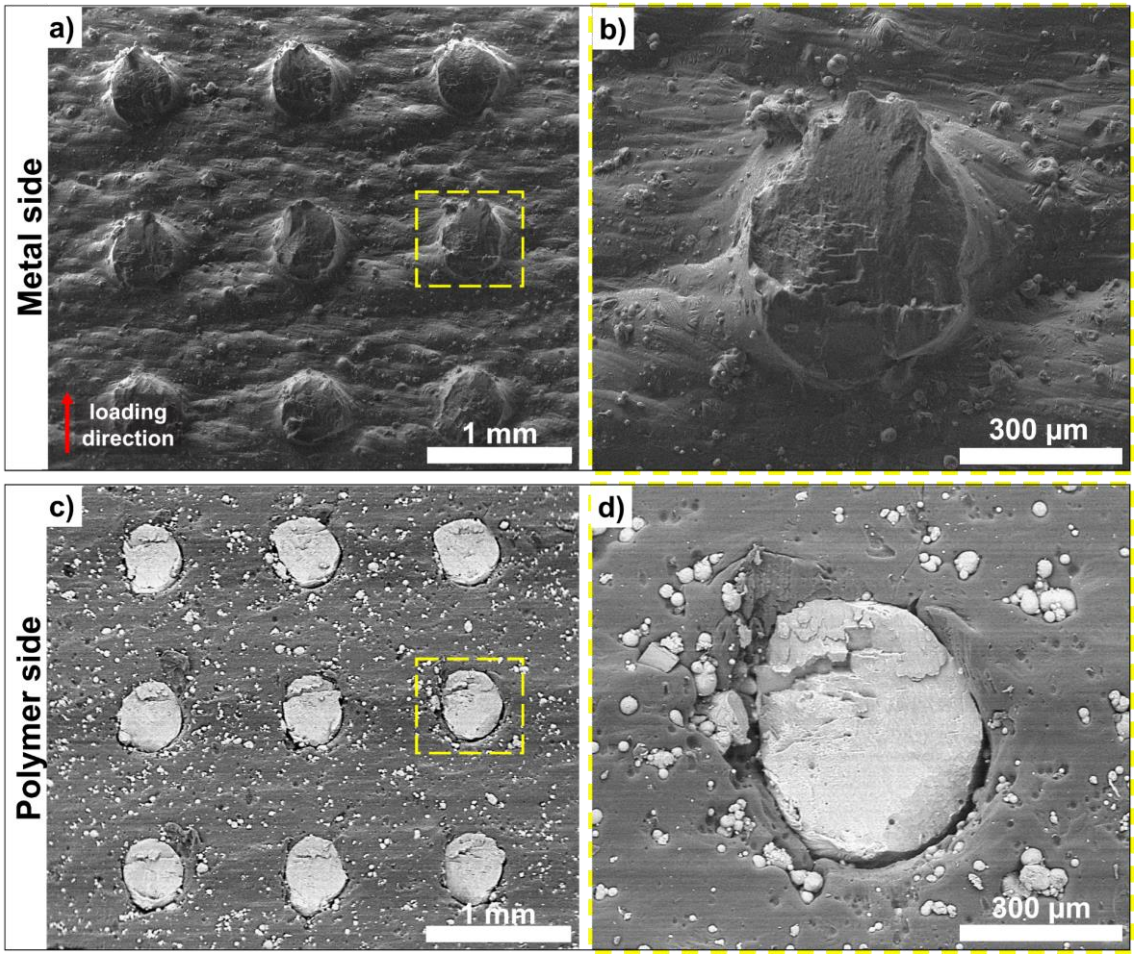

Figure 4.32: SEM images of the zone (i) of the fracture surface of a PC/AlSi10Mg joint with mushroom-like structuring after fatigue testing with 70% loading. Low (a) and high (b) magnifications of the fracture surface of the base of mushroom-like structures on the metal side; Low (c) and high (d) magnifications of the fracture surface of the base of mushroom-like structures on the polymer side.

The run-out PC/AlSi10Mg hybrid joints subjected to fatigue testing at 30% ULSF were subjected to quasi-static lap-shear testing to evaluate residual lap-shear strength. Results revealed a 93% residual joining strength, as shown in Table 4.5. This suggests that the endurance limit of the PC/AlSi10Mg joints is close to 30% of the ULSF, similar to that observed for the PC/AA6061 joints (Figure 4.14).

Table 4.5: Ultimate lap-shear force (ULSF) of run-out PC/AlSi10Mg hybrid joints with mushroom-like structuring.

PC/AlSi10Mg	**ULSF [N]**
Before fatigue testing	1610 ± 60
After 10^6 fatigue cycles	1495 ± 54

5. CONCLUSIONS

In this study, hybrid joints of polycarbonate (PC) and aluminum alloys AA6061 and AlSi10Mg were manufactured by injection overmolding, followed by an in-depth study on processing conditions, adhesion mechanisms, short and long-term mechanical strengths and hygrothermal stability.

In the first part, injection-overmolded PC/AA606 joints with laser-textured metal inserts machined from rolled sheets were produced and characterized. Using design of experiments (DoE) and analysis of variance (ANOVA), it was shown that the injection overmolding parameters barrel temperature, holding pressure and injection speed played positive effects on the filling degree of polymer into the laser-textured grooves on the metal surface, which direct contributed to the lap-shear strength of the joints. Under optimized injection overmolding conditions – barrel temperature 330 °C, holding pressure 1000 bar, injection speed 80 cm^3/s (with mold temperature fixed at 110 °C) – joints reached ultimate lap-shear force (ULSF) of 2.249 N ± 53 N (overlap area of 12.7 mm x 24.8 mm) thus proving a lap-shear strength of 7.2 ± 0.5 MPa, which is comparable to the shear strength of other related joints shown in the literature. PC/AA6061 joints exhibited mixed (adhesive and cohesive) failure with pull-out of the grooves at the metal end on the polymer side. Digital image correlation (DIC) analysis revealed out-of-plane forces in the joint causing secondary bending on the polymeric side. PC/AA6061 joints showed excellent mechanical durability in fatigue tests withstanding 10^6 cycles at 30% ULSF, indicating the endurance limit is close to this, with residual ULSF of 1315 ± 285 N. Also, PC/AA6061 joints exhibited excellent hygrothermal stability after aging at 80 ^oC during 30 days, with residual ULSF of 2236 ± 253 N. Additional studies on hygrothermal aged PC specimens suggested two competing mechanisms - water absorption and physical aging - that appear to balance stiffness and strength of the polymer while reducing ductility, with no significant effect on the joining strength.

In the second part, injection-overmolded PC/AlSi10Mg joints with additive manufactured metal inserts were produced and characterized. DoE and ANOVA analysis revealed that laser powder bed fusion (L-PBF) printing conditions, laser power and hatching distance had a positive impact on the relative density of

printed parts and other factors (layer height, scan speed, and laser spot diameter) showed negative impact. On optimized L-PBF conditions - laser power 240 W, layer height 20 µm, laser scan speed 750 mm/s, laser spot diameter 60 µm and hatching distance 120 µm - parts with relative density of 98% were produced. Following, submillimetrical mushroom, inkpot and lattice shaped structures were printed on the metal surface to provide anchoring with the polymer part. The leaning angle between the printed part with submillimetrical pattern on the surface and the laser beam proved crucial for achieving a smoother surface. Two roughness plateaus were found, the first between 0° and 45° with an average roughness of 20 µm and the second between 50° and 90° with an average roughness of 35 µm. PC/AlSi10Mg joints manufactured with optimal injection parameters attained ULSF values of 1400 N ± 230 N and 1613 N ± 303 N, respectively, for metal inserts containing lattice and mushroom structures on the surface. Considering a structured area of 6.35 mm x 12.4 mm, the lap-shear strength for these joints were, respectively, 17.8 MPa ± 2.9 MPa and 20.5 MPa ± 3.8 MPa. These are above-average when compared with other injection overmolded polymer-metal joints with metal inserts structured with other techniques. In addition, a significant effect of secondary bending on the polymeric side was observed DIC analysis. Furthermore, an endurance limit close to 30% ULSF (samples withstand 10^6 cycles with residual ULSF of 1495 $\pm$ 54 N) was identified in dynamic fatigue testing for PC/AlSi10Mg with mushroom-like structures on the metal surface. Additive manufacturing shows high potential for structuring complex shapes on micrometric scales on the metal surface to increase polymer-metal adhesion. This sort of structure with a high level of complexity can be a viable choice for future applications in industries that employ additive manufacturing to produce metal inserts with subsequent hybridization with polymers.

6. SUGGESTIONS FOR FUTURE STUDIES

This Ph.D. dissertation enabled the manufacturing and optimization of PC-aluminum alloys injection-molded hybrid joints with excellent joining strength. Moreover, it contributed to the knowledge of the mechanical behavior of hybrid joints with direct-adhesion when subjected to cyclic load, a scarce topic in the literature. Furthermore, for the first time, the hygrothermal aging of polymer-metal hybrid joints produced with injection overmolding was investigated, as well as the use of 3D printed aluminum substrates with submillimeter-scale pattern of the surface under lap-shear tests. However, this work dealt with a complex system of different material classes and topics and the following future investigations are needed:

- A comprehensive examination of the effects of laser texturing on the microstructure of the surface of AA6061 component should be conducted.
- AA6061 inserts with deeper grooves and smaller textured area should be employed in order to estimate the maximum joining strength of the PC/AA6061 joint.
- Use dynamic mechanical analysis (DMA) for the determination of the glass transition temperature (T_g) of PC samples before and after hygrothermal aging.
- Use nanohardness on the polymer side of PC/AA6061 joints and DIC testing for the joints after hygrothermal aging tests to investigate the phenomena involving changes in polymer stiffness by physical aging and release of residual stresses.
- Apply finite element analysis (FEA) to support the understanding of the mechanical behavior of injection overmolded hybrid joints.
- Finite element modeling and topology optimization of the texturing profile patterns on the micrometric/submillimeter scale to further improve the quasi-static and cyclic mechanical performance of L-PBF/Polymer hybrid joints.

7. REFERENCES

[1] S.T. Amancio Filho, L.-A. Blaga, eds., Joining of Polymer-Metal Hybrid Structures: Principles and Applications, Wiley, 2018.

[2] F. Lambiase, S.I. Scipioni, C.J. Lee, D.C. Ko, F. Liu, A state-of-the-art review on advanced joining processes for metal-composite and metal-polymer hybrid structures, Materials. 14 (2021). https://doi.org/10.3390/ma14081890.

[3] M.L. Green, L. Espinal, E. Traversa, E.J. Amis, Materials for sustainable development, MRS Bull. 37 (2012) 303–308. https://doi.org/10.1557/mrs.2012.51.

[4] I. Carvalho, O carro do futuro será feito de… plástico?, (2016). https://quatrorodas.abril.com.br/noticias/o-carro-do-futuro-sera-feito-de-plastico/ (accessed May 25, 2018).

[5] R.P. Verma, M. Kumar Lila, A short review on aluminium alloys and welding in structural applications, Mater Today Proc. 46 (2021) 10687–10691. https://doi.org/10.1016/j.matpr.2021.01.447.

[6] M. Authors, Volume 2: Properties and Selection: Nonferrous Alloys and Special-Purpose Materials, 2nd ed., ASM International, United States of America, n.d.

[7] E. Ghio, E. Cerri, Additive Manufacturing of AlSi10Mg and Ti6Al4V Lightweight Alloys via Laser Powder Bed Fusion: A Review of Heat Treatments Effects, Materials. 15 (2022). https://doi.org/10.3390/ma15062047.

[8] F. Lambiase, V. Grossi, A. Paoletti, High-speed joining of hybrid metal-polymer joints during the friction-assisted joining process, Compos Struct. 280 (2022) 114890. https://doi.org/10.1016/j.compstruct.2021.114890.

[9] F. Lambiase, F. Balle, L.A. Blaga, F. Liu, S.T. Amancio-Filho, Friction-based processes for hybrid multi-material joining, Compos Struct. 266 (2021) 113828. https://doi.org/10.1016/j.compstruct.2021.113828.

[10] E.E. Feistauer, J.F. dos Santos, S.T. Amancio-Filho, An investigation of the ultrasonic joining process parameters effect on the mechanical properties

of metal-composite hybrid joints, Welding in the World. 64 (2020) 1481–1495. https://doi.org/10.1007/s40194-020-00927-x.

[11] N.Z. Borba, L. Blaga, J.F. dos Santos, L.B. Canto, S. de T. Amancio-Filho, Influence of rotational speed on the microstructure and mechanical performance of friction-riveted thermosetting composite joints, Welding International. 32 (2018) 11–21. https://doi.org/10.1080/09507116.2017.1347321.

[12] N.M. André, S.M. Goushegir, J.F. dos Santos, L.B. Canto, S.T. Amancio-Filho, Influence of the interlayer film thickness on the mechanical performance of AA2024-T3/CF-PPS hybrid joints produced by friction spot joining, Welding International. 32 (2018) 1–10. https://doi.org/10.1080/09507116.2017.1347319.

[13] R. Sankaranarayanan, N.R.J. Hynes, D. Li, A. Chrysanthou, S.T. Amancio-Filho, Review of Research on Friction Riveting of Polymer/Metal Light Weight Multi-material Structures, Transactions of the Indian Institute of Metals. 74 (2021) 2541–2553. https://doi.org/10.1007/s12666-021-02356-w.

[14] E. Rodríguez-Vidal, C. Sanz, J. Lambarri, I. Quintana, Experimental investigation into metal micro-patterning by laser on polymer-metal hybrid joining, 104 (2018) 73–82. https://doi.org/10.1016/j.optlastec.2018.02.003.

[15] R. Falck, S.M. Goushegir, J.F. dos Santos, S.T. Amancio-Filho, AddJoining: A novel additive manufacturing approach for layered metal-polymer hybrid structures, Mater Lett. 217 (2018) 211–214. https://doi.org/10.1016/j.matlet.2018.01.021.

[16] G.H.M. Oliveira, C. Belei, W.S. de Carvalho, L.B. Canto, S.T. Amancio-Filho, On the fully additive manufacturing of PC/AlSi10Mg hybrid structures, Mater Lett. 330 (2023) 133378. https://doi.org/10.1016/j.matlet.2022.133378.

[17] H. Paul, M. Luke, F. Henning, Combining mechanical interlocking, force fit and direct adhesion in polymer-metal-hybrid structures - Evaluation of the deformation and damage behavior, Compos B Eng. 73 (2015) 158–165. https://doi.org/10.1016/j.compositesb.2014.12.013.

[18] S.T. Amancio-Filho, J.F. dos Santos, Joining of polymers and polymer-metal hybrid structures: Recent developments and trends, Polym Eng Sci. 49 (2009) 1461–1476. https://doi.org/10.1002/pen.21424.

[19] Sergio De Traglia Amancio FilhoJorge F. Dos SantosMatthias Beyer, Method and device for connecting a plastic workpiece to a further workpiece, US8025827B2, 2010.

[20] Sergio De Traglia Amancio FilhoJorge F. Dos SantosAndré Bastos Abibe, Method for joining metal and plastic workpieces, US8567032B2, 2011.

[21] Sergio De Traglia Amancio FilhoJorge F. Dos SantosAndré Bastos Abibe, Method for connecting a plastic workpiece to a further workpiece, US8518198B2, 2012.

[22] André Bastos AbibeSergio De Traglia Amancio FilhoMarilia SônegoJorge Fernandez dos Santos, Method for joining a plastic workpiece to a further workplace, US9925720B2, 2015.

[23] S.T. Amancio-Filho, C. Bueno, J.F. dos Santos, N. Huber, E. Hage, On the feasibility of friction spot joining in magnesium/fiber-reinforced polymer composite hybrid structures, Materials Science and Engineering A. 528 (2011) 3841–3848. https://doi.org/10.1016/j.msea.2011.01.085.

[24] S.M. Goushegir, J.F. dos Santos, S.T. Amancio-Filho, Friction Spot Joining of aluminum AA2024/carbon-fiber reinforced poly(phenylene sulfide) composite single lap joints: Microstructure and mechanical performance, Mater Des. 54 (2014) 196–206. https://doi.org/10.1016/j.matdes.2013.08.034.

[25] N.M. André, J.F. dos Santos, S.T. Amancio-Filho, Evaluation of joint formation and mechanical performance of the AA7075-T6/CFRP spot joints produced by frictional heat, Materials. 16 (2019). https://doi.org/10.3390/ma12060891.

[26] N.M. André, S.M. Goushegir, J.F. dos Santos, L.B. Canto, S.T. Amancio-Filho, Friction Spot Joining of aluminum alloy 2024-T3 and carbon-fiber-reinforced poly(phenylene sulfide) laminate with additional PPS film interlayer: Microstructure, mechanical strength and failure mechanisms,

Compos B Eng. 94 (2016) 197–208. https://doi.org/10.1016/j.compositesb.2016.03.011.

[27] S.M. Goushegir, J.F. dos Santos, S.T. Amancio-Filho, Influence of process parameters on mechanical performance and bonding area of AA2024/carbon-fiber-reinforced poly(phenylene sulfide) friction spot single lap joints, Mater Des. 83 (2015) 431–442. https://doi.org/10.1016/j.matdes.2015.06.044.

[28] J. v. Esteves, S.M. Goushegir, J.F. dos Santos, L.B. Canto, E. Hage, S.T. Amancio-Filho, Friction spot joining of aluminum AA6181-T4 and carbon fiber-reinforced poly(phenylene sulfide): Effects of process parameters on the microstructure and mechanical strength, Mater Des. 66 (2015) 437–445. https://doi.org/10.1016/j.matdes.2014.06.070.

[29] C.F. Rodrigues, L.A. Blaga, J.F. dos Santos, L.B. Canto, E. Hage, S.T. Amancio-Filho, FricRiveting of aluminum 2024-T351 and polycarbonate: Temperature evolution, microstructure and mechanical performance, J Mater Process Technol. 214 (2014) 2029–2039. https://doi.org/10.1016/j.jmatprotec.2013.12.018.

[30] J. Gonçalves, J.F. dos Santos, L.B. Canto, S.T. Amancio-Filho, Friction spot welding of carbon fiber-reinforced polyamide 66 laminate, Mater Lett. 159 (2015) 506–509. https://doi.org/10.1016/j.matlet.2015.08.036.

[31] L. Blaga, R. Bancilă, J.F. dos Santos, S.T. Amancio-Filho, Friction Riveting of glass-fibre-reinforced polyetherimide composite and titanium grade 2 hybrid joints, Mater Des. 50 (2013) 825–829. https://doi.org/10.1016/j.matdes.2013.03.061.

[32] A.B. Abibe, M. Sônego, J.F. dos Santos, L.B. Canto, S.T. Amancio-Filho, On the feasibility of a friction-based staking joining method for polymer-metal hybrid structures, Mater Des. 92 (2016) 632–642. https://doi.org/10.1016/j.matdes.2015.12.087.

[33] W.S. Junior, T. Emmler, C. Abetz, U.A. Handge, J.F. dos Santos, S.T. Amancio-Filho, V. Abetz, Friction spot welding of PMMA with PMMA/silica and PMMA/silica-g-PMMA nanocomposites functionalized via ATRP,

Polymer (Guildf). 55 (2014) 5146–5159. https://doi.org/10.1016/j.polymer.2014.08.022.

[34] P.H.F. Oliveira, S.T. Amancio-Filho, J.F. dos Santos, E. Hage, Preliminary study on the feasibility of friction spot welding in PMMA, Mater Lett. 64 (2010) 2098–2101. https://doi.org/10.1016/j.matlet.2010.06.050.

[35] J. Altmeyer, U.F.H. Suhuddin, J.F. dos Santos, S.T. Amancio-Filho, Microstructure and mechanical performance of metal-composite hybrid joints produced by FricRiveting, Compos B Eng. 81 (2015) 130–140. https://doi.org/10.1016/j.compositesb.2015.06.015.

[36] J. Altmeyer, J.F. dos Santos, S.T. Amancio-Filho, Effect of the friction riveting process parameters on the joint formation and performance of Ti alloy/short-fibre reinforced polyether ether ketone joints, Mater Des. 60 (2014) 164–176. https://doi.org/10.1016/j.matdes.2014.03.042.

[37] E. Rodríguez-vidal, C. Sanz, C. Soriano, J. Leunda, G. Verhaeghe, Effect of metal micro-structuring on the mechanical behavior of polymer – metal laser T-joints, Journal of Materials Processing Tech. 229 (2016) 668–677. https://doi.org/10.1016/j.jmatprotec.2015.10.026.

[38] J.P. Bergmann, M. Stambke, Potential of laser-manufactured polymer-metal hybrid joints, 39 (2012) 84–91. https://doi.org/10.1016/j.phpro.2012.10.017.

[39] Sergio De Traglia Amancio FilhoEduardo ETZBERGER FEISTAUERJorge Fernandez Dos Santos, United States METHOD FOR CONNECTING A SURFACE-STRUCTURED WORKPIECE AND, US009925717B2, 2018.

[40] F. Balle, G. Wagner, D. Eifler, Ultrasonic metal welding of aluminium sheets to carbon fibre reinforced thermoplastic composites, Adv Eng Mater. 11 (2009) 35–39. https://doi.org/10.1002/adem.200800271.

[41] F. Balle, G. Wagner, D. Eifler, Ultrasonic spot welding of aluminum sheet/ carbon fiber reinforced polymer - Joints, Materwiss Werksttech. 38 (2007) 934–938. https://doi.org/10.1002/mawe.200700212.

[42] U.F. Dal Conte, I. F Villegas, J. Tachon, Ultrasonic plastic welding of CF/PA6 composites to aluminium: Process and mechanical performance

of welded joints, J Compos Mater. 53 (2019) 2607–2621. https://doi.org/10.1177/0021998319836022.

[43] W.S. de Carvalho, N.F. Colvin, A. Benatar, S.T. Amancio-Filho, Ultrasonic Joining of Additively Manufactured Metal-Composite Hybrid Joints: A Comparison between Vertical and Horizontal Vibration Modes, Metals (Basel). 13 (2023) 319. https://doi.org/10.3390/met13020319.

[44] B. Pereira, W.S. de Carvalho, N.F. Colvin, A. Benatar, S.T. Amancio-Filho, metals Ultrasonic Joining of Additively Manufactured Metal-Composite Hybrid Joints: A Comparison between Vertical and Horizontal Vibration Modes, (2023). https://doi.org/10.3390/met13020319.

[45] W.S. de Carvalho, S.T. Amancio-Filho, On the Feasibility of Joining Additively-Manufactured 316l Stainless Steel and Poly-Ether-Ether-Ketone by Ultrasonic Energy, SSRN Electronic Journal. 3 (2022) 100098. https://doi.org/10.2139/ssrn.4171664.

[46] R. Falck, J.F. dos Santos, S.T. Amancio-Filho, Microstructure and mechanical performance of additively manufactured aluminum 2024-t3/acrylonitrile butadiene styrene hybrid joints using an addjoining technique, Materials. 16 (2019). https://doi.org/10.3390/ma12060864.

[47] C. Belei, R. Pommer, S.T. Amancio-Filho, Optimization of additive manufacturing for the production of short carbon fiber-reinforced polyamide/Ti-6Al-4V hybrid parts, Mater Des. 219 (2022). https://doi.org/10.1016/j.matdes.2022.110776.

[48] M. Grujicic, V. Sellappan, G. Arakere, N. Seyr, A. Obieglo, M. Erdmann, J. Holzleitner, The potential of a clinch-lock polymer metal hybrid technology for use in load-bearing automotive components, J Mater Eng Perform. 18 (2009) 893–902. https://doi.org/10.1007/s11665-008-9325-2.

[49] M. Grujicic, Injection over molding of polymer-metal hybrid structures, American Journal of Science and Technology. 1 (2014) 168–181. https://doi.org/10.4271/980708.

[50] F. Kimura, S. Kadoya, Y. Kajihara, Effects of molding conditions on injection molded direct joining using a metal with nano-structured surface,

Precis Eng. 45 (2016) 203–208. https://doi.org/10.1016/j.precisioneng.2016.02.013.

[51] T. Temesi, T. Czigany, Integrated Structures from Dissimilar Materials: The Future Belongs to Aluminum–Polymer Joints, Adv Eng Mater. 22 (2020). https://doi.org/10.1002/adem.202000007.

[52] R.H., B.D.J., B.D.M. and H.L.R.J. Dahm, Adhesives 4, Applied Science Pub., London, 1979. https://doi.org/10.1179/sic.1984.29.Supplement-1.5.

[53] G. Lucchetta, F. Marinello, P.F. Bariani, Aluminum sheet surface roughness correlation with adhesion in polymer metal hybrid overmolding, CIRP Ann Manuf Technol. 60 (2011) 559–562. https://doi.org/10.1016/j.cirp.2011.03.073.

[54] X. Li, D. Xu, N. Gong, Z. Xu, L. Wang, W. Dong, Improving the strength of injection molded aluminum/polyphenylene sulfide lap joints dependence on surface microstructure and composition, Mater Des. 179 (2019) 107875. https://doi.org/10.1016/j.matdes.2019.107875.

[55] N. Gong, B. Wang, Y. Wang, X. Li, W. Lin, S. Fu, X. Chu, Effect of metal surface state on injection joining strength of aluminum-rubber composite part, J Manuf Process. 49 (2020) 365–372. https://doi.org/10.1016/j.jmapro.2019.12.006.

[56] S. Kadoya, F. Kimura, Y. Kajihara, PBT–anodized aluminum alloy direct joining: Characteristic injection speed dependence of injected polymer replicated into nanostructures, Polym Test. 75 (2019) 127–132. https://doi.org/10.1016/j.polymertesting.2019.02.006.

[57] F.C. Liu, P. Dong, W. Lu, K. Sun, On formation of Al–O–C bonds at aluminum/polyamide joint interface, Appl Surf Sci. 466 (2019) 202–209. https://doi.org/10.1016/j.apsusc.2018.10.024.

[58] S.M. Goushegir, N. Scharnagl, J.F. dos Santos, S.T. Amancio-Filho, XPS analysis of the interface between AA2024-T3/CF-PPS friction spot joints, in: Surface and Interface Analysis, John Wiley and Sons Ltd, 2016: pp. 706–711. https://doi.org/10.1002/sia.5816.

[59] J. Friedrich, Metal-Polymer Systems: Interface Design and Chemical Bonding, Wiley-VCH, 2018, Erkner, Germany, n.d.

[60] A. Baldan, Adhesion phenomena in bonded joints, Int J Adhes Adhes. 38 (2012) 95–116. https://doi.org/10.1016/j.ijadhadh.2012.04.007.

[61] A.J. Kinloch, Adhesion and Adhesives, Springer Netherlands, Dordrecht, 1987. https://doi.org/10.1007/978-94-015-7764-9.

[62] X. Li, N. Gong, C. Yang, S. Zeng, S. Fu, K. Zhang, Aluminum/polypropylene composites produced through injection molding, J Mater Process Technol. 255 (2018) 635–643. https://doi.org/10.1016/j.jmatprotec.2018.01.008.

[63] P.C. Pandey, S. Narasimhan, Three-dimensional nonlinear analysis of adhesively bonded lap joints considering viscoplasticity in adhesives, Comput Struct. 79 (2001) 769–783. https://doi.org/10.1016/S0045-7949(00)00160-7.

[64] L. Zhao, A. Xin, F. Liu, J. Zhang, N. Hu, Secondary bending effects in progressively damaged single-lap, single-bolt composite joints, Results Phys. 6 (2016) 704–711. https://doi.org/10.1016/j.rinp.2016.08.021.

[65] S. Ebnesajjad, A.H. Landrock, Joint Design, Adhesives Technology Handbook. (2015) 183–205. https://doi.org/10.1016/b978-0-323-35595-7.00007-3.

[66] J. Shields, Adhesives Handbook, 1984. https://doi.org/10.1016/c2013-0-06270-6.

[67] L.F.M. da Silva, P.J.C. das Neves, R.D. Adams, A. Wang, J.K. Spelt, Analytical models of adhesively bonded joints—Part II: Comparative study, Int J Adhes Adhes. 29 (2009) 331–341. https://doi.org/10.1016/j.ijadhadh.2008.06.007.

[68] J.W. Renton, J.R. Vinson, On the behavior of bonded joints in composite material structures, Eng Fract Mech. 7 (1975) 41–60. https://doi.org/10.1016/0013-7944(75)90065-X.

[69] J.-H. Kweon, J.-W. Jung, T.-H. Kim, J.-H. Choi, D.-H. Kim, Failure of carbon composite-to-aluminum joints with combined mechanical fastening and adhesive bonding, Compos Struct. 75 (2006) 192–198. https://doi.org/10.1016/j.compstruct.2006.04.013.

[70] S. Ebnesajjad, A.H. Landrock, Adhesives for Medical and Dental Applications, 2015. https://doi.org/10.1016/b978-0-323-35595-7.00010-3.

[71] W.J. Renton, J.R. Vinson, The Efficient Design of Adhesive Bonded Joints, J Adhes. 7 (1975) 175–193. https://doi.org/10.1080/00218467508075049.

[72] American Society for Testing and Materials, Standard Test Method for Bearing Response of Polymer Matrix Composite Laminates - D5961, (2017).

[73] A.B. Abibe, S.T. Amancio-Filho, J.F. dos Santos, E. Hage, Mechanical and failure behaviour of hybrid polymer–metal staked joints, Materials & Design . 46 (2013) 338–347. https://doi.org/10.1016/j.matdes.2012.10.043.

[74] R. Jones, A.J. Kinloch, J.G. Michopoulos, A.J. Brunner, N. Phan, Delamination growth in polymer-matrix fibre composites and the use of fracture mechanics data for material characterisation and life prediction, Compos Struct. 180 (2017) 316–333. https://doi.org/10.1016/j.compstruct.2017.07.097.

[75] K.L. Rugg, B.N. Cox, R. Massabò, Mixed mode delamination of polymer composite laminates reinforced through the thickness by z-fibers, Compos Part A Appl Sci Manuf. 33 (2002) 177–190. https://doi.org/10.1016/S1359-835X(01)00109-9.

[76] R.L. Vasconcelos, G.H.M. Oliveira, S.T. Amancio-Filho, L.B. Canto, Injection overmolding of polymer-metal hybrid structures: A review, Polym Eng Sci. (2023). https://doi.org/10.1002/pen.26244.

[77] H. Fettig, J. Wylde, T. Hubbard, M. Kujath, Simulation, dynamic testing and design of micromachined flexible joints, Journal of Micromechanics and Microengineering. 11 (2001) 209–216. https://doi.org/10.1088/0960-1317/11/3/308.

[78] X. Li, F. Liu, N. Gong, P. Huang, C. Yang, Enhancing the joining strength of injection-molded polymer-metal hybrids by rapid heating and cooling, J Mater Process Technol. 249 (2017) 386–393. https://doi.org/10.1016/j.jmatprotec.2017.06.034.

[79] X. Li, F. Liu, N. Gong, C. Yang, B. Wang, Surface topography induced high injection joining strength of polymer-metal composite and fracture mechanism, Compos Struct. 184 (2018) 545–553. https://doi.org/10.1016/j.compstruct.2017.10.020.

[80] J. Byskov-Nielsen, J. v. Boll, A.H. Holm, R. Højsholt, P. Balling, Ultra-high-strength micro-mechanical interlocking by injection molding into laser-structured surfaces, Int J Adhes Adhes. 30 (2010) 485–488. https://doi.org/10.1016/j.ijadhadh.2010.03.008.

[81] J. Gebauer, M. Fischer, A.F. Lasagni, I. Kühnert, A. Klotzbach, Laser structured surfaces for metal-plastic hybrid joined by injection molding, J Laser Appl. 30 (2018) 032021. https://doi.org/10.2351/1.5036803.

[82] K. Enami, F. Kimura, K. Yokoyama, T. Murakami, Y. Kajihara, Experimental and simulative investigation of the effects of laser-structured metal surface on metal-polymer direct joining, Precis Eng. 62 (2020) 273–281. https://doi.org/10.1016/j.precisioneng.2019.12.011.

[83] S. Zhao, A. Takeuchi, F. Kimura, Y. Kajihara, Experimental investigation of the anchoring effect of aluminum/amorphous-plastics joints fabricated by injection molded direct joining, Precis Eng. 77 (2022) 320–327. https://doi.org/10.1016/j.precisioneng.2022.06.013.

[84] S. Zhao, F. Kimura, S. Kadoya, Y. Kajihara, Experimental analysis on mechanical interlocking of metal–polymer direct joining, Precis Eng. 61 (2020) 120–125. https://doi.org/10.1016/j.precisioneng.2019.10.009.

[85] R. Xu, Y. Xie, R. Li, J. Zhang, T. Zhou, Direct Bonding of Polymer and Metal with an Ultrahigh Strength: Laser Treatment and Mechanical Interlocking, Adv Eng Mater. 23 (2021) 1–11. https://doi.org/10.1002/adem.202001288.

[86] P.A. Fabrin, M.E. Hoikkanen, J.E. Vuorinen, Adhesion of thermoplastic elastomer on surface treated aluminum by injection molding, Polym Eng Sci. 47 (2007) 1187–1191. https://doi.org/10.1002/pen.20801.

[87] F. Kimura, S. Kadoya, Y. Kajihara, Effects of molding conditions on injection molded direct joining under various surface fine-structuring, International Journal of Advanced Manufacturing Technology. 101 (2019) 2703–2712. https://doi.org/10.1007/s00170-018-3154-8.

[88] R.Y. Yeh, R.Q. Hsu, Improving the adhesion of plastic/metal direct bonding by injection moulding using surface modifications, Advances in Materials and Processing Technologies. 2 (2016) 21–30. https://doi.org/10.1080/2374068X.2016.1147765.

[89] F. Kimura, E. Yamaguchi, N. Horie, G. Suzuki, Y. Kajihara, Formation of boehmite crystals on microblasted aluminum surface to enhance performance of metal–polymer direct joining, Mater Lett. 260 (2020) 126963. https://doi.org/10.1016/j.matlet.2019.126963.

[90] S. Zhao, F. Kimura, E. Yamaguchi, N. Horie, Y. Kajihara, Manufacturing aluminum/polybutylene terephthalate direct joints by using hot water–treated aluminum via injection molding, International Journal of Advanced Manufacturing Technology. 107 (2020) 4637–4644. https://doi.org/10.1007/s00170-020-05364-0.

[91] S. Verma, C.K. Yang, C.H. Lin, J.Y. Jeng, Additive manufacturing of lattice structures for high strength mechanical interlocking of metal and resin during injection molding, Addit Manuf. 49 (2022). https://doi.org/10.1016/j.addma.2021.102463.

[92] X. Cao, W. Wallace, C. Poon, J.-P. Immarigeon, Research and Progress in Laser Welding of Wrought Aluminum Alloys. I. Laser Welding Processes, Materials and Manufacturing Processes. 18 (2003) 1–22. https://doi.org/10.1081/AMP-120017586.

[93] O.S. Odebiyi, S.M. Adedayo, L.A. Tunji, M.O. Onuorah, A review of weldability of carbon steel in arc-based welding processes, Cogent Eng. 6 (2019). https://doi.org/10.1080/23311916.2019.1609180.

[94] J. Gandra, H. Krohn, R.M. Miranda, P. Vilaça, L. Quintino, J.F. dos Santos, Friction surfacing—A review, J Mater Process Technol. 214 (2014) 1062–1093. https://doi.org/10.1016/j.jmatprotec.2013.12.008.

[95] S. Selvi, A. Vishvaksenan, E. Rajasekar, Cold metal transfer (CMT) technology - An overview, Defence Technology. 14 (2018) 28–44. https://doi.org/10.1016/j.dt.2017.08.002.

[96] S. Yin, Y. Xie, R. Li, J. Zhang, T. Zhou, Polymer-Metal Hybrid Material with an Ultra-High Interface Strength Based on Mechanical Interlocking via Nanopores Produced by Electrochemistry, Ind Eng Chem Res. 59 (2020) 12409–12420. https://doi.org/10.1021/acs.iecr.0c01304.

[97] R.Y. Yeh, R.Q. Hsu, Application of porous oxide layer in plastic/metal direct adhesion by injection molding, J Adhes Sci Technol. 29 (2015) 1617–1627. https://doi.org/10.1080/01694243.2015.1038955.

[98] S. Bistac, M.F. Vallat, J. Schultz, Durability of steel/polymer adhesion in an aqueous environment, Int J Adhes Adhes. 18 (1998) 365–369. https://doi.org/10.1016/S0143-7496(98)00020-7.

[99] F.J. Boerio, P. Shah, Adhesion of injection molded PVC to steel substrates, Journal of Adhesion. 81 (2005) 645–675. https://doi.org/10.1080/00218460590954656.

[100] M. Honkanen, M. Hoikkanen, M. Vippola, J. Vuorinen, T. Lepistö, Metal-plastic adhesion in injection-molded hybrids, J Adhes Sci Technol. 23 (2009) 1747–1761. https://doi.org/10.1163/016942409X12489445844435.

[101] M. Hoikkanen, M. Honkanen, M. Vippola, T. Lepistö, J. Vuorinen, Effect of silane treatment parameters on the silane layer formation and bonding to thermoplastic urethane, Prog Org Coat. 72 (2011) 716–723. https://doi.org/10.1016/j.porgcoat.2011.08.002.

[102] M. Hoikkanen, M. Honkanen, L. Frisk, M. Vippola, T. Lepistö, J. Vuorinen, Metal-thermoplastic urethane hybrids in environmental exposure, Int J Adhes Adhes. 35 (2012) 21–26. https://doi.org/10.1016/j.ijadhadh.2012.01.024.

[103] Y. Zhang, L. Sun, L. Li, B. Huang, T. Wang, Y. Wang, Direct injection molding and mechanical properties of high strength steel/composite hybrids, Compos Struct. 210 (2019) 70–81. https://doi.org/10.1016/j.compstruct.2018.11.035.

[104] L. Ammosova, K. Mönkkönen, M. Suvanto, Precise fabrication of microtextured stainless steel surfaces using metal injection moulding, Precis Eng. 62 (2020) 89–94. https://doi.org/10.1016/j.precisioneng.2019.11.012.

[105] S. Wurzbacher, S. Gach, U. Reisgen, C. Hopmann, Joining of plastic-metal hybrid components by overmoulding of specially designed form-closure elements, Materwiss Werksttech. 52 (2021) 367–378. https://doi.org/10.1002/mawe.202000158.

[106] D.F.F. John F. Ready, Handbook of laser Materials Processing-Laser, 2001.

[107] A. Samanta, Q. Wang, S.K. Shaw, H. Ding, Nanostructuring of laser textured surface to achieve superhydrophobicity on engineering metal surface, J Laser Appl. 31 (2019) 022515. https://doi.org/10.2351/1.5096148.

[108] A. Klotzbach, M. Langer, Thermal direct joining of metal to fiber reinforced thermoplastic components Thermal direct joining of metal to fiber reinforced thermoplastic components, 022421 (2017). https://doi.org/10.2351/1.4983243.

[109] Y. Pao, Co2 Lasers Effects and Applications, Co2 Lasers Effects and Applications. (1976). https://doi.org/10.1016/b978-0-122-23350-0.x5001-9.

[110] K.T. Voisey, S.S. Kudesia, W.S.O. Rodden, D.P. Hand, J.D.C. Jones, T.W. Clyne, Melt ejection during laser drilling of metals, Materials Science and Engineering A. 356 (2003) 414–424. https://doi.org/10.1016/S0921-5093(03)00155-2.

[111] B. Mao, A. Siddaiah, Y. Liao, P.L. Menezes, Laser surface texturing and related techniques for enhancing tribological performance of engineering materials: A review, J Manuf Process. 53 (2020) 153–173. https://doi.org/10.1016/j.jmapro.2020.02.009.

[112] A. Bharatish, G.R. Rajkumar, P. Gurav, G. Satheesh Babu, H.N. Narasimha Murthy, M. Roy, Optimization of laser texture geometry and resulting functionality of nickel aluminium bronze for landing gear applications, International Journal of Lightweight Materials and Manufacture. 4 (2021) 346–357. https://doi.org/10.1016/j.ijlmm.2021.04.004.

[113] Â. Cunha, F. Bartolomeu, F. Silva, B. Trindade, Ó. Carvalho, Influence of Laser Parameters on the Texturing of 420 Stainless Steel, Materials. 15 (2022) 8979. https://doi.org/10.3390/ma15248979.

[114] A. Samanta, Q. Wang, S.K. Shaw, H. Ding, Nanostructuring of laser textured surface to achieve superhydrophobicity on engineering metal

surface, J Laser Appl. 31 (2019) 022515. https://doi.org/10.2351/1.5096148.

[115] M. Skalon, B. Meier, A. Gruberbauer, S. de T. Amancio-Filho, C. Sommitsch, Stability of a Melt Pool during 3D-Printing of an Unsupported Steel Component and Its Influence on Roughness, Materials. 13 (2020) 808. https://doi.org/10.3390/ma13030808.

[116] A. Yadollahi, N. Shamsaei, S.M. Thompson, A. Elwany, L. Bian, Effects of building orientation and heat treatment on fatigue behavior of selective laser melted 17-4 PH stainless steel, Int J Fatigue. 94 (2017) 218–235. https://doi.org/10.1016/j.ijfatigue.2016.03.014.

[117] J.D. Pérez-Ruiz, F. Marin, S. Martínez, A. Lamikiz, G. Urbikain, L.N. López de Lacalle, Stiffening near-net-shape functional parts of Inconel 718 LPBF considering material anisotropy and subsequent machining issues, Mech Syst Signal Process. 168 (2022) 108675. https://doi.org/10.1016/j.ymssp.2021.108675.

[118] D. Simson, S.K. Subbu, Effect of Process Parameters on Surface Integrity of LPBF Ti6Al4V, Procedia CIRP. 108 (2022) 716–721. https://doi.org/10.1016/j.procir.2022.03.111.

[119] I. Koutiri, E. Pessard, P. Peyre, O. Amlou, T. de Terris, Influence of SLM process parameters on the surface finish, porosity rate and fatigue behavior of as-built Inconel 625 parts, J Mater Process Technol. 255 (2018) 536–546. https://doi.org/10.1016/j.jmatprotec.2017.12.043.

[120] L. Lizzul, M. Sorgato, R. Bertolini, A. Ghiotti, S. Bruschi, Surface finish of additively manufactured Ti6Al4V workpieces after ball end milling, Procedia CIRP. 102 (2021) 228–233. https://doi.org/10.1016/j.procir.2021.09.039.

[121] C. Earl, J.R. Castrejón-Pita, P.A. Hilton, W. O'Neill, The dynamics of laser surface modification, J Manuf Process. 21 (2016) 214–223. https://doi.org/10.1016/j.jmapro.2015.10.002.

[122] Sachin Salunkhe, Sergio T. Amancio-Filho, J. Paulo Davim, eds., Advances in Metal Additive Manufacturing, Elsevier, 2023. https://doi.org/10.1016/C2020-0-03745-X.

[123] L. Minkowitz, S. Arneitz, P.S. Effertz, S.T. Amancio-Filho, Laser–Powder Bed Fusion Process Optimisation of AlSi10Mg Using Extra Trees Regression, Mater Des. (2023) 111718. https://doi.org/10.1016/j.matdes.2023.111718.

[124] F. Calignano, D. Manfredi, E.P. Ambrosio, L. Iuliano, P. Fino, Influence of process parameters on surface roughness of aluminum parts produced by DMLS, International Journal of Advanced Manufacturing Technology. 67 (2013) 2743–2751. https://doi.org/10.1007/s00170-012-4688-9.

[125] V. Gunenthiram, P. Peyre, M. Schneider, M. Dal, F. Coste, R. Fabbro, Analysis of laser–melt pool–powder bed interaction during the selective laser melting of a stainless steel, J Laser Appl. 29 (2017) 022303. https://doi.org/10.2351/1.4983259.

[126] P. Jin, Q. Tang, J. Song, Q. Feng, F. Guo, X. Fan, M. Jin, F. Wang, Numerical investigation of the mechanism of interfacial dynamics of the melt pool and defects during laser powder bed fusion, Opt Laser Technol. 143 (2021) 107289. https://doi.org/10.1016/j.optlastec.2021.107289.

[127] M. Grujicic, Injection Overmolding of Polymer-Metal Hybrid Structures, in: Joining of Polymer-Metal Hybrid Structures, John Wiley & Sons, Inc, Hoboken, NJ, 2017: pp. 277–305. https://doi.org/10.1002/9781119429807.ch10.

[128] Z. Tadmor, C. Gogos, Principles of Polymer Processing, 2nd ed., John Wiley & Sons, Inc., Hoboken, New Jersey, 2006.

[129] M.G.R. Eds: D. V. Rosato, D. V. Rosato, Injection Molding Handbook, Springer Science+Business Media, New York, 2000.

[130] Chang Dae Han, Rheology in Polymer Processing, Oxford University Press, Inc., New York, 2007.

[131] A. v. Shenoy, D.R. Saini, Thermoplastic melt rheology and processing, Marcel Dekker, 1996.

[132] Manfred Rink, Process for producing bonded plastic metal parts, US5842265A, 1996.

[133] M. Grujicic, Joining Processes Based on Direct-Assembly Methods Injection Overmolding of Polymer – Metal Hybrid, (n.d.).

[134] K. Ramani, B. Moriarty, Thermoplastic bonding to metals via injection molding for macro-composite manufacture, Polym Eng Sci. 38 (1998) 870–877. https://doi.org/10.1002/pen.10253.

[135] S.L. Kim, M.Y. Lyu, Adhesive strengths between glass fiber-filled ABS and metal in insert molding with engraved and embossed metal surface treatments, Polym Eng Sci. 59 (2019) E93–E100. https://doi.org/10.1002/pen.24866.

[136] B. Huang, L. Sun, L. Li, L. Zhang, Y. Lin, J. Che, Experimental investigation of the strength of polymer-steel direct adhesion (PSDA) joints with micro-structures ablated by laser, J Mater Process Technol. 249 (2017) 407–414. https://doi.org/10.1016/j.jmatprotec.2017.06.031.

[137] M. Grujicic, V. Sellappan, M.A. Omar, N. Seyr, A. Obieglo, M. Erdmann, J. Holzleitner, An overview of the polymer-to-metal direct-adhesion hybrid technologies for load-bearing automotive components, J Mater Process Technol. 197 (2008) 363–373. https://doi.org/10.1016/j.jmatprotec.2007.06.058.

[138] D. v. Rosato, M.G. Rosato, M.G. Rosato, eds., Injection Molding Handbook, Springer US, Boston, MA, 2000. https://doi.org/10.1007/978-1-4615-4597-2.

[139] M.Y. Lyu, T.G. Choi, Research trends in polymer materials for use in lightweight vehicles, International Journal of Precision Engineering and Manufacturing. 16 (2015) 213–220. https://doi.org/10.1007/s12541-015-0029-x.

[140] E. Commission, Zero emission vehicles: first ‘Fit for 55’’ deal will end the sale of new CO2 emitting cars in Europe by 2035,’ (2022) https://ec.europa.eu/commission/presscorner/detail.

[141] P. Today, Trelleborg becomes first-time WIT user for new plastic brake pedal, (2010). https://www.plasticstoday.com/trelleborg-becomes-first-time-wit-user-new-plastic-brake-pedal (accessed November 9, 2022).

[142] SABIC Basic Industries Corp., AUTOMOTIVE LIGHTING LIGHTING THE WAY TO A BRIGHT FUTURE, Accessed: 05/12/2022. (n.d.).

[143] S. Gestermann, W. Köppchen, V. Krause, M. Möthrath, D.W. Pophusen, A. Sandquist, O. Zöllner, Authors: Polycarbonat und seine Blends für Karosseriebauteile Polycarbonate and its Blends for Car Body Parts, 2005.

[144] M.E.J. Dekkers, S.Y. Hobbs, V.H. Watkins, Morphology and deformation behaviour of toughened blends of poly(butylene terephthalate), polycarbonate and poly(phenylene ether), 1991.

[145] S. Kobayashi, K. Müllen, Encyclopedia of Polymeric Nanomaterials, n.d.

[146] S.V.C. Jr., Polymer Science: A Textbook for Engineers and Technologists, Hanser Publications, Munich, 2019.

[147] John T. Bendler, ed., Handbook of Polycarbonate Science and Technology, 1st Edition, CRC Press, Boca Raton, 2000.

[148] Advances in Polycarbonates, n.d.

[149] A.K. Gupta, D.J. Lloyd, S.A. Court, Precipitation hardening in Al-Mg-Si alloys with and without excess Si, 2001. www.elsevier.com/locate/msea.

[150] G.A. Edwards, K. Stiller, G.L. Dunlop, M.J. Couper, THE PRECIPITATION SEQUENCE IN Al±Mg±Si ALLOYS, n.d.

[151] A calorimetric study of precipitation in commercial aluminium alloy 6061, 1991.

[152] Y.J. Liu, Z. Liu, Y. Jiang, G.W. Wang, Y. Yang, L.C. Zhang, Gradient in microstructure and mechanical property of selective laser melted AlSi10Mg, J Alloys Compd. 735 (2018) 1414–1421. https://doi.org/10.1016/j.jallcom.2017.11.020.

[153] R. Pal, A. Basak, Linking Powder Properties, Printing Parameters, Post-Processing Methods, and Fatigue Properties in Additive Manufacturing of AlSi10Mg, Alloys. 1 (2022) 149–179. https://doi.org/10.3390/alloys1020010.

[154] R. Pal, A. Basak, Linking Powder Properties, Printing Parameters, Post-Processing Methods, and Fatigue Properties in Additive Manufacturing of AlSi10Mg, Alloys. 1 (2022) 149–179. https://doi.org/10.3390/alloys1020010.

[155] T. Hirata, T. Kimura, T. Nakamoto, Effects of hot isostatic pressing and internal porosity on the performance of selective laser melted AlSi10Mg

alloys, Materials Science and Engineering A. 772 (2020). https://doi.org/10.1016/j.msea.2019.138713.

[156] J.G. Santos Macías, L. Zhao, D. Tingaud, B. Bacroix, G. Pyka, C. van der Rest, L. Ryelandt, A. Simar, Hot isostatic pressing of laser powder bed fusion AlSi10Mg: parameter identification and mechanical properties, J Mater Sci. 57 (2022) 9726–9740. https://doi.org/10.1007/s10853-022-07027-9.

[157] SABIC Americas, LEXAN RESIN 103 - Technical Data Sheet, 2023.

[158] J.M. Dealy, K.F. Wissbrun, Melt Rheology and Its Role in Plastics Processing, Springer Netherlands, 1990. https://doi.org/10.1007/978-94-009-2163-4.

[159] American Society for Testing and Materials, Standard Test Methods for Vickers Hardness and Knoop Hardness of Metallic Materials - E92, (2017).

[160] Advances in Metal Additive Manufacturing, n.d.

[161] L. Minkowitz, S. Arneitz, P.S. Effertz, S.T. Amancio-Filho, Laser-Powder Bed Fusion Process Optimisation of AlSi10Mg Using Extra Trees Regression, n.d. https://ssrn.com/abstract=4270248.

[162] American Society for Testing and Materials, Standard Test Method for Deflection Temperature of Plastics Under Flexural Load in the Edgewise Position - D648, (2018).

[163] American Society for Testing and Materials, Standard Test Method for Tensile Properties of Plastics - D638, (2022).

[164] American Society for Testing and Materials, Standard Test Method for Apparent Shear Strength of Single-Lap-Joint Adhesively Bonded Metal Specimens by Tension Loading (Metal-to-Metal) - D1002, (2019).

[165] Leclerc H, Neggers J, Mathieu F, IDDN.FR.001.520008.000.S.P.2015.000.31500, Correli 3.0, 2015.

[166] S.M. Goushegir, J.F. dos Santos, S.T. Amancio-Filho, Fatigue Performance of Metal–Composite Friction Spot Joints, Materials. 14 (2021) 4516. https://doi.org/10.3390/ma14164516.

[167] M. Dubé, P. Hubert, J.N.A.H. Gallet, D. Stavrov, H.E.N. Bersee, A. Yousefpour, Fatigue performance characterisation of resistance-welded

thermoplastic composites, Compos Sci Technol. 68 (2008) 1759–1765. https://doi.org/10.1016/j.compscitech.2008.02.012.

[168] P. LIN, J. PAN, T. PAN, Failure modes and fatigue life estimations of spot friction welds in lap-shear specimens of aluminum 6111-T4 sheets. Part 1: Welds made by a concave tool, Int J Fatigue. 30 (2008) 74–89. https://doi.org/10.1016/j.ijfatigue.2007.02.016.

[169] American Society for Testing and Materials, Standard Practice for Statistical Analysis of Linear or Linearized Stress-Life (S-N) and Strain-Life (ε-N) Fatigue Data - E739, (2010).

[170] F. Wang, H. Bu, J. Luo, P. Zhang, L. Wang, X. Zhan, Influence of different micro-pattern types on interface characteristic and mechanical property of CFRTP/aluminum alloy laser bonding joint, International Journal of Advanced Manufacturing Technology. 120 (2022) 3543–3557. https://doi.org/10.1007/s00170-022-08748-6.

[171] M.M. Quazi, M.A. Fazal, A.S.M.A. Haseeb, F. Yusof, H.H. Masjuki, A. Arslan, Laser-based Surface Modifications of Aluminum and its Alloys, Critical Reviews in Solid State and Materials Sciences. 41 (2016) 106–131. https://doi.org/10.1080/10408436.2015.1076716.

[172] R. Christensen, Analysis of Variance, Design, and Regression: Applied Statistical Methods, CRC Press reprint, New York, 1996.

[173] Rheology and Processing of Polymeric Materials Volume 2, n.d.

[174] Y. Tanaka, T. Sako, T. Hiraoka, M. Yamaguchi, M. Yamaguchi, Effect of morphology on shear viscosity for binary blends of polycarbonate and polystyrene, J Appl Polym Sci. 137 (2020). https://doi.org/10.1002/app.49516.

[175] X. Li, F. Liu, N. Gong, C. Yang, B. Wang, Surface topography induced high injection joining strength of polymer-metal composite and fracture mechanism, Compos Struct. 184 (2018) 545–553. https://doi.org/10.1016/j.compstruct.2017.10.020.

[176] O. Izadi, P. Mosaddegh, M. Silani, M. Dinari, An experimental study on mechanical properties of a novel hybrid metal–polymer joining technology based on a reaction between isocyanate and hydroxyl groups, J Manuf

Process. 30 (2017) 217–225. https://doi.org/10.1016/j.jmapro.2017.09.022.

[177] S.T. Amancio-Filho, L.B. Canto, E. Hage, J. v Esteves, J.F. dos Santos, L.B. Canto, Friction spot joining of aluminum 6181-T4 and carbon fiber reinforced poly(phenylene sulfide) Friction Spot Joining of Aluminum-Composite Hybrid Structures View project Friction-based Injection Clinching Joining View project FRICTION SPOT JOINING OF ALUMINUM 6181-T4 AND CARBON FIBER REINFORCED POLY(PHENYLENE SULFIDE), 2012. https://www.researchgate.net/publication/286800000.

[178] O. Izadi, P. Mosaddegh, M. Silani, M. Dinari, An experimental study on mechanical properties of a novel hybrid metal–polymer joining technology based on a reaction between isocyanate and hydroxyl groups, J Manuf Process. 30 (2017) 217–225. https://doi.org/10.1016/j.jmapro.2017.09.022.

[179] O. Izadi, M. Silani, P. Mosaddegh, M. Farzin, Warpage and bending behavior of polymer–metal hybrids: experimental and numerical simulations, International Journal of Advanced Manufacturing Technology. 98 (2018) 873–885. https://doi.org/10.1007/s00170-018-2226-0.

[180] B. Huang, L. Sun, L. Li, L. Zhang, Y. Lin, J. Che, Experimental investigation of the strength of polymer-steel direct adhesion (PSDA) joints with micro-structures ablated by laser, J Mater Process Technol. 249 (2017) 407–414. https://doi.org/10.1016/j.jmatprotec.2017.06.031.

[181] B. Bonpain, M. Stommel, Influence of surface roughness on the shear strength of direct injection molded plastic-aluminum hybrid-parts, Int J Adhes Adhes. 82 (2018) 290–298. https://doi.org/10.1016/j.ijadhadh.2018.02.003.

[182] X. Li, B. Wang, D. Xu, B. Wang, W. Dong, M. Li, Super-high bonding strength of polyphenylene sulfide-aluminum alloy composite structure achieved by facile molding methods, Compos B Eng. 224 (2021). https://doi.org/10.1016/j.compositesb.2021.109204.

[183] S. Wang, F. Kimura, S. Zhao, E. Yamaguchi, Y. Ito, Y. Kajihara, Influence of fluidity improver on metal-polymer direct joining via injection molding,

Precis Eng. 72 (2021) 620–626. https://doi.org/10.1016/j.precisioneng.2021.07.001.

[184] T. Kleffel, D. Drummer, Investigating the suitability of roughness parameters to assess the bond strength of polymer-metal hybrid structures with mechanical adhesion, Compos B Eng. 117 (2017) 20–25. https://doi.org/10.1016/j.compositesb.2017.02.042.

[185] M. Du, W. Dong, X. Li, L. Wang, B. Wang, B. Tang, Effect of surface topography on injection joining Ti alloy for improved bonding strength of metal-polymer, Surf Coat Technol. 433 (2022). https://doi.org/10.1016/j.surfcoat.2022.128132.

[186] S. Wurzbacher, S. Gach, U. Reisgen, C. Hopmann, Joining of plastic-metal hybrid components by overmoulding of specially designed form-closure elements, Materwiss Werksttech. 52 (2021) 367–378. https://doi.org/10.1002/mawe.202000158.

[187] A.J. Comer, K.B. Katnam, W.F. Stanley, T.M. Young, Characterising the behaviour of composite single lap bonded joints using digital image correlation, Int J Adhes Adhes. 40 (2013) 215–223. https://doi.org/10.1016/j.ijadhadh.2012.08.010.

[188] G. Sun, X. Liu, G. Zheng, Z. Gong, Q. Li, On fracture characteristics of adhesive joints with dissimilar materials – An experimental study using digital image correlation (DIC) technique, Compos Struct. 201 (2018) 1056–1075. https://doi.org/10.1016/j.compstruct.2018.06.018.

[189] N.Z. Borba, J.F. dos Santos, S.T. Amancio-Filho, The influence of clamping pressure on joint formation and mechanical performance of Ti6Al4V/CF-PEEK friction-riveted joints, Materials. 12 (2019). https://doi.org/10.3390/ma12050745.

[190] M.T. Takemori, Fatigue Fracture of Polycarbonate, Polym Eng Sci. 22 (1982) 937–945.

[191] D.H. Banasiak, A.F. Grandt, L.T. Montulli, Fatigue Crack Retardation in Polycarbonate, J Appl Polym Sci. 21 (1977) 1297–1309.

[192] L.E. Hornberger, K.L. Devries, The Effects of Residual Stress on the Mechanical Properties of Glassy Polymers, n.d.

[193] Q.Z. Fang, T.J. Wang, H.M. Li, Overload-induced retardation of fatigue crack growth in polycarbonate, Int J Fatigue. 30 (2008) 1419–1429. https://doi.org/10.1016/j.ijfatigue.2007.10.005.

[194] J.M. Sousa, J.R. Correia, J. Gonilha, S. Cabral-Fonseca, J.P. Firmo, T. Keller, Durability of adhesively bonded joints between pultruded GFRP adherends under hygrothermal and natural ageing, Compos B Eng. 158 (2019) 475–488. https://doi.org/10.1016/j.compositesb.2018.09.060.

[195] X. Jiang, X. Qiang, M.H. Kolstein, F.S.K. Bijlaard, Experimental investigation on mechanical behaviour of FRP-to-steel adhesively-bonded joint under combined loading - Part 2: After hygrothermal ageing, Compos Struct. 125 (2015) 687–697. https://doi.org/10.1016/j.compstruct.2014.12.040.

[196] F. Stazi, M. Giampaoli, M. Rossi, P. Munafò, Environmental ageing on GFRP pultruded joints: Comparison between different adhesives, Compos Struct. 133 (2015) 404–414. https://doi.org/10.1016/j.compstruct.2015.07.067.

[197] R. Wimberger-Friedl, Molecular orientation induced by cooling stresses. Birefringence in polycarbonate: III. Constrained quench and injection molding, J Polym Sci B Polym Phys. 32 (1994) 595–605. https://doi.org/10.1002/polb.1994.090320401.

[198] U.A. Dar, Y.J. Xu, S.M. Zakir, M.-U. Saeed, The effect of injection molding process parameters on mechanical and fracture behavior of polycarbonate polymer, J Appl Polym Sci. 134 (2017). https://doi.org/10.1002/app.44474.

[199] H.T. Pham, C.P. Bosnyak, K. Sehanobish, Residual stresses in injection molded polycarbonate rectangular bars, Polym Eng Sci. 33 (1993) 1634–1643. https://doi.org/10.1002/pen.760332408.

[200] M. Haghighi-Yazdi, J.K.Y. Tang, P. Lee-Sullivan, Moisture uptake of a polycarbonate blend exposed to hygrothermal aging, Polym Degrad Stab. 96 (2011) 1858–1865. https://doi.org/10.1016/j.polymdegradstab.2011.07.007.

[201] L. Dowling, J. Kennedy, D. Trimble, Effect of a modified energy density equation to achieve a more uniform energy input during LPBF for improved

repeatability, J Manuf Process. 77 (2022) 607–615. https://doi.org/10.1016/j.jmapro.2022.03.045.

[202] H. Shipley, D. McDonnell, M. Culleton, R. Coull, R. Lupoi, G. O'Donnell, D. Trimble, Optimisation of process parameters to address fundamental challenges during selective laser melting of Ti-6Al-4V: A review, Int J Mach Tools Manuf. 128 (2018) 1–20. https://doi.org/10.1016/j.ijmachtools.2018.01.003.

[203] W.A. Ayoola, W.J. Suder, S.W. Williams, Parameters controlling weld bead profile in conduction laser welding, J Mater Process Technol. 249 (2017) 522–530. https://doi.org/10.1016/j.jmatprotec.2017.06.026.

[204] T. Yang, T. Liu, W. Liao, H. Wei, C. Zhang, X. Chen, K. Zhang, Effect of processing parameters on overhanging surface roughness during laser powder bed fusion of AlSi10Mg, J Manuf Process. 61 (2021) 440–453. https://doi.org/10.1016/j.jmapro.2020.11.030.

[205] F. Kimura, S. Kadoya, Y. Kajihara, Active Air Venting of Mold Cavity to Improve Performance of Injection Molded Direct Joining, Nanomanufacturing and Metrology. 4 (2021) 109–117. https://doi.org/10.1007/s41871-021-00097-4.

[206] E.S. Sherman, A. Ram, S. Kenig, Tensile failure of weathered polycarbonate, Polym Eng Sci. 22 (1982) 457–465. https://doi.org/10.1002/pen.760220802.

[207] M.E.J. Dekkers, D. Heikens, The tensile behavior of polycarbonate and polycarbonate–glass bead composites, J Appl Polym Sci. 30 (1985) 2389–2400. https://doi.org/10.1002/app.1985.070300610.

[208] Handbook Committee, ASM handbook - Fatigue and Fracture, ASM International®, United States of America, 1996.

[209] J. Trapp, A.M. Rubenchik, G. Guss, M.J. Matthews, In situ absorptivity measurements of metallic powders during laser powder-bed fusion additive manufacturing, Appl Mater Today. 9 (2017) 341–349. https://doi.org/10.1016/j.apmt.2017.08.006.

[210] M. Heinle, D. Drummer, Measuring mechanical stresses on inserts during injection molding, Advances in Mechanical Engineering. 7 (2015) 1–6. https://doi.org/10.1177/1687814015584479.

APPENDIX A

Using a Pareto chart (Figure A.1) with a significance level (α) of 0.05, it was shown that all five studied L-PBF parameters (laser power, scan speed, laser spot diameter, layer height and hatching distance) play a significant influence on the relative density of the AlSi10Mg printed parts, with layer height and laser power showing the highest influence on the relative density. Moreover, the Pareto Chart indicates that only two-way interaction influencing the relative density is the laser scan speed-laser spot diameter; however, only at a small level. Other interactions do not show a significant level of influence on the density.

As shown in the main effect plots of Figure A.2, the laser power positively affected the relative density since aluminum alloys require high energy to melt due to their low electromagnetic absorption and high reflectivity [209]. In contrast, relative density exhibited a negative dependency on scanning speed, laser spot diameter, and layer height since the energy delivered by the laser is inversely proportional to these factors [124]. The hatching distance showed a positive effect on the relative density of the AlSi10Mg inserts, as shown in reference [161].

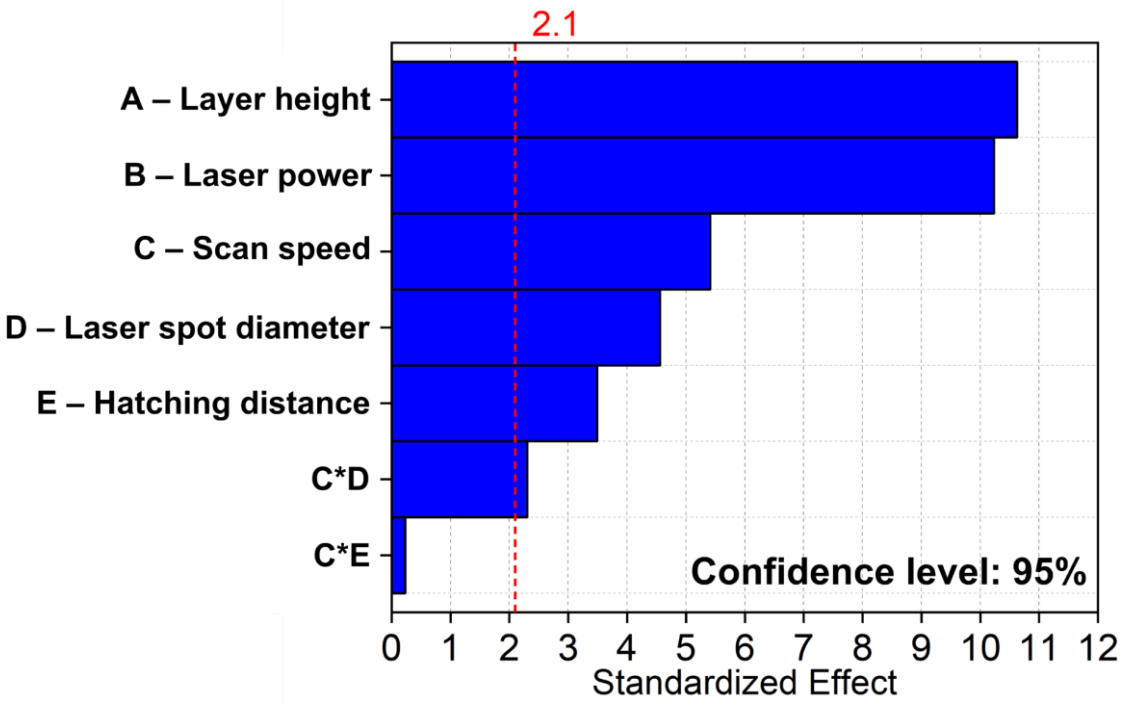

Figure A.1: Pareto chart of standardized effects for relative density of AlSi10Mg printed parts via L-PBF.

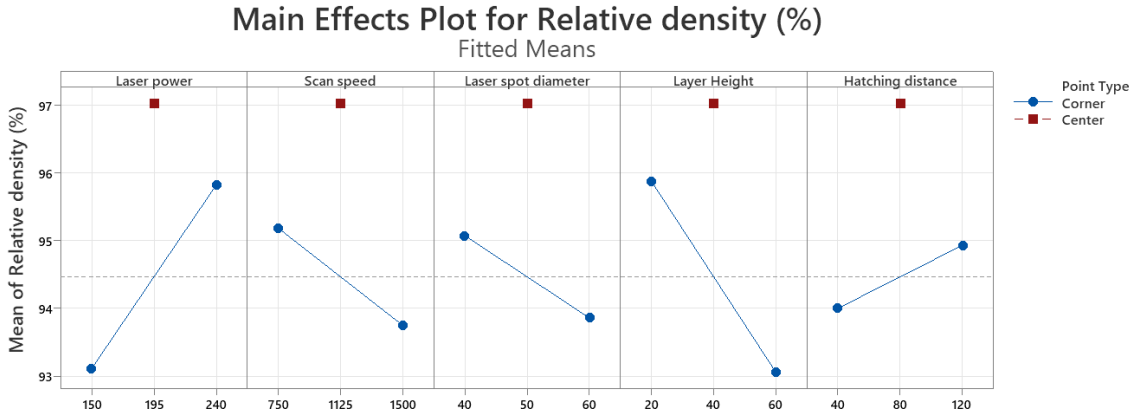

Figure A.2: Main effect plots illustrating the influence of the laser powder bed fusion (L-PBF) parameters (laser power, scan speed, spot diameter, layer height and hatching distance) on the relative density of AlSi10Mg printed parts.

Table A.1: Analysis of variance (ANOVA) of the ultimate lap-shear force of PC/AA6061 hybrid joints.

Source	DF	Adj SS	Adj MS	F-Value	p-Value
Model	8	138.194	172.743	40.73	0.001
Linear	5	118.318	236.637	55.80	0.001
Laser power	1	44.282	442.817	104.42	0.001
Laser scan speed	1	12.327	123.267	29.07	0.001
Laser spot diameter	1	8.882	88.817	20.94	0.001
Layer Height	1	47.602	476.017	112.25	0.001
Hatching distance	1	5.227	52.267	12.32	0.002
2-Way Interactions	2	2.308	11.542	2.72	0.093
Scan speed*Laser spot diameter	1	2.282	22.817	5.38	0.032
Scan speed*Hatching distance	1	0.027	0.0267	0.06	0.805
Error	18	7.633	0.4241		
Total	26	145.827			

APPENDIX B

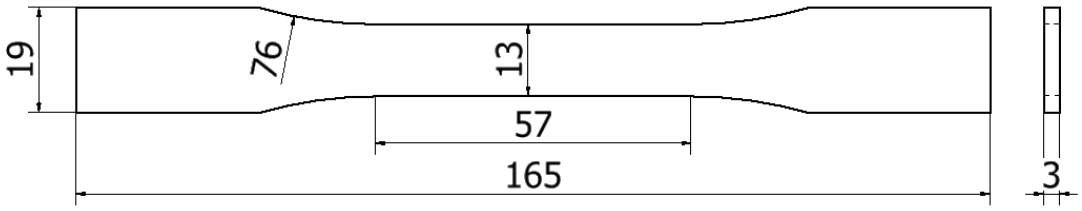

Figure B.1: PC tensile specimens with dimensions according to ASTM D638 - Type I.

APPENDIX C

Table C.1 provides the image acquisition system technical specifications and setup. Moreover, the details of the DIC analysis parameters and software are detailed in Table C.2.

Table C.1: Details of the used cameras and image acquisition settings.

Camera	Canon EOS 5DS*
Definition	8736x5856
Color filter	Bayer
Gray level amplitude	14 bits
Lens	Macro 180 mm
Aperture	F8
Image scale	11.4 µm/px (FC) and 3.7 µm/px (LC)*
Image acquisition rate	4 s
Exposure time	1/10
Patterning technique	Sprained paint

- A Canon EF 2x lens extender was used to better image acquisition.

Table C.2: Digital Image Correlation (DIC) software and analysis parameters.

DIC software	Correli 3.0 framework
Image filtering	None
Shape functions	Linear (T3)
Element length	Variable
Matching criterion	Regularized sum of squared functions
Strain calculation	Strain derivative of shape functions

APPENDIX D

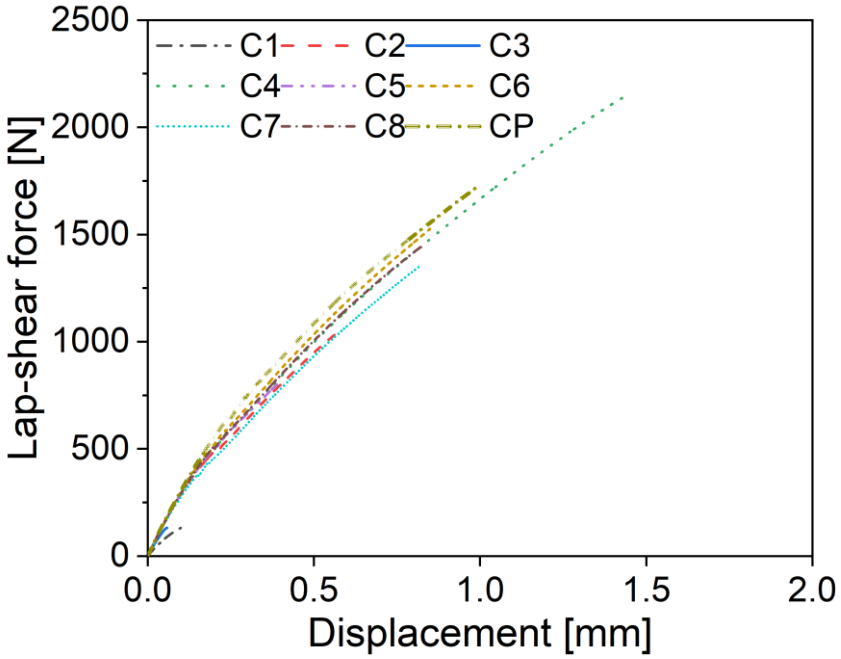

Figure D.1: Typical force-per-displacement curve for PC/AA6061 joints with a metal insert laser textured with 4 scans and injected overmolded using design of experiments parameters depicted in Table 3.5.

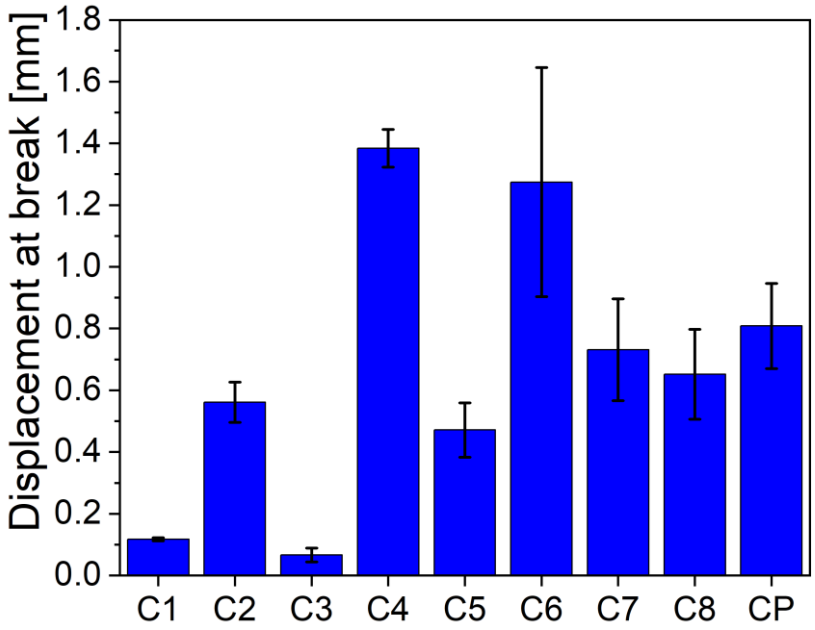

Figure D.2: Displacement at the break of injection molded PC/AA6061 joints injection overmolded in different conditions (see Table 3.5).

APPENDIX E

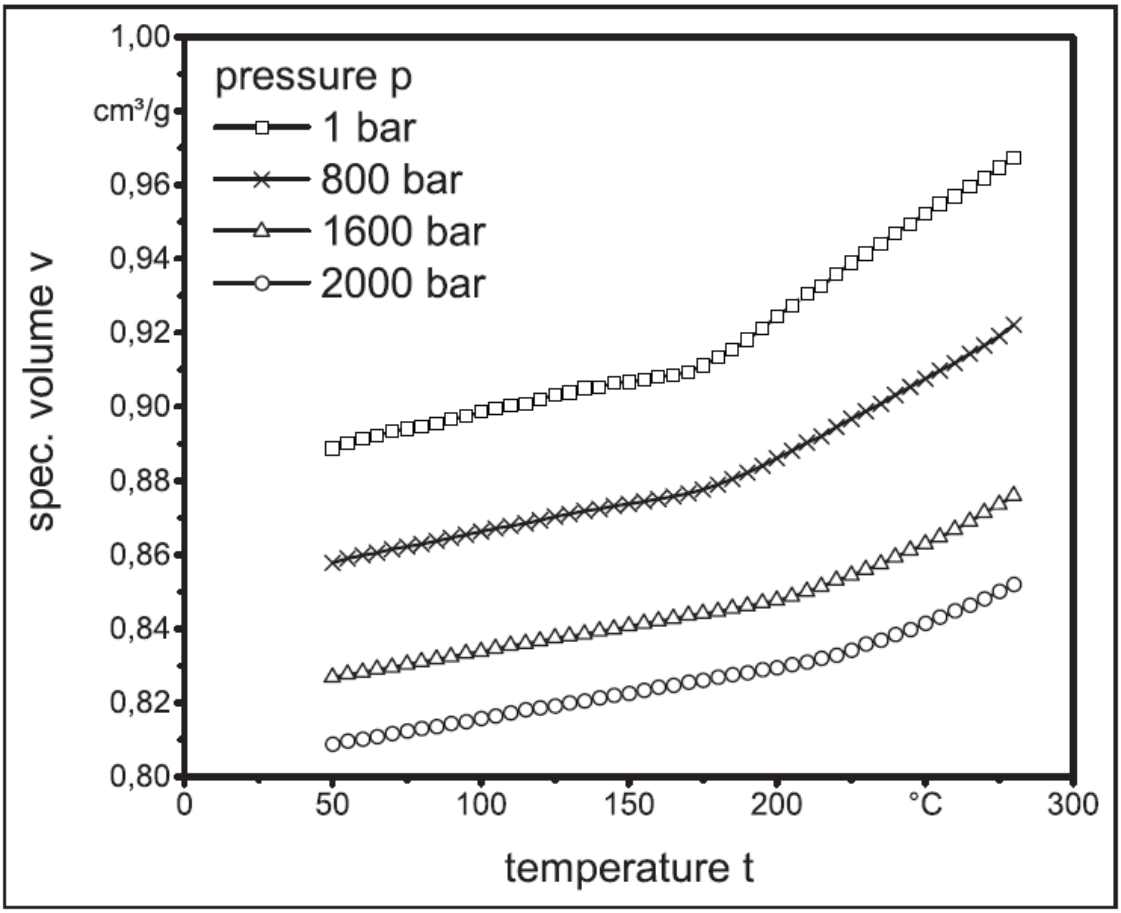

Figure E.1: pvT diagram of polycarbonate (PC). Extracted from reference [210].

APPENDIX F

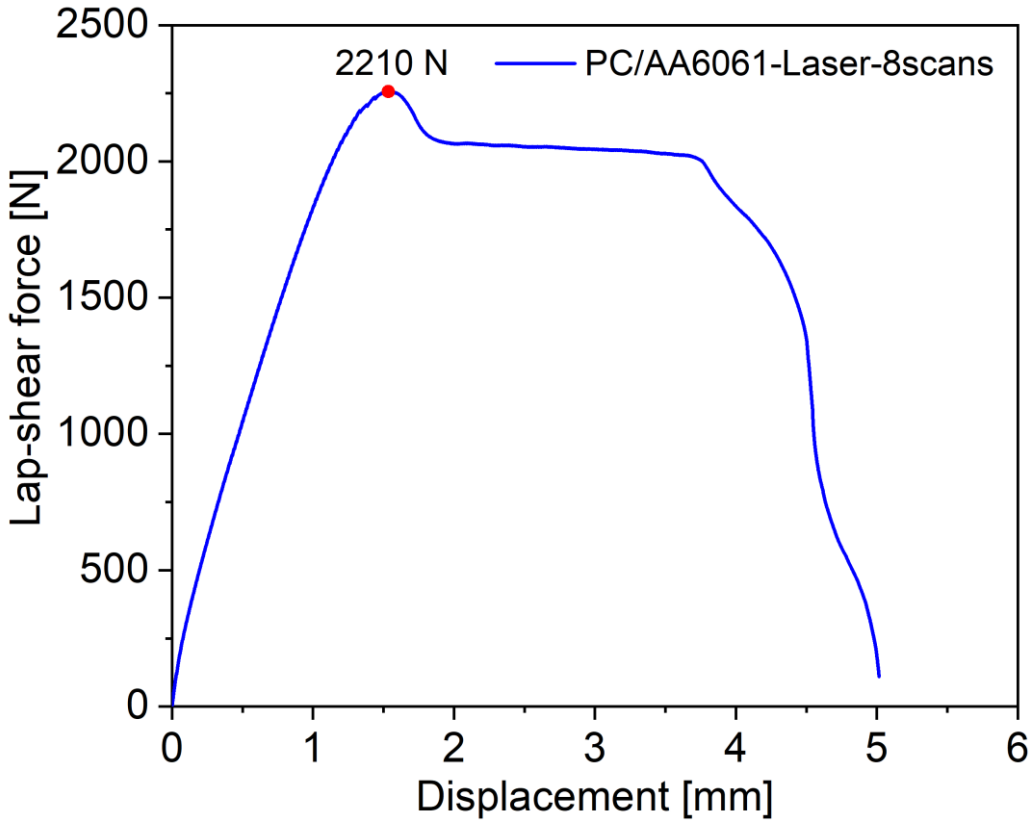

Figure F.1: Typical force-per-displacement curve for a PC/AA6061 joint with a metal insert laser textured with 8 scans (grooves with depth of 65 µm) injection overmolded at the optimized condition.

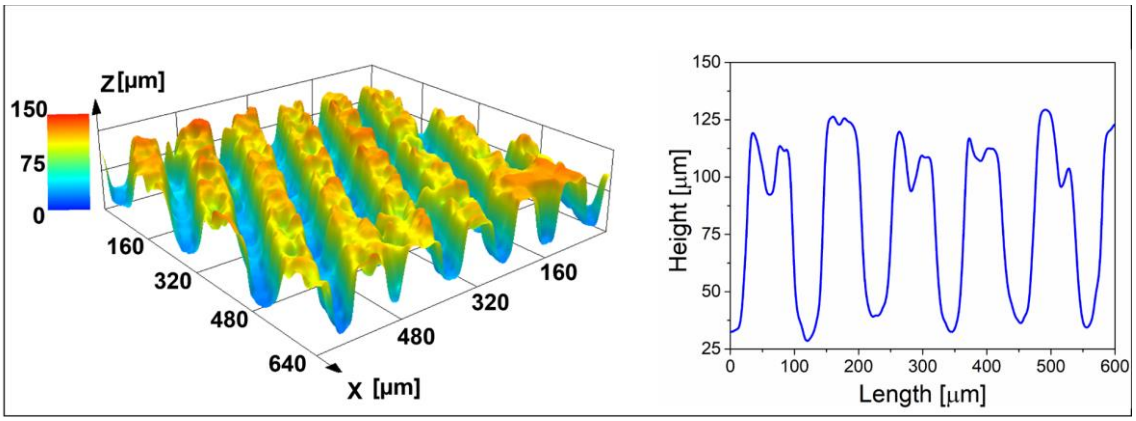

Figure F.2: Laser scanning confocal image and height profile of the laser textured AA6061 surface. On the left-hand side a 3D surface image and on the right-hand side the surface profile. Laser texturing parameters: frequency 20 kHz, scan speed 500 mm/s and 8 scans.

APPENDIX G

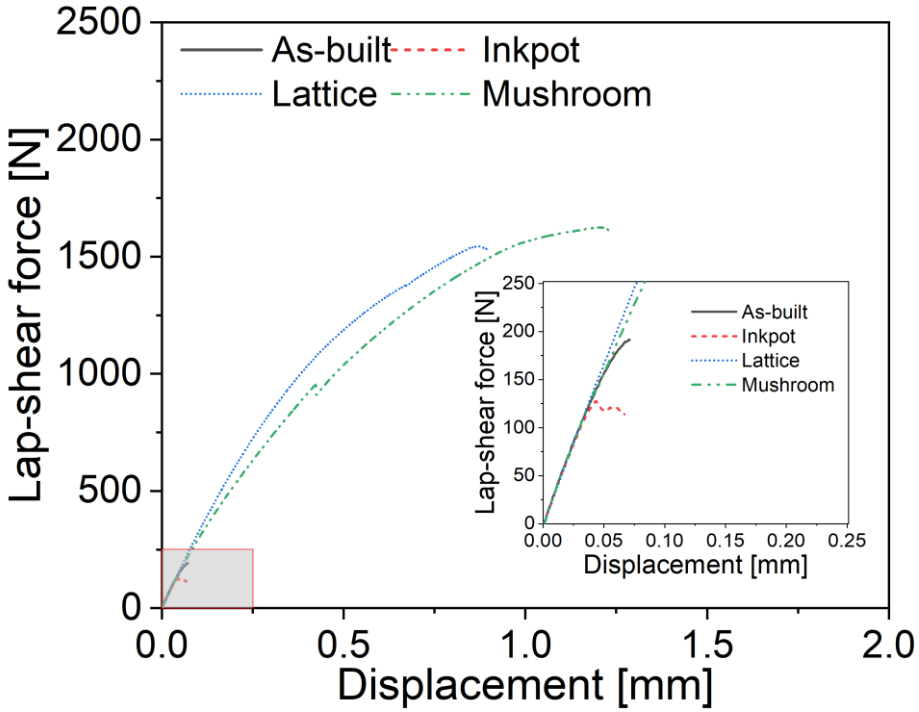

Figure G.1: Typical force-per-displacement curve for PC/AlSi10Mg joints with a metal insert produced with laser powder bed fusion (L-PBF) with different surface structures (Inkpot, Lattice and Mushroom; see Figure 3.7).

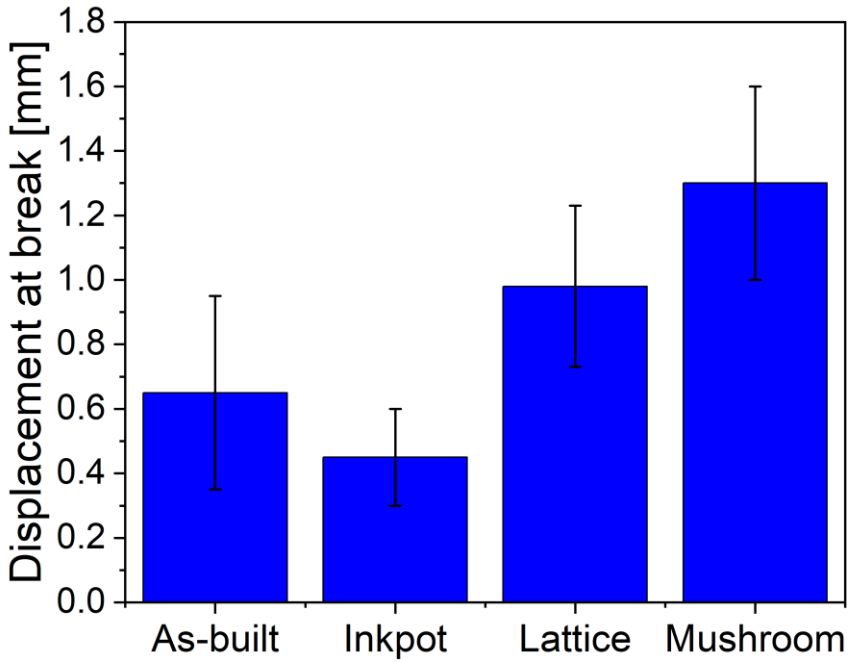

Figure G.2: Displacement at the break of injection overmolded PC/AlSi10Mg joints injection overmolded in the optimized condition C4 (see Table 3.5).